

TALLINN UNIVERSITY OF TECHNOLOGY
DOCTORAL THESIS
45/2020

**Additive Manufacturing of Novel
Ceramic-Based Composite Scaffolds
for Bone Tissue Engineering**

NIKHIL KUMAR KAMBOJ



TALLINN UNIVERSITY OF TECHNOLOGY

School of Engineering

Department of Mechanical and Industrial Engineering

This dissertation was accepted for the defence of the degree 12/10/2020

Supervisor:

Professor Irina Hussainova
School of Engineering
Department of Mechanical and Industrial Engineering
Tallinn University of Technology
Tallinn, Estonia

Opponents:

Professor Michael Gasik
Aalto University Foundation
Helsinki, Finland

Professor Enrico Bernardo
Department of Industrial Engineering
University of Padova
Padova, Italy

Defence of the thesis: 04/12/2020, Tallinn

Declaration:

Hereby I declare that this doctoral thesis represents my original investigation and achievements and is submitted for doctoral degree at Tallinn University of Technology. It has not been submitted elsewhere for a doctoral or equivalent academic degree.

Nikhil Kumar Kamboj

signature



European Union
European Regional
Development Fund



Investing
in your future

This work has been partially supported by ASTRA “TUT Institutional Development Programme for 2016-2022”, Graduate School of Functional Materials and Technologies (2014-2020.4.01.16-0032).

Copyright: Nikhil Kumar Kamboj, 2020

ISSN 2585-6898 (publication)

ISBN 978-9949-83-611-6 (publication)

ISSN 2585-6901 (PDF)

ISBN 978-9949-83-612-3 (PDF)

Printed by Koopia Niini & Rauam

TALLINNA TEHNIKAÜLIKOOL
DOKTORITÖÖ
45/2020

**Uudsete keraamilal põhinevate
komposiitkarkasside
kihtlisandustehnoloogia luukoetehnikas**

NIKHIL KUMAR KAMBOJ



Contents

List of publications.....	7
Author’s contribution to the publications.....	8
Introduction.....	9
List of abbreviations	11
1. Overview of the literature	12
1.1 Bone scaffolds	12
1.1.1 Synthetic scaffolds for bone tissue engineering (BTE).....	13
1.2 Additive manufacturing of ceramic-based scaffolds for BTE	14
1.2.1 Stereolithography	15
1.2.2 Binder jetting or 3D printing.....	16
1.2.3 Material extrusion	16
1.2.4 Powder bed fusion process	17
1.3 Requirements for ceramic scaffolds for BTE	19
1.3.1 Geometry and pore size	19
1.3.2 Mechanical compliance	20
1.3.3 Bioactivity, biocompatibility, and biodegradability.....	21
1.4 Crystalline and porous silicon for BTE.....	22
1.5 Objectives.....	23
2. Experimental.....	25
2.1 Powder feedstock.....	25
2.2 Scaffold design	26
2.3 Fabrication of scaffolds by SLM.....	26
2.4 Characterisation of the scaffolds.....	27
3. Results and discussion	30
3.1 Macro-porous silicon by SLM	30
3.2 Silicon-wollastonite scaffolds for drug delivery	31
3.2.1 Processing and characterisation	31
3.2.2 Vancomycin drug delivery	34
3.3 Cytocompatibility of silicon-wollastonite scaffolds and gene induction studies.....	35

3.3.1 Processing and characterisation	35
3.3.2 Assessment of scaffolds for osteo-lineages and cytocompatibility	38
3.4 Silicon-62 W glass scaffolds	39
3.4.1 Processing and characterisation	39
3.4.2 Bioactivity of silicon-62 W glass scaffolds	42
Conclusions	43
References	45
Acknowledgements	53
Abstract	54
Lühikokkuvõte	56
Appendix	57
Paper I	57
Paper II	71
Paper III	79
Paper IV	93
Curriculum vitae	104
Elulookirjeldus	106

List of publications

The following is a list of publications by the author, on the basis of which, this thesis has been prepared:

- I **Nikhil Kamboj**, Aghayan, M., Rodrigo-Vazquez, C.S., Rodríguez, M.A., and Hussainova, I., 2019. Novel silicon-wollastonite based scaffolds for bone tissue engineering produced by selective laser melting. *Ceramics International*, 45(18), 24691–24701, doi.org/10.1016/j.ceramint.2019.08.208.
- II **Nikhil Kamboj**, Rodríguez, M.A., Rahmani, R., Prashanth, K.G., and Hussainova, I., 2019. Bioceramic scaffolds by additive manufacturing for controlled delivery of the antibiotic vancomycin. *Proceedings of the Estonian Academy of Sciences*, 68(1), 185–190, doi.org/10.3176/proc.2019.2.10.
- III **Nikhil Kamboj**, Kazantseva, J., Rahmani, R., Rodríguez, M.A., and Hussainova, I., 2020. Selective laser sintered bio-inspired silicon-wollastonite scaffolds for bone tissue engineering. *Materials Science and Engineering: C*, p.111223, doi.org/10.1016/j.msec.2020.111223.
- IV Rodrigo-Vázquez, C.S., **Nikhil Kamboj**, Aghayan, M., Sáez, A., Antonio, H., Rodríguez, M.A. and Hussainova, I., 2020. Manufacturing of silicon-Bioactive glass scaffolds by selective laser melting for bone tissue engineering. *Ceramics International*, doi.org/10.1016/j.ceramint.2020.07.171.

Manuscripts are included in the Appendix.

Author's contribution to the publications

The contributions of the author to the papers included in this thesis are as follows:

- I The author conducted a major portion of the experimental work on the optimisation of the printing parameters of the scaffolds and subsequent biological analyses; methodology; data curation; and preparation of the initial draft of the manuscript. The results were presented at the 2nd Global Forum on Advanced Materials and Technologies for Sustainable Development (GFMAT-2), and the 4th International Conference on Innovations in Biomaterials, Biomanufacturing and Biotechnologies (Bio-4), July 21-26, 2019, Toronto, Canada.
- II The author conducted a major portion of the experimental work; formal analysis; methodology; interpretation of the results; and preparation of the initial draft of the manuscript. The results were presented at the 43rd International Conference and Exposition on Advanced Ceramics and Composites (ICACC-2019), Jan-Feb 1, 2019, Florida, USA.
- III The author conducted a major portion of the experimental work; optimisation of the printing parameters of the scaffolds; formal analysis; data curation; methodology; in-vitro experiments; creation of the initial draft with the help of co-authors; and answering the reviewers' questions. The results were presented at the 44th International Conference and Exposition on Advanced Ceramics and Composites (ICACC-2020), Jan 26-31, 2020, Florida, USA.
- IV The author conducted a portion of the experimental work; optimisation of the printing parameters of the scaffolds; mechanical characterisation; and writing of some sections of the initial draft.

Introduction

The next-generation manufacturing technologies for biomaterials present exciting opportunities for doctors, engineers, and professionals to design implants with specific designs and functionalities using novel materials and geometries, aimed at mitigating orthopaedic ailments, such as donor site morbidity, non-unions, bone tumour, and clinical constraints (El-Rashidy et al., 2017). Bone tissue engineering (BTE) has evolved into a multifaceted field, combining holistic approaches from biology, advanced manufacturing, and therapeutic medicine (Qu, 2020). Lately, the fabrication of customised scaffolds by additive manufacturing (AM) for bone fractures is emerging as a key research hotspot in the field of BTE.

The concept of “scaffold” in BTE encompasses several aspects, such as like osteoinduction, osteoconduction, mechanical stability, and vascularisation (Koc et al., 2019). The AM technologies has paved the way for personalised orthopaedic regenerative medicine (X. Wang et al., 2016). The timeline of some of the successfully fabricated 3D-printed customised bone implants includes the world’s first additively manufactured lower jaw mandible implant by Dr. Jules Poukens and his research team in Belgium in 2011 (Jules Poukens, 2011); the customised implant for a substantial cranial defect, designed and fabricated by researchers in Brazil through AM in 2014 (Jardini et al., 2014); and the world’s first 3D-printed titanium heel, triumphantly implanted by orthopaedic surgeons in Australia in 2014 (CSIRO, 2014).

However, the choice of materials (metals, polymers, ceramics, or composites) for scaffolds is regarded as the primary and exclusive factor in determining the prospects of the scaffold at the site of implantation. The scaffold is ideally expected to bio-mimic the natural features (both organic and inorganic) of the bone. The metallic scaffolds are subjected to several constraints, such as curbed degradation and stress shielding phenomenon, which can have several ramifications on the growth of osseous tissue at the site of implantation (Koons et al., 2020). Some of the polymeric scaffolds, implanted at the defect sites, commonly experience foreign body and immunological reactions owing to the lixiviation of the micro-particles, and possibly languish immunomodulation effects (Koons et al., 2020; Lichte et al., 2011). Bioceramics, such as calcium phosphate-based biomaterials are frequently used in BTE. The most frequently and popularly used are the Hydroxyapatite (HAP) scaffolds featuring calcium phosphate; it effectively replicates the bio-inorganics of the bone, as two-thirds of the dry weight of the bone typically comprises inorganic matter, of which HAP constitutes 85%. However, the slackened decaying rate of the stoichiometric HAP with restricted use in in-vivo applications (Kato et al., 2014) has resulted in a shifting of the spotlight to silicate-based bioceramics, including bioactive glasses. The silicate-based bioceramics can be ameliorative substitutes for calcium phosphate-based ceramics by benefitting from silicon. Pure macro-porous silicon scaffolds, synthesised by conventional anodisation methods were used in the past for repairing cortical defects in-vivo by facilitating COL-1 synthesis and alleviating osteoblastic differentiation (Sun, 2007). Si^{4+} ion is also regraded as an osteostimulatory ion, as it can stimulate bone marrow stromal cells (BMC) differentiation towards osteolineages without any external stimuli or ingredients (S.-C. Huang et al., 2015). The ion also possess the potential to boost the proliferation of the endothelial cells of the human umbilical vein by co-relating with the up-regulation of the vascular endothelial growth factor (VEGF) (Wang et al., 2013).

In this work, novel silicon-wollastonite and silicon-62 wollastonite glass-based ceramic composite scaffolds were fabricated by selective laser melting (SLM). For the first time, the bioactive macro-porous silicon scaffolds were produced using a laser-assisted technique, and a well-defined biomimetic design. Novel bioactive 62 wollastonite glass ceramic powder was developed using the ternary phase diagram of CaSiO_3 - $\text{MgCa}(\text{SiO}_3)_2$ - $\text{Ca}_3(\text{PO}_4)_2$ system. The fabricated composite scaffolds were obtained in single step, without the addition of a binder or geometric constraints, unlike most of the other ceramic-based scaffolds, which are commonly confronted with these limitations. Promising results were obtained, as revealed by cytocompatibility and osteolineage studies; furthermore, the modulation of the biomimetic design showed differential regulation of the primary transcription factors. These metalloid-based scaffolds demonstrated an intermediate level of strength i.e., lesser than that of metal-based composite scaffolds, but greater than that of ceramic- or polymer-based composite scaffolds. However, the strength of this metalloid-based composite scaffold can be further altered by increasing or decreasing the ceramic content in the composite scaffold. The “as-fabricated” scaffolds also demonstrated the potential of sustained delivery of the biological moieties. For an ongoing study, these novel scaffolds have been implanted on Wistar albino adult rats with calvaria bone defects of 20 mm in diameter. The findings from the research embodied in this thesis clearly demonstrate the capability of the novel metalloid-ceramic composite scaffolds to medicate peculiar orthopaedic defects, by altering the biomimetic design through AM.

List of abbreviations

BTE	Bone tissue engineering
3D	Three-dimensional
ECM	Extra-cellular matrix
β -TCP	β -tri-calcium phosphate
α -TCP	α -tri-calcium phosphate
rh-BMP	recombinant human bone morphogenetic protein
rh-PDGF	recombinant platelet derived growth factor
PDSC	Periosteum-derived stem cells
BMC	Bone marrow stromal cells
MSC	Mesenchymal stem cells
ASC	Adipose-derived mesenchymal cells
HAP	Hydroxyapatite
ALP	Alkaline phosphatase
DBM	Demineralised bone matrix
VEGF	Vascular endothelial growth factor
SBF	Simulating body fluid
OCN	Osteocalcin
OCP	Osteopontin
BSP	Bone sialoprotein
CAD	Computer-aided design
UV	Ultraviolet
DLP	Digital light processing
PVA	Poly (vinyl alcohol)
FDM	Fused deposition modelling
PCL	Poly (ϵ -caprolactone)
PLA	Poly(lactic acid)
SLM	Selective laser melting
SLS	Selective laser sintering
FE	Finite element
DMEM	Dulbecco's modified eagle's medium
FBS	Foetal bovine serum
PBS	Phosphate buffer saline
FITC	Fluorescein isothiocyanate
GAPDH	Glyceraldehyde-3-phosphate dehydrogenase

1. Overview of the literature

This chapter provides insights into the principles of scaffolds for bone tissue engineering (BTE). Commonly used orthopaedic materials with their microstructure, mechanical properties, and methods of manufacturing; and various biomimetic approaches for bone tissue repair are discussed.

1.1 Bone scaffolds

Osseous tissue, commonly known as bone provides a framework to the body of a living being and plays a crucial role in its mechanical movement, shielding the organs, and hosting numerous blood cells (Liao et al., 2011). Bone tissue is constantly remodelled and can dynamically heal itself owing to the constant activity of the osteoblasts, osteocytes, and osteoclasts, as depicted in Fig. 1.1.

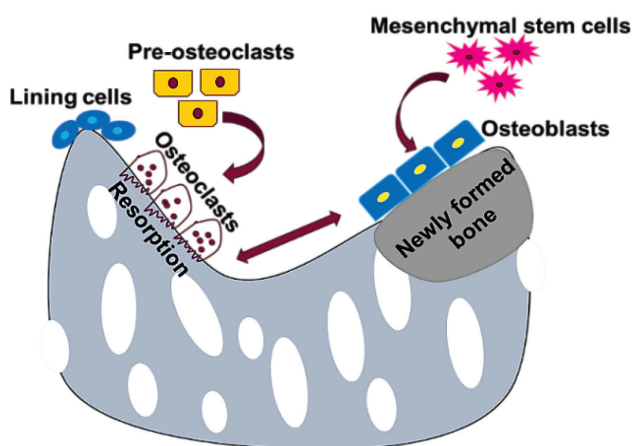


Figure 1.1 Bone regeneration process, depicting the constant remodelling of bone by osteoclasts and osteoblasts; adapted from (Maradze et al., 2018)

Usually, under normal circumstances bones can regenerate themselves and have the capacity to heal micro-level damages, without inducing a scar formation. On the other hand, complex or compromised bone fractures, which are generally larger than critical-sized defects, usually suffer from non-unions and non-healing of the bones (Ho-Shui-Ling et al., 2018). Additionally, co-morbidities, combined with sedentary lifestyles, genetic factors, and diabetes can delay the healing process and pose the risk of non-unions (D. Holmes, 2017).

There are various types of bone fractures, depending on the impact and the way bone is shattered (partial or complete), which in turn, can lead to various complications, such as osteogenesis imperfecta, osteopenia, and osteoporosis. The disjunction of the bone may lead to serious complications, such as avascular necrosis, hypovolaemic shock, pulmonary syndrome, Volkmann's contracture, osteomyelitis, and osteoarthritis. Eventually, if the bone is left untreated, the infected organ may have to be amputated.

The bones at numerous locations in a human body can be fractured. The most prominent or common fracture sites include the hip, wrist, femur shoulder, ankle, tibia, and maxillofacial and cranial fractures (Ho-Shui-Ling et al., 2018).

Natural bone scaffolds involving autologous bone grafts (osseous graft from one anatomical site, transferred to a different site in the same individual), allogenic bone

grafts (osseous graft transplanted within genetically different individuals of the same species), and xenografts (osseous graft within genetically different individuals of the different species) have been used to heal various fracture sites (Roberts et al., 2012). These natural bone scaffolds were commonly used, before the advent of AM, to facilitate osseointegration or bone regeneration to heal the fracture sites. They were considered as one of the prime precedent in treating osseous tissues with defects and for bone regeneration (Goldberg et al., 2005). However, natural bone scaffolds suffer from several disadvantages, such as donor site infection, increased blood loss, heterotrophic ossification, the elevation of histocompatibility complex antigens, immunogenicity, limited availability of transplanted material, vulnerability to the risk of viral contamination, deprived mechanical properties, and inefficiency to completely bio-resorb after the transplantation (Burchard, 1983; Dimitriou et al., 2011; Flynn, 2011; Goldberg et al., 2005; Roberts et al., 2012; Stevenson et al., 1992; W. Wang et al., 2017).

Therefore, considering the serious complications posed by natural bone scaffolds, coupled with the patient discomfort and the continuous necessity of bone grafts in an ageing population has led to the emergence of synthetic bone scaffolds as an alternative to osseous tissues.

1.1.1 Synthetic scaffolds for BTE

Critical-sized bone defects, commonly in the range of 1-4.5 cm are generally repaired by synthetic grafts known as scaffolds (Schemitsch, 2017). To overcome the shortcomings of natural bone scaffolds, a permanent, reliable, sustainable, and holistic solution is required to heal and repair critical-sized bone defects. Synthetic bone scaffolds play an imperative role in BTE and can mimic the natural bone ECM by facilitating and providing a 3D network for regenerating the bone for critical defects. The synthetic bone scaffolds can be classified into three broad categories. This classification primarily depends on the fracture sites, as illustrated in Fig. 1.2.

Of late, 3D printing has emerged as an efficient solution to the fabrication of scaffolds for BTE, as it allows custom-designed scaffolds suitable to the defect. Various fabrication techniques allow superior control of parameters, such as pore size, porosity, surface roughness, and mechanical properties of the scaffolds to better suit the anatomy of the patient's defective bone.

Synthetic bone grafts manufactured by AM technologies can also be integrated with active biomolecules. They can influence bone growth by acting on the antagonist of bone marker genes and enhancing its proliferation. Most synthetic grafts are natural bone matrix (ECM) or β TCP scaffolds infused with bioactive molecules. Some of these products include rh-BMP-2 [Infuse[®] bone graft] (Ho-Shui-Ling et al., 2018), rh-BMP-7 [Osigraft] (Ho-Shui-Ling et al., 2018), rh-PDGF [Augment[®] bone graft] (Krell et al., 2016), rhBMP-6 + whole blood coagulum [Osteogrow] (Genera Research Ltd, 2014), and allograft-derived growth factor [Osteoamp] (Ho-Shui-Ling et al., 2018). These bone grafts are mainly used for cervical and lumbar spine, wrist, ankle, and grim fractures of femur and tibia, where the fracture size is between 2 to 4 cm.

The last category of scaffolds relies on the delivery of cells encapsulated on cell-based scaffolds (Bolander et al., 2017). The commonly used stem cells are PDSCs, BMSCs, and ASCs. The "as-prepared" construct can be further nourished and developed in a bioreactor system to reach a more advanced stage (Ho-Shui-Ling et al., 2018), in which a 3D network is established that stimulates the entrapped stem cells to develop into new tissue or heal the defect site (Ingber et al., 2006). Stem cell therapies, combined with an allogenic graft matrix or HAP matrix usually heal critical size defects greater than 4 cm by

intermediate avascular cartilaginous callus (Schindeler et al., 2008). These bone grafts are primarily used for femoral neck fractures and to support fracture sites of defects more than 4 cm in size.




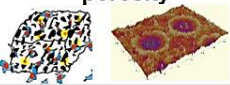
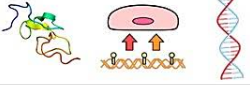




	Synthetic bone grafts	Synthetic bone grafts (ceramic carrier + bioactive molecules)	Synthetic bone grafts (ceramic carrier + stem cells)
Scaffolds	3D Scaffolds 	Collagen and bioceramic scaffolds 	Bioceramic granules and scaffolds 
Functionality	Surface roughness, pore size, and porosity 	Growth factors, genes, and small molecules 	Stem cells, MSCs, and PDSCs 
Fracture site length	Fracture sites < 2 cm 	Fracture sites 2 - 4 cm 	Fracture sites > 4 cm 

Figure 1.2 Three major categories of synthetic scaffolds used for bone repair

Three dimensional (3D) printed synthetic ceramic scaffolds with enhanced functionality, achieved by precisely controlling the pore size, porosity, and 3D shapes using AM allow flexibility in design through CAD; this is the motivation for the present study. The unification of bone tissue engineering and synthetic bone scaffolds using AM has become a synergistic approach, nowadays, for repairing bone defects. Furthermore, 3D customised synthetic bone ceramic scaffolds are a current trend, as they are biocompatible, osteoconductive, and can precisely fit into a defect in a patient's cranial, maxillofacial, femur, and tibia bones.

1.2 Additive manufacturing of ceramic-based scaffolds for BTE

The advent of AM has resulted in an advancement of customised scaffolds of BTE. The shortcomings faced by the conventional techniques, for example, inability to fabricate scaffolds with desired porosities, pore sizes, and controlled geometries, as well as a non-adaptability towards in-vivo microenvironment and subtractive methods, has resulted in the emergence of rapid manufacturing or AM techniques.

Presently, 3D printing techniques are commonly used for ceramic-based scaffolds. These techniques rely on CAD to have precise control over the microstructure of the scaffolds.

Table 1.1 Commonly used conventional techniques to fabricate bioactive ceramic composite scaffolds

Conventional technique	Disadvantages
Solvent casting	Inability to form complex shapes, as only flat sheets and tubes can be fabricated (Aboudzadeh et al., 2010; Subia et al., 2010).
Sol-gel	Usually, structures deteriorate faster, offering inferior mechanical properties (Q.-Z. Chen et al., 2010).
Electrospinning	Use of organic solvents, which can be toxic to the body.
Freeze drying	Time-consuming; strenuous energy utilisation; usage of noxious solvents; and production of random pores of 15 to 30 µm size (Matassi et al., 2011; Roseti et al., 2017).
Gas foaming	Excessive heat generation during the process of compressive moulding, which can alter the composition and ultimately lead to the formation of additional phases in synthetic matrices; close and non-interconnected porous structures with the formation of an additional nano-porous layer on the surface of the matrix (Roseti et al., 2017).

Henceforth, the restrictions and shortcomings posed by the conventional techniques has led to the rapid exploitation of the AM techniques for the fabrication of customised ceramic-based scaffolds. The rapid manufacturing techniques include the following: 1) stereolithography, 2) binder jetting, 3) material extrusion, and 4) powder-bed fusion process (SLM/S). Bioceramic scaffolds are more amenable to BTE than their metallic and polymer counterparts owing to their osteoconductivity and potential osteoinductivity. Some commonly used bioceramics for BTE include calcium silicates, calcium phosphates, bioactive glasses, and polymer-bioceramic composites. In the following sections, AM of calcium silicates, calcium phosphates, bioactive glasses, and polymer-bioceramic composites are discussed in detail.

1.2.1 Stereolithography

Stereolithography uses a photopolymer liquid, which is disclosed to a focused UV laser. The photopolymer is scanned by the laser, which eventually results in a phenomenon called photo-polymerisation (Van Bochove et al., 2016). The photo-polymerised material hardens to become a solid part, layer-by-layer. The ceramic phase incorporated in the ceramic stereolithography can impede or alter the ceramic printing which can be attributed to differential light scattering effects in the UV range (Gentry et al., 2013; Hwa et al., 2017). Differential light scattering phenomena can be due to scattering dominant behaviour of the particle sizes and concentration of the ceramic in the suspension and refractive index which can be annihilated by the Mie model (Equation 1).

$$\frac{\Delta n}{n_0} = \frac{n_{cer} - n_0}{n_0} \quad (1)$$

n_{cer} represents refractive index of the ceramic phase in the suspension whereas n_0 denotes refractive index of suspension (medium). Smaller the refractive index difference between the suspension or monomer and ceramic powder, higher the energy propagates in the forward with very negligible amount of energy scattered and vice versa.

However, ceramic stereolithography allows to fabricate polymer-ceramic composite leveraging onto the photo-polymerised resin and hence as a result requires the debinding of the polymer phase in the composite through pyrolysis. This can have several ramifications in the ultimate fate on the final finished product (ceramic phase) as it can deteriorate and pose several geometrical constraints with compromised mechanical properties on the final sample.

1.2.2 Binder jetting or 3D printing

Binder jetting offers several advantages in BTE, as assorted binders can solidify the powder to fabricate customised scaffolds (Hwa et al., 2017; Ziaee et al., 2019). The selection of the binder is vital for the binder jetting process, as it plays a pivotal role in the printability of the powder feedstock. The binder must endure the shear stress-strain induced during the printing process. Additionally, the binder should have a low viscosity, good powder interaction, long shelf life, and potential to burn-out during firing (J. Liu et al., 2003).

One of the predicaments associated with the binder jetting technique is the deposition of biological moieties on the bioceramic scaffold matrix (Nooeaid et al., 2014). The heat treatment during de-binding and sintering can lead to the production of unwanted by-products from the biological moieties, and thermally degrade them; these by-products can be toxic for the human body. The bioceramic scaffolds produced by binder jetting usually are impeded with several other constraints, such as deteriorated mechanical properties, geometric constraints, and formation of undesired phases.

1.2.3 Material extrusion

Material extrusion technique involves the extrusion of a single material or a mixture of materials, using a nozzle to form a 3D scaffold. Material extrusion can be divided into two broad categories, FDM and Robocasting.

The materials fabricated through FDM generally include polymers, such as PCL, PLA, and other biocompatible polymers (B. Holmes et al., 2016; Hutmacher et al., 2001; Steffens et al., 2016). For these materials, heat treatment at low temperatures is sufficient to melt the polymer. Because of a process limitation, the FDM method cannot print osteoconductive ceramics properly, as it can lead to unwanted phases and several geometric constraints in the polymeric matrix. Therefore, researchers have attempted to add lesser bioactive ceramic content to the polymer matrix to mitigate the issues with the FDM process for polymer scaffolds.

Robocasting, which is an extrusion-based method, mainly relies on the rheological properties of the bioactive ceramic slurries (HAP, TCP, calcium silicate, and bioglasses such as 45S5 Bioglass® are usually mixed with water and an anionic dispersant to prepare the slurries). The flowable slurry is then passed through an extrusion head for the scaffold fabrication (Eqtesadi et al., 2014). Water-based robocast scaffolds, incorporated with bioceramic components with superior mechanical properties were fabricated. These encompass HAP (Miranda et al., 2008), β -TCP (Miranda et al., 2006), wollastonite (A. Liu et al., 2016) and 45S5 Bioglass® (Eqtesadi et al., 2014). In summary, the material extrusion-based process has been predominately used in BTE depending on the type of composite used. Polymer-ceramic composites have been mostly fabricated by FDM; while, most pure bioceramic scaffolds have been fabricated through direct ink writing or robocasting.

1.2.4 Powder bed fusion process

SLS/M (i.e. SLS or SLM) is a powder bed fusion process, in which a laser source either fuses (in SLS) or melts (in SLM) the powder bed as depicted in Fig. 1.3(a-b). The fundamental difference between SLM and SLS is in the energy of the laser source. In SLS, the laser expedites the sintering process, while SLM facilitates the melting of the powder bed. The primary advantages associated with the powder bed fusion process include large build volume and relatively large production speed.

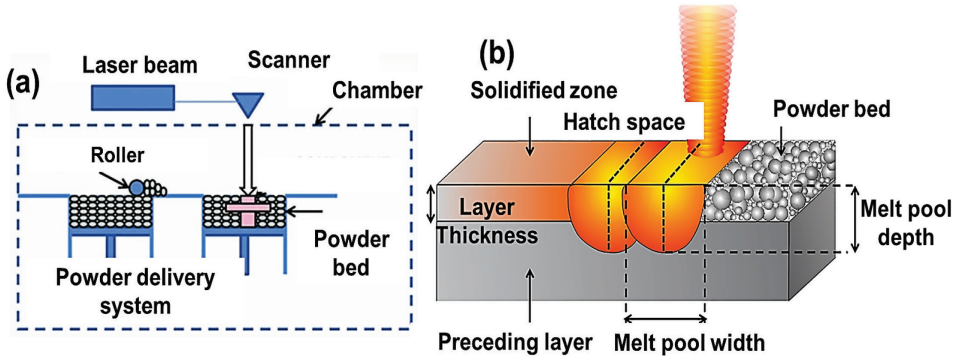


Figure 1.3 (a) General illustration of the SLS/M process; (b) schematic representation of the interaction between the laser beam and powder bed; adapted from (Frazier, 2014; Sola et al., 2019)

In the SLS process, the laser introduces just enough energy to the powder bed that is sufficient to exceed the point of phase transition (Mazzoli, 2013). A roller evenly distributes the powder over the platform so that successive layers can selectively sinter the powder. In the powder region, scanned by the laser a coalescence of the particles takes place, and this results in a significant reduction in the surface energy. This reduction in surface energy causes the sintering process (Mazzoli, 2013). The absence of the melting process here is responsible in retaining the voids or gaps (micro-spaces) between the adjacent particles (N Kamboj et al., 2019; Wubneh et al., 2018). These micro-spaces can play a key role in mimicking an ECM-like porous structure inside the scaffold (Mazzoli, 2013) and can be used for drug delivery systems (N Kamboj et al., 2019). This sintering process is repeated layer-by-layer to fabricate the final 3D structure.

SLM can be regarded as SLS performed at a higher temperature to completely melt the powder (Traini et al., 2008). The powder material feedstock undergoes a rapid solidification at a rate of 105-108 K/s (Calignano et al., 2014). The melt pool is highly dynamic, which can be attributed to the rapid scan speed or scanning by a Gaussian laser beam, which results in various defects, such as balling, splashing, and denudation of a single track (Simchi, 2006). SLM is also accompanied by several physical phenomena unfolding in the process, such as curing shrinkage, recoil pressure, diffusion, and heat conduction and radiation, as shown in Fig. 1.4.

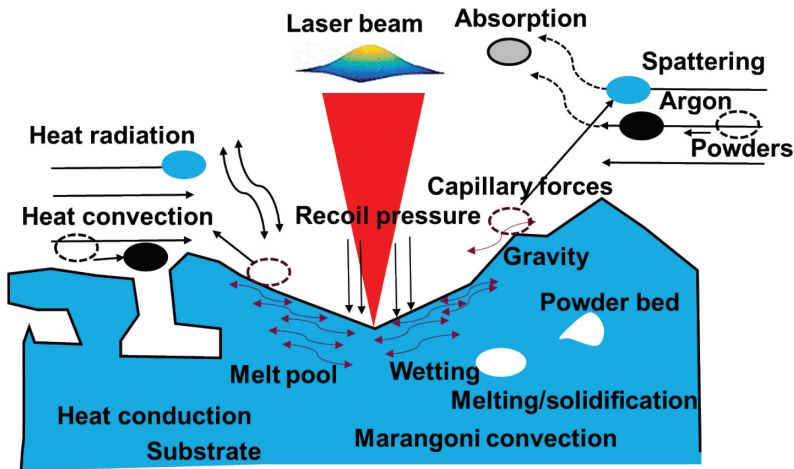


Figure 1.4 Physical phenomenon unfolding during the SLM process; adapted from (Chen et al., 2018)

SLM/S presents several advantages and is capable of producing porous scaffolds with 100 - 1000 μm pore sizes, which are generally required in BTE (Sears et al., 2016), as described in detail in Section 1.3. Figure 1.5 shows the superiority of the SLS/M techniques to the other techniques mentioned in Section 1.2, which can be attributed to a wider window of pore sizes possible with these two techniques through CAD modelling for BTE.

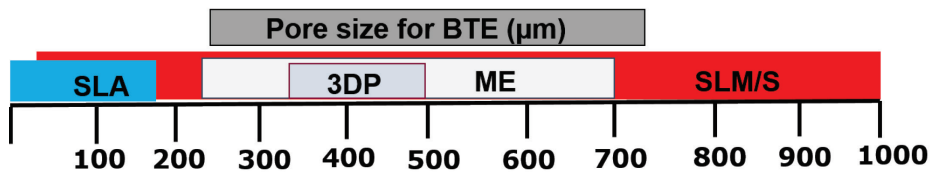


Figure 1.5 Superiority of SLM/S techniques over the other techniques; adapted from (Moreno Madrid et al., 2019)

The process parameters that usually define the magnitude of the laser energy or energy density applied depend on several parameters, such as laser spot size, laser power, scanning speed and layer thickness. In the present study, all these parameters were taken into consideration while fabricating porous ceramics composites for BTE.

The selection of laser power solely depends on the amount of energy absorbed by the powder bed. If the laser power is low, it can significantly influence the final product; it can lead to un-melted powder between successive layers and hence, ultimately cause the final product to fail. Henceforth, a decisive operating window is essential for the final product, which revolves around the laser power, scanning speed and laser spot size (Chen et al., 2018). In the present work, the working operational window was optimised for a novel ceramic-based feedstock powder, which was used to rapidly shape bioactive and osteoconductive biomimetic scaffolds.

1.3 Requirements for ceramic scaffolds for BTE

A brief overview of the scaffolds for BTE is presented in this section. An ideal scaffold should allow cell attachment onto the matrix, suitable mechanical properties, cell differentiation to osteoblasts, and vascularisation; furthermore, it should be commercially available (Amini et al., 2012).

1.3.1 Geometry and pore size

The geometry is considered as one of the most crucial parameters for the scaffolds. The design should be inspired by the biological aspects of the bone, eventually guide the cells to regenerate the bone tissue (Baino et al., 2015), enable the formation of the fibrous tissue, and act as a medium to support the stem cells (Shao et al., 2015). The geometry is also determined by the shapes of the pores and the pore size, which have a significant bearing on the mechanical strength, infiltration of the biological fluids, and formation of the blood capillaries to regenerate the bone tissue as shown in Figs. 1.6(a-c).

The optimum pore size and porosity for the scaffolds is a mandatory requirement in BTE. The porous scaffolds enhance the mechanical interlocking between the scaffold and the mangled or fractured bone mustering mechanical stability at the critical interface (Story et al., 1998). The pore sizes can be broadly classified into three categories, nano-pores (< 100 nm), micro-pores (100 nm-50 μm), and macro-pores (> 50 μm) (Vagaská et al., 2010). Micro-pores in the range of (10-50 μm) are essential for the diffusion of nutrients and oxygen for cell survivability. On the other hand, macro-pores ranging from 250-450 μm are optimal for bone growth and vascularisation through cell migration, as shown in Fig. 1.6(e) (Murphy et al., 2010). Because of the wide gap in the sized of micro- and macro-pores, numerous studies have been dedicated to the optimum pore sizes for both in vivo and in vitro microenvironments (Murphy et al., 2010; Shao et al., 2015; Story et al., 1998; Vagaská et al., 2010).

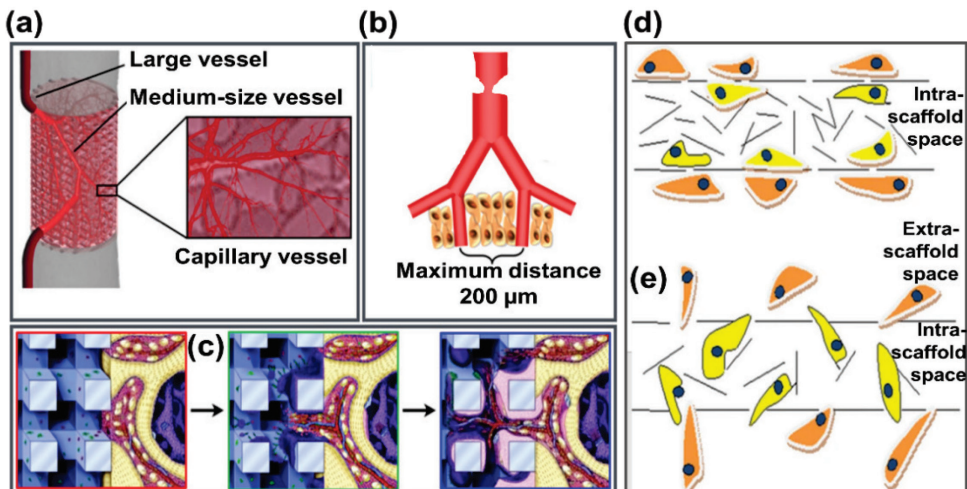


Figure 1.6 Schematic representation showing vascularisation and cell migration through pores in a 3D scaffold: (a) vascular network facilitated by the 3D scaffold; (b) distance between the blood capillaries; (c) bone formation facilitated by an ideal scaffold; (d) indirect cell-cell or cell-ECM communication through pores of size < 10 μm ; (e) cell migration in and out of the scaffold through pores of size 300-800 μm for bone tissue regeneration; adapted from (Bružauskaitė et al., 2016; Kumar et al., 2016; Muschler et al., 2004)

1.3.2 Mechanical compliance

The mechanical properties of scaffolds should comply with the natural bone (either cortical or trabecular) to provide the necessary support and facilitate bone regeneration. The compressive strength and elastic modulus are the crucial parameters in determining the location of the implant. The compressive strength and elastic modulus of the cortical bone are in the range of 170-193 MPa and 10-20 GPa, respectively and those of the trabecular bone are in the range of 7-10 MPa and 0.5-1.5 GPa, respectively (Murugan et al., 2005). A well-designed scaffold should have a fine balance between the elastic modulus and compressive strength to avoid the so-called “stress shielding” phenomenon, and other complications, such as implant-related osteopenia or revision of surgery (Sumner et al., 1998). However, owing to the anisotropic compressive strength and elastic modulus properties of the bones, as shown in Fig. 1.7 (cortical [midfemoral], trabecular [proximal tibia or axial femoral]), it is very difficult to design an ideal scaffold for bones.

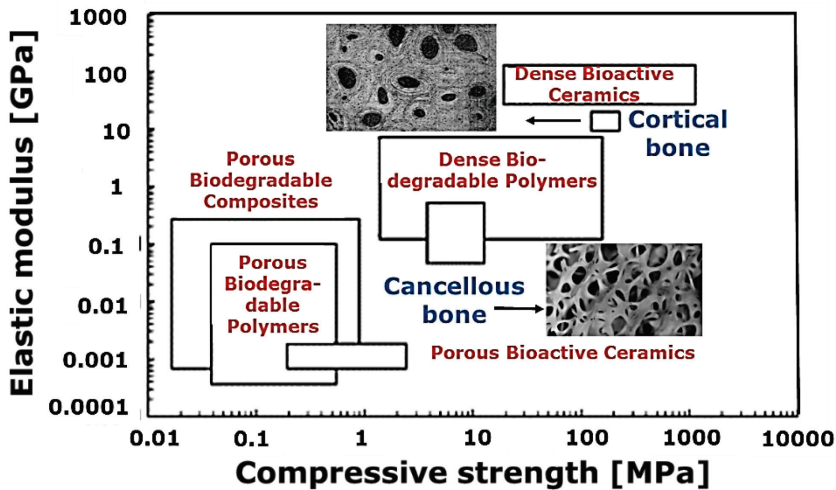


Figure 1.7 Elastic modulus vs compressive strength of porous bioceramic and polymer scaffolds for BTE (adapted from (Rezwan et al., 2006)), depicting bone morphologies of compact bone human femora and trabeculae in human bone (S. Wu et al., 2014)

The stiffness of the scaffold is regarded as an effective parameter that enhances osteogenesis. The cells adhering to the scaffold can differentiate in the presence of a mechanical stimulus. Chen et al fabricated 3D composite scaffolds (collagen-HAP) with a differential stiffness values and similar microstructures, which resulted in a wide range of expression levels of osteoproteins in vitro (Chen et al., 2015). Cells customarily receive mechanical feedback from the scaffold to which they adhere, and the chosen stiffness of the biomimetic matrix for a pre-mineralised bone regeneration should be > 30 kPa (Breuls et al., 2008).

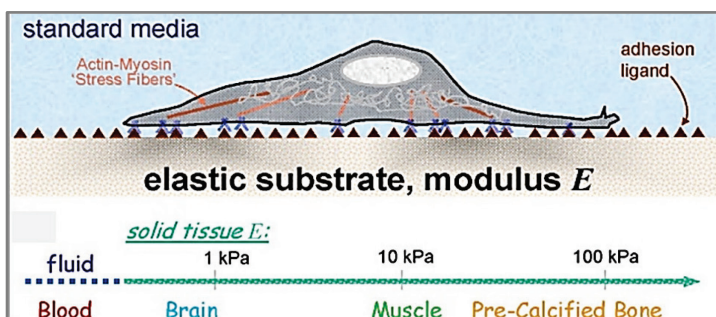


Figure 1.8 Elasticity of the bone tissue with blood as the fluid tissue; adapted from (Rehfeldt et al., 2007)

1.3.3 Bioactivity, biocompatibility, and biodegradability

The other common prerequisites for the scaffolds are bioactivity, biocompatibility, and biodegradability. The bioactivity and biomineralisation can be defined as the formation of HAP crystals, CaP like compounds, and apatite on the surface of a biomaterial. The materials that usually display the phenomenon of biomineralisation are called osteoconductive. Usually, deposition of the biomimetic-like compounds on the scaffolds favours cell attachment, proliferation, differentiation and enhanced hydrophilicity (Tang et al., 2013). Tailoring the surface chemistry (Lee et al., 2009) by increasing the partial pressure of carbon dioxide in the SBF (Cai et al., 2011) and hydrothermal synthesis to coat apatite nanostructures at 150 °C in the SBF (Abdal-hay et al., 2013) can expedite the bioactivity of the scaffolds.

Bioactivity is generally accompanied by cytocompatibility or biocompatibility. The scaffold should not be toxic and should aid cell attachment, proliferation, differentiation, and finally ossification (Anselme, 2000). The scaffold should act as an ideal matrix to support the cells adhering to its surface. Additionally, over time (incubation time in days), cells should exhibit a higher density of cultured cells (Ni et al., 2006). The aforementioned behaviour was observed in silicate-based scaffolds, where the cell culture in vitro after seven days maintained physical contact with the neighbouring cells through cytoplasmic extensions (Ni et al., 2006). The silicate-based scaffolds for BTE have shown a preferential attachment of the osteoblasts, usually on the pore walls (Wu et al., 2010). A comparison of the biocompatibility between silicate-based ceramics (akermanite) and β -TCP revealed an upregulated expression of osteogenic marker genes, such as OCN, OSP, and BSP in the scaffolds made of the former (Huang et al., 2009).

Resorption or biodegradability is the dissolution or degradation of the biomaterials in an in vivo or in vitro microenvironment. The dissolution of the biomaterial is an essential pre-requisite for BTE scaffold so that there is an equilibrium between the resorption of the scaffold by the neighbouring tissue and the immediate mechanical support to the fractured bone.

The degradation of bioceramic-based scaffolds can be understood in the following sequence. Firstly, the dissolution of the degraded products from the scaffold leads to an alteration of the local pH. Secondly, some newly formed biomimetic phases, such as HAP are accumulated on the surface of the scaffold. The aforementioned degradation of the products from the scaffolds occurs at specific crystallographic planes, inducing grain boundaries (Kamboj et al., 2019). Thus, the degradation of the scaffolds is governed by

the grain size, crystallinity, scaffold pore size, porosity, and particle size distribution (LeGeros, 1993). Thirdly, the activation of the phagocytosis, macrophages, osteoclasts, and osteoblasts decreases the pH of the local microenvironment. Lastly, the dissolution of the grains and the particles from the scaffold is slowly reconstituted by the growth of the bone (LeGeros, 1993).

1.4 Crystalline and porous silicon for BTE

Silicon, a commonly used semiconductor material, possesses all the required properties needed for BTE. In addition, porous and/or polycrystalline silicon has a significantly higher mechanical strength compared to the relatively available resorbable polymers (PCL, PLLA) used in orthopaedic implant materials; hence, the former is more suitable for load-bearing applications (Aston & Canham, 2007). The use of silicon is also advantageous, as the degradation or the corrosion of the silicon particles leads to the formation of silicic acid, a chemical well known for simulating the bone growth, and that can be passed down by the body easily (Aston & Canham, 2007). J.D Birchall proved that the deficiency of the silicon was responsible for the defective collagenous connective tissue and defects in the proper growth of the bone at the fractured area (Birchall, 1995). Sun et al were the first to investigate the potential of porous silicon as a novel cell interface for BTE (Sun et al.,2007). They manufactured three different porous silicon architecture varieties, namely nano-architecture (<20 nm), meso-architecture (approximately 50 nm), and macro-architecture (1 μm to 10 μm), using the anodisation technique. Interestingly, when a comparative analysis was performed, they observed that the macro-porous silicon performed better than the meso-porous and nano-porous varieties in supporting the attachment of the osteoblasts and their proliferation (Sun et al., 2007). This is shown in Fig. 1.9.

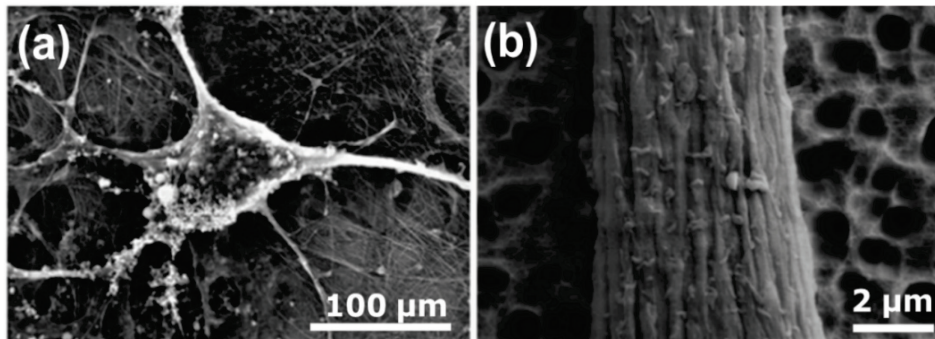


Figure 1.9 (a) SEM images of the osteoblast attachment; (b) type I collagen fibre bundle onto macro-porous silicon; adapted from (Sun, 2007)

Macro-porous silicon also possesses the property of integrating adenovirus coated with BMP (Sun, 2007). The feasibility of the direct coating method to incorporate the virus coated BMP onto the macro-porous silicon exhibited the potential to infect cells and foster osteoinduction (Sun, 2007). At the same time, macro-porous silicon can support bone regeneration. The potential of the macro-porous silicon to repair the bone in vivo in mouse tibia is also significant (Sun, 2007). The large surface to volume ratio and adjustable surface chemistry of the porous silicon make it an interesting candidate for drug delivery and scaffolding (Sun et al., 2007).

1.5 Objectives

This research was motivated by a critical need for reliable and repeatable processing of controllable and customised scaffolds for BTE, as most of the existing bioceramic composites (metal-bioceramic and polymer-bioceramic composites), which are specified in Fig. 1.10, experience many inherent processing difficulties attributed to the removal of the binder, geometric constraints, and subsequent sintering. They also entail other excessive post-processing steps, which not only are tedious but also leads to the deterioration of characteristic features (physical-chemical) of the scaffolds. To plug these loopholes, the overall objective of the work was to design new silicon-bioceramic formulations, employing AM through SLM, to obtain scaffolds for BTE with uncompromising mechanical properties, and without the need of subsequent binder addition and/or thermal treatment.

Thus, this work aimed to use SLM as a 3D tool to shape novel pseudo-metal-ceramic composites using acicular wollastonite and 62 W glass ceramics. It must be emphasised that the unique and novel 62 W glass ceramic was designed to have 70 vol.% of ceramic and 30 vol.% of glass.

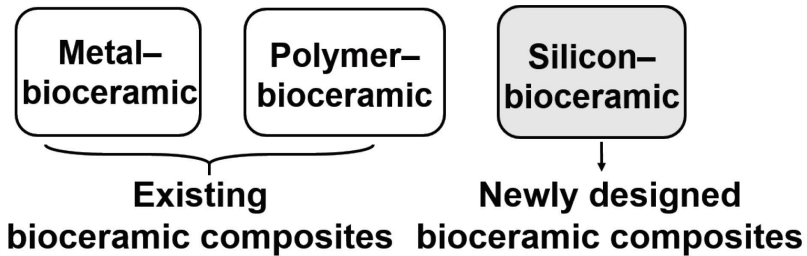


Figure 1.10 Primary objective of this work

The scientific goals of the present research described in this thesis were to:

1. reveal the phases formed after the interaction of the newly designed silicon-bioceramic feedstock powder with a YAG laser;
2. disclose important aspects of the microstructural features of the scaffolds, associated with their mechanical properties and enhancing the mechanical properties of the scaffolds by tuning the biomimetic CAD design;
3. assess the bioactivity and cytocompatibility of the scaffolds;
4. study the *in-vitro* osteoblastic differentiation potential of hMSC onto the scaffolds with a different biomimetic design;
5. study the ability of the scaffolds to deliver biological moieties; and

The technological goals of the present study were to:

1. optimise the laser power and co-relating them with the characteristic features of the scaffolds;
2. develop process parameters for the fabrication of the silicon-bioceramic composites using SLM; and

3. study the transition in the compressive strength of the scaffolds (towards the load-bearing component of the bone) by altering the amount of ceramic content (in wt.%) in silicon-bioceramic metalloid composites.

A major part of the work was concentrated on (i) optimisation of the SLM process parameters (ii) characterisation and functionalisation of the silicon-acicular wollastonite/62 W glass composite scaffolds, and (iii) evaluation of the biological response of the composites.

2. Experimental

2.1 Powder feedstock

The powders for the feedstock for the SLM used were silicon of > 99.9% purity (Silgrain-Elkem), with a particle size ranging from 10 to 44 μm (shown in Fig 2.1(a)) and acicular wollastonite of > 99.9% purity (NYCD[®] M1250), provided by NYCO with particle sizes ranging from 2 to 10 μm (shown in Fig 2.1(b). The 62 W glass composition was prepared, using the ternary phase diagram of $\text{CaSiO}_3\text{-MgCa}(\text{SiO}_3)_2\text{-Ca}_3(\text{PO}_4)_2$ (Sara Rodrigo-Vázquez et al., 2020), and by blending a mixture of SiO_2 (> 99.7% purity) (Strem Chemicals), CaCO_3 (> 98.5% purity) (Merck KGaA), MgO (> 97% purity) (MERCK, KGaA), and $\text{Ca}_3(\text{PO}_4)_2$ (Pharma grade; PanReac AppliChem). The experimental weight compositions (in wt.%) were CaO (47), SiO_2 (39), P_2O_5 (10.2), and P_2O_5 (3). The mixture was melted at 1500 $^\circ\text{C}$ in an electric furnace for 2 h. Then, the melted glass was converted to the fritted glass by pouring cold water on the melted glass. Subsequently, the fritted glass was milled in a vibrating cup mill, and sieved below 45 μm . The final particle size distribution was analysed using a Mastersizer S (Malvern, England), with a medium particle size of approximately 2.5 μm (shown in Fig. 2.1(c)).

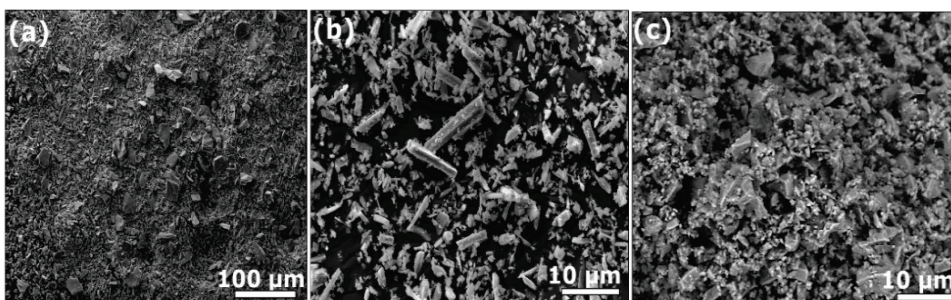


Figure 2.1 SEM images of the powder precursors: (a) silicon; (b) acicular wollastonite; (c) 62 W glass

Different formulations of silicon-wollastonite and silicon-62 W glass were prepared. The initial composition was started with 50 wt.% silicon and 50 wt.% of the ceramic phase for the powder feedstock for SLM (shown in Fig. 2.2(a-b)). Consequently, with aim of increasing bioactive ceramic phase in the scaffolds and expediting the degradation rate, wollastonite and 62 W glass phase was increased upto 70wt.% in the silicon-wollastonite and silicon-62 W glass composite scaffolds respectively. The powders were homogeneously mixed in a Turbula[®] shaker mixer for 3 h using ZrO_2 balls. The composite powder mixture was parched in an oven heated to 120 $^\circ\text{C}$ for 24 hours.

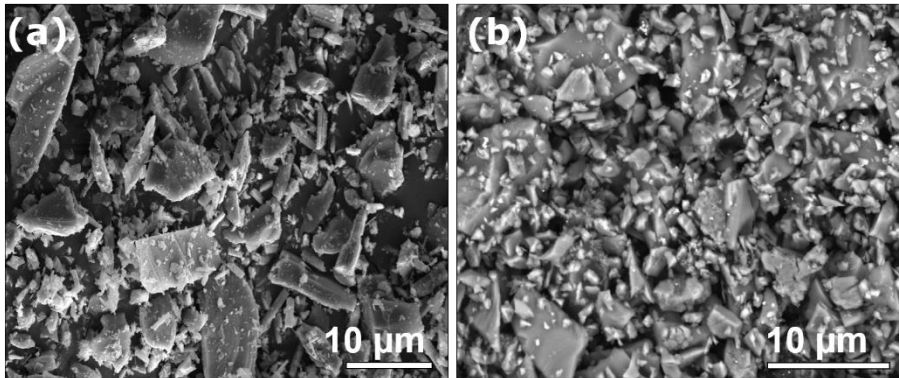


Figure 2.2 SEM images of the mixed powders: (a) silicon-acicular wollastonite; (b) silicon-62 W glass

2.2 Scaffold design

Three-dimensional scaffolds (diameter and height of 5 and 6 mm, respectively) were fabricated based on a CAD software (SOLIDWORKS®; Dassault Systemes, USA), with a pore diameter ranging from 50 to 400 µm. Two types of scaffolds, homogenous and gradient were designed, taking into consideration the importance of the pore sizes for the bone ingrowth, proper infiltration of the body fluids, and vascularisation, as discussed, in detail, in Section 1.31. The gradient scaffolds were designed to have a gradient in the pores in both radial and axial directions. This could have several implications, as a gradient is radially exhibited by the long bones and axially by the flat bones. In addition, solid cylindrical structures were also designed to have the same dimensions as of the porous scaffolds to study and compare the mechanical properties.

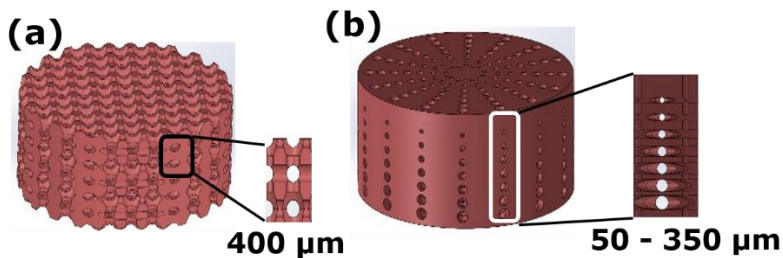


Figure 2.3 CAD model depicting pore sizes of (a) homogeneous; (b) gradient scaffolds

2.3 Fabrication of scaffolds by SLM

A Realizer SLM50 (Realizer GmbH, Germany) machine, whose schematic is shown in Fig. 2.4, was used to fabricate the scaffolds for BTE by using the powder precursor, shown in Fig. 2.2(a-b) equipped with continuous-wave laser. The machine was supplied with a gaussian laser beam and a maximum power of 120 W and a wavelength of 1.07 µm. High purity argon (99.999 vol.%) filled in the working chamber obstructs oxidation of the powder. A rubber wiper outspread the composite (silicon-ceramic) powder feedstock on top of the cylindrical stainless steel platform. During the scaffold fabrication, pure silicon base plate was printed on the bottom followed by scaffold printing and consequently base plate was removed after the scaffold printing.

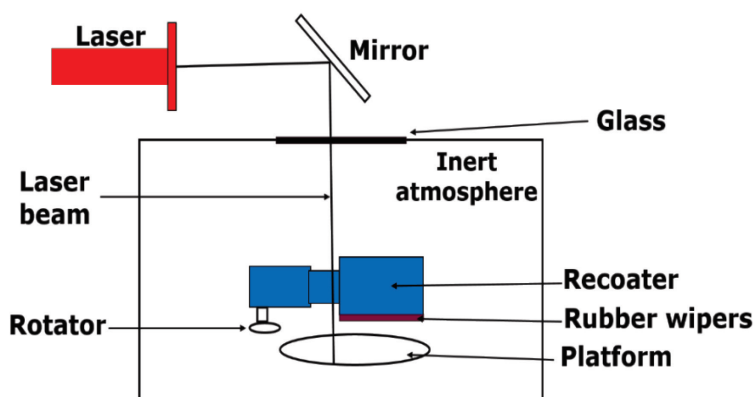


Figure 2.4 Schematic representation of the SLM chamber

Process parameters, such as laser power, layer thickness, scanning speed, and energy density, were carefully monitored for macro-porous silicon, silicon-wollastonite and silicon-62 W glass scaffolds (Table 2.1). Deeper analyses correlating the energy density parameters with characteristic features of the scaffolds will be presented in section 3.

Table 2.1 Parameters of the SLM machine and optimised parameters for the scaffolds

Parameter	Equipment parameters (maximum)	Optimised parameters for (silicon-ceramic) scaffolds
Laser power (W)	120	18-35
Scanning speed (mm/s)	1000	80
Point distance (μm)	50	10
Layer thickness (μm)	50	25

2.4 Characterisation of the scaffolds

Scanning electron microscopy (SEM Zeiss EVO MA 15, Germany) was used to study the microstructure equipped with EDS of voltage up to 20 kV and magnifications up to 50,000x.

Phase composition of the squashed scaffolds was accessed by X-ray diffraction (XRD; D5005, Bruker, USA) operating at $\text{CuK}\alpha 1$ radiation ($\lambda = 1.5406 \text{ \AA}$) with a step of $0.02^\circ (2\theta)$ in the range of $20\text{-}80^\circ$. The EVA-version 6.0 Diffract Plus software (Bruker AXS GmbH, Karlsruhe, Germany) was used to examine the peaks in the diffractogram.

Cylindrical porous samples of the dimensions 5 mm and 6 mm (diameter and height) were examined under compression at the ambient temperature and an applied strain rate of 0.5 mm min^{-1} by servo-hydraulic model 8500 universal testing machine (Instron Ltd., UK) and universal testing machine (EM2/200/FR, MicroTest, Spain). The compressive strengths of the scaffolds were also evaluated after drenching them in a Tris buffer solution at a pH of 7.4 and a temperature of 37°C for three, seven, and 14 days, and later parched them at 120°C .

The local and global stress distribution on the scaffolds were also analysed computationally using the FE method with a persistent deformation rate of 0.5 mm min^{-1} to be in congruent with the experimental deformation under uniaxial compression.

The computation of the local stress distribution was carried through commercial FE software ANSYS® 17.2.

The porosity of the scaffolds were accessed by utilising MXT 225 HU-CT machine (Medix Technology). The visualisation and 3D representation of the scaffold were performed through a μ -CT analyser. Subsequently, identical threshold values were defined to reduce the image noise and differentiate the dense material from the pores. The porosities of some of the scaffolds were also measured by mercury intrusion porosimetry.

The biomimetic method, based on ISO 10993 was used to examine the bioactivity of the scaffolds. The scaffolds were soaked in an SBF solution. The flasks were continuously monitored with the passage of days which were placed inside an incubator at a controlled temperature of 37 °C. The bioactivity of the scaffolds was assessed after 3, 7, and 14 days, followed by an analysis of the biomimetic HAP formation.

The deposited HAP layer or the globules on the scaffolds was characterised by confocal RAMAN spectroscopy (Ramanscope 1000, Renishaw Plc) using a 514.5 nm (for silicon-wollastonite) and 785 nm (silicon-bioactive glass) laser line with 10% of the laser power with the microscope objective of 50x. The Raman spectra were collected over a range of 1500-200 cm^{-1} with the measuring conditions of 10 s exposure time. The weight reduction of the constructs immersed in the Tris buffer solution after three, seven, and 14 days (ratio of the solution volume to construct mass: 1 L/g), and parched at 120 °C were evaluated using a precision balance. Ion dissolution from the scaffolds was carried out by inductively coupled plasma atomic emission spectrometry (ICP-AES, Vista AX, Varian, Palo Alto, USA).

The scaffolds were coated with PCL by dissolving 7.5 wt%/v and 10 wt%/v solutions in dichloromethane for 10 min at 37 °C using a magnetic stirrer. Vancomycin hydrochloride with a concentration of 19.2 mg/mL was added to the coating solution. The constructs with a weight of 5 gm were dipped into the coating solution for 10 min in the vacuum. The weight fluctuations before coating, after coating with PCL was determined with very sensitive analytical balance with the accuracy of 4×10^{-6} . The coated samples with vancomycin entrapped were then placed in 60 mL vials containing the SBF, and revolved in a shaking incubator at a constant speed of 240 rpm and 37 °C for a specific number of days. The dissolution of the vancomycin from the pores of the constructs were measured by UV/vis spectroscopy at a wavelength of 280 nm.

Subcutaneous adipose tissue was used to acquire human MSCs. MSCs were nourished and grown using DMEM with 10% FBS, 1 mg/ml penicillin, and 0.1 mg/ml streptomycin at 37 °C in 5% CO_2 . To exclude any contamination to the cell culture the constructs were undergone UV-C treatment. The MSCs were seeded on the surface of the constructs in 12-well plate at a density of 4×10^4 cells per well. The visualisation of the cells adhering on the surface of the constructs was conducted using a filamentous actin (F-actin) phalloidin, tagged by FITC (Sigma). The cells were anchored by 4% paraformaldehyde at 48 h after seeding, cleansed by PBS, and permeabilised by 0.3% TRITON X-100 in PBS for 5 min. Then, the constructs were left in Phalloidin-FITC stain for 18 h at 4 °C, in-order to permeate Phalloidin-FITC staining. On the counterpart, the cells cultured on the flat glass which act as a control (i.e., cells grown without constructs) were kept for 2 h at the ambient temperature. The cells were incubated with Hoechst 33342 (Invitrogen, 1 $\mu\text{g}/\text{ml}$) for 10 min in-order to the stain the nucleus of the cells. The phalloidin-stained cells were examined by Nikon Eclipse 80i microscope (Nikon) by performing PBS cleansing procedures.

RNAs were obtained from the cells grown on the constructs by an Invitrogen kit. The cDNAs were synthesised by taking appropriate amount of DNase-treated (Ambion) RNA accompanied with RevertAid reverse transcriptase (Thermo Fisher Scientific). The quality aspect of the cDNA was attested by RT-PCR using house-keeping genes primers (GAPDH) and HOT FIREpol® Master Mix (Solis Biodyne, Estonia). The fold change of the considered gene was computed in accordance to the control after normalisation to the house-keeping gene, utilising the $2^{-\Delta\Delta Ct}$ formula (double difference of Ct). The final values were exhibited as $\Delta Ct = Ct(\text{considered gene}) - Ct(\text{house-keeping gene})$, and $\Delta\Delta Ct = \Delta Ct(\text{treated}) - \Delta Ct(\text{control})$.

The relative gene expression of the considered gene was illustrated as a mean \pm SD and investigated with Student's t-test, through which differences to be statistically significant when $p < 0.05$.

3. Results and discussion

The novel metalloid-based composite scaffolds i.e., silicon-acicular wollastonite and silicon-62 W glass were fabricated by SLM. However, to elucidate the process parameters of the scaffolds, it was essential to perform a parametric study on pure macro-porous silicon. These parameters would provide key information and insights on important parameters, such as laser power and energy density.

3.1 Macro-porous silicon by SLM

Figure 3.1(a-b) shows the SEM images of the SLM fabricated macro-porous silicon scaffolds. The designed pores through the CAD model in Fig. 2.3(a) were well replicated in the 3D printed silicon macro-porous scaffold.

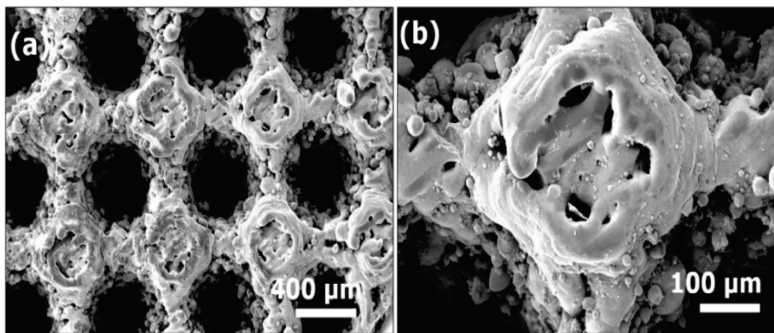


Figure 3.1 (a, b) SEM images of the silicon macro-porous scaffold

The process parameters had numerous effects on the quality of the fabricated scaffolds. A recent study has demonstrated the possibility of the consolidation of the silicon powder by SLM (Minasyan et al., 2018). The study revealed the potential for densification of the silicon powder to a bulk sample with nearly full Archimedes density, and a compressive strength ranging from 337-432 MPa. The findings also suggested that the optimised parameters, namely a laser power of 34 W, scanning speed of 80 mm/s with the single scan track, layer thickness of 25 μm , hatch distance of 60 μm , and energy density of 283 J/mm³ were adequate to consolidate pure silicon. Therefore, some of the parameters were replicated with the implemented CAD design of 400 μm to obtain the macro-porous silicon as shown in Figs. 3.1(a, b). The layer thickness of 25 μm is selected since the particle size have several repercussions on the regulation of the immune response by modulating the ionic microenvironment between the scaffolds and the site of implantation (Y. Huang et al., 2018). The continuous-mode laser facilitated the sintering of the silicon powder and contributed to the formation of the silicon matrix. More detailed information is presented in Paper III. Therefore, considering the parametric study of porous silicon, novel composites of silicon-acicular wollastonite and silicon-62 W glass were fabricated.

3.2 Silicon-wollastonite scaffolds for drug delivery

3.2.1 Processing and characterisation

The 50-50 wt.% of silicon-wollastonite scaffolds were investigated for their ability of drug delivery. However, it is very important to first evaluate the processing parameters, mechanical properties, bioactivity, and biodegradation studies of the scaffolds.

3.2.1.1 Processing and characterisation

As explained briefly in section 3.1, a laser power of 34 W was adequate to consolidate pure silicon. The addition of wollastonite to the silicon powder required optimisation of the parameters for porous silicon-wollastonite scaffolds with a pore size of 400 μm .

Table 3.1. Process parameter optimisation

Specimen	Laser power (W)	Energy density (J/mm^3)	Peculiarity of the scaffold
S1	45	375	More cracks
S2	35	291	Decreased pore size of the scaffold
S3	30	250	Designed pore size with no cracks
S4	22	183	Brittle constructs

Layer thickness and point distance of 25 μm and 10 μm respectively were kept constant throughout the experiments for the fabrication of the scaffolds since it was optimised for the pure silicon powder which eventually facilitates the printing process. The lowest laser power of 22 W led to the formation of brittle constructs. However, on the other hand, higher laser energy ranging from 45-32 W led to more cracks in the scaffolds and decreased the pore size. More detailed information on the specimen and peculiarity of the scaffolds can be found in Paper I. A laser power of 30 W with an energy density of 250 J/mm^3 was optimised for reliable product development for 50-50 wt.% composite.

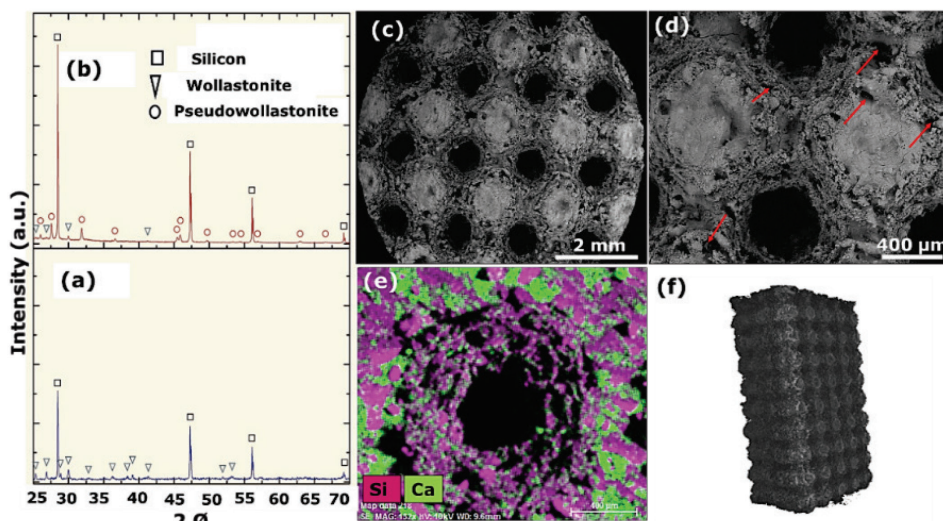


Figure 3.2 XRD patterns of a) powder feedstock; b) silicon-wollastonite crushed scaffold; SEM micrographs of the scaffold with (c) desired pore size; (d) cracks around the pores on the scaffolds depicting residual porosity; e) EDS elemental mapping conducted around the pore; f) CT image of the scaffold

The XRD pattern of the crushed SLM fabricated scaffolds revealed an additional phase of pseudo-wollastonite in Fig. 3.2(b), apart from the silicon and wollastonite phases present in the powder feedstock, shown in Fig. 3.2(a). The propensity of the silicon phase to absorb the YAG laser in Figs. 3.1(a-b) provided sufficient energy to the acicular wollastonite particles to coalesce together with the silicon particles. The interaction between the silicon and wollastonite particles (melt pool) led to the formation of the additional phase of pseudo-wollastonite that can be co-related with the melt pool temperature, as the transition of wollastonite to a higher temperature polymorph i.e. pseudo-wollastonite occurred above 1150°C. Both the wollastonite and pseudowollastonite are regarded as the excellent bioactive, biocompatible materials and simentensously, promoting osteoblasts adhesion and differentiation (Zhang et al., 2013). Figs. 3.2(c-d) represent the SEM images of the scaffolds, which clearly replicated the CAD model shown in Fig. 2.3(a). In addition, the surface depicts some holes indicated with red arrows on the scaffold, which can be regarded as the residual porosity shown in Fig. 3.2(d). The residual porosity could expedite the process of the infiltration of the body fluids and biomolecule impregnation, and ramp-up the degradation process. Fig. 3.2(e) shows the EDS elemental mapping of the scaffolds, illustrating silicon in pink and calcium in green around one pore of the scaffold. This signifies that silicon was formed as a matrix with well-dispersed calcium on the scaffold. Figure 3.2(f) depicts the micro-CT 3D image of the composite scaffold that had a porosity of approximately 35%.

The compressive strength of the macro-porous silicon scaffolds shown in Fig. 3.1(a) was 152 MPa, while that of the scaffold with 50-50 wt.% of each component was found to be 110 MPa under the uniaxial compression. The elastic modulus of the scaffold was 2.9 GPa, which was close to that of metal-based scaffolds for the load-bearing part (cortical-bone) (Tan et al., 2017). In addition, the scaffold immersed in Tris buffer (wet-condition) after 14 days experienced a deterioration in its compressive strength of nearly 18% when compared to the scaffold in the dry condition, as shown in Fig. 3.3(a). More detailed information with regard to the SEM images after 3, 7, and 14 days of immersion of the scaffolds in Tris buffer can be found in paper I.

HAP globules were well recognised and precipitated onto the scaffolds. Fig. 3.3(b) shows a typical cauliflower-like morphology of HAP structures deposited on the scaffolds. The increased magnification at a specific location in Fig. 3.3(b) shows rod-like nanostructures of HAP, as shown in Fig. 3.3(c). The Ca/P was found to be 1.57, which implied the formation of a non-stoichiometric HAP on the as-fabricated silicon-wollastonite scaffolds. The HAP formation was also confirmed with Raman spectroscopy and the HAP profile was used as a standard to compare the HAP deposited on the scaffold. The intense band of symmetric stretching of the P-O bonds, which corresponded to the internal modes of the PO_4^{3-} tetrahedral frequency at 965 cm^{-1} , followed by the bending mode of O-P-O bonds at 432 cm^{-1} , 587 cm^{-1} which authenticated the presence of HAP. Additionally, peak at 965 cm^{-1} can also be assigned to the Si-O stretching mode of the wollastonite (Colomban, 2004), but the main contribution can be attributed to the HAP due to the second Raman peak of wollastonite located at 635 cm^{-1} (assigned to the bending mode of Si-O) which appears only as a faint shoulder joined with the peak at 587 cm^{-1} . Furthermore, an overlapping of the Raman peak of the PO_4^{3-} and Si-O can be occurring at 965 cm^{-1} , but this Raman peak cannot corresponds only to wollastonite since Raman peak at 635 cm^{-1} was a faint shoulder in the spectrum. It can be further supported by the evidence that, the Ca/Si ratio decreased from 1.65 from the fabricated scaffold to the Ca/Si ratio of 0.65 on the 14th day (more detailed in Paper I) of the immersion in Tris

buffer clearly suggesting the dispersion of the wollastonite phase first as compared to the silicon phase in the scanned region. In addition, a sharp signal corresponding to silicon was also seen in the spectrum at approximately 520 cm^{-1} .

Figure 3.3(e) indicates the lixiviation of the Ca and Si ions into the Tris buffer. A progressive increase in two ions was observed in the Tris buffer as a function of the number of days spent. There was an increase in the concentration of Ca^{2+} ions from 125 mg/L on the third day to approximately 200 mg/L on the 14th day. However, on the other hand, the concentration of Si^{4+} ions concentration increased from 70 to 112 mg/L after the passage of the same number of days as in the case of Ca^{2+} ions. These findings suggest and can be correlated with the early nascent bone formation in the fractures of critical size defects, as Ca^{2+} ions (early lixiviation) could induce early osteoblastic genes, with the silicon matrix from the scaffolds still holding the fracture site. It was optimised by Huang et al. that separate release of calcium and silicon ions apart from the lixiviation from the silicate based materials can also impede the inflammatory responses by inhibiting several inflammatory signalling pathways (Y. Huang et al., 2018).

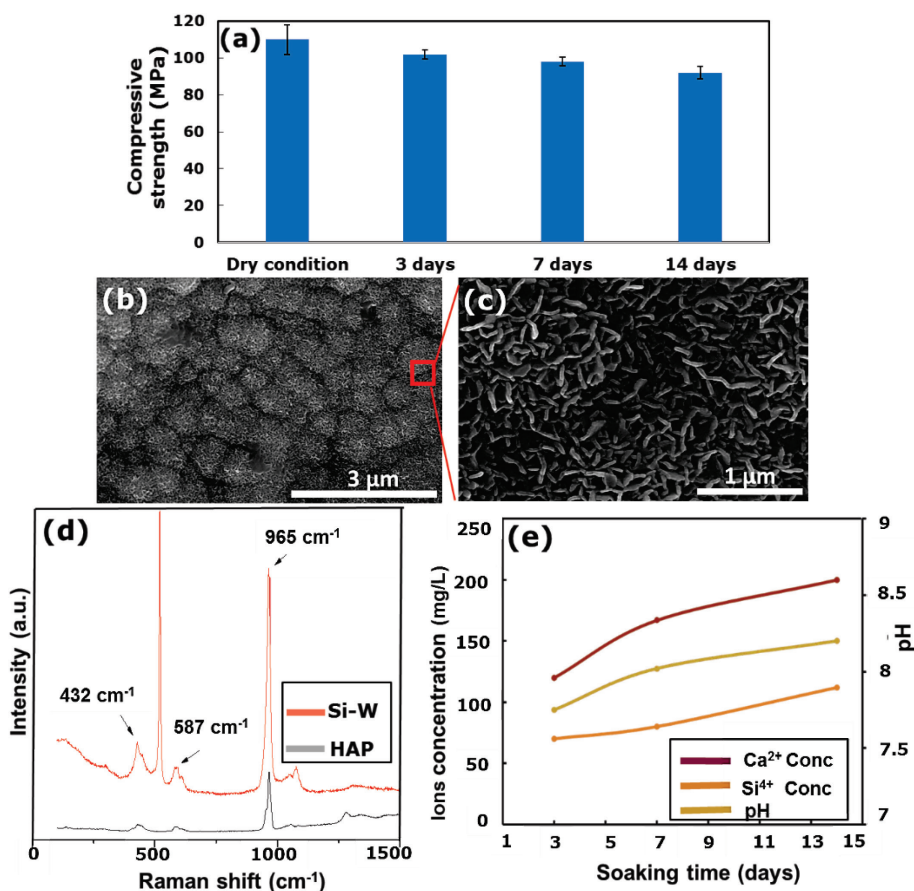


Figure 3.3 a) Comparative analysis of the compressive strength between the dry and wet (Tris buffer) conditions with the passage of days; b, c) HAP globules formation on the scaffolds immersed in the SBF on the 14th day; d) Raman spectrum on the 14th day of the scaffold being immersed in the SBF; e) concentration of ions (Ca and Si) with respective soaking time in days

3.2.2 Vancomycin drug delivery

The as-fabricated scaffolds were also investigated for their potential to deliver vancomycin for wound healing and treating chronic osteomyelitis infections. The scaffolds were coated with differential PCL in wt.% dissolved in dichloromethane as shown in the SEM micrographs in Figs. 3.4(a, b). When the coating concentration increased i.e., PCL increased in wt.% from 7.5 to 10% in dichloromethane, some of the pores of the scaffolds were fully clogged as shown in Fig. 3.4(b). The surface of the composite scaffold was entirely covered or surrounded by the PCL coating. Vancomycin was also loaded with a PCL coating. The drug loading capacity of the scaffolds (loaded drug/carrier) reached up to 16.73 ± 0.82 and 17.92 ± 0.5 mg/g for PCL with 7.5 and 10 wt%/v, respectively. The drug release profiles exhibited a two-step process, with an initial burst nearly 50% of the drug-loaded in the first 40 h. This was followed by a sustained release of nearly 20% and 34 % after six days for the PCL coatings with 7.5 and 10 wt%/v respectively. Therefore, the initial coating conditions were decisive for the drug release. The release kinetics of the coated PCL scaffolds could provide the drug to the infected site, and consequently, the antibacterial effects with a sustained release for long-term healing.

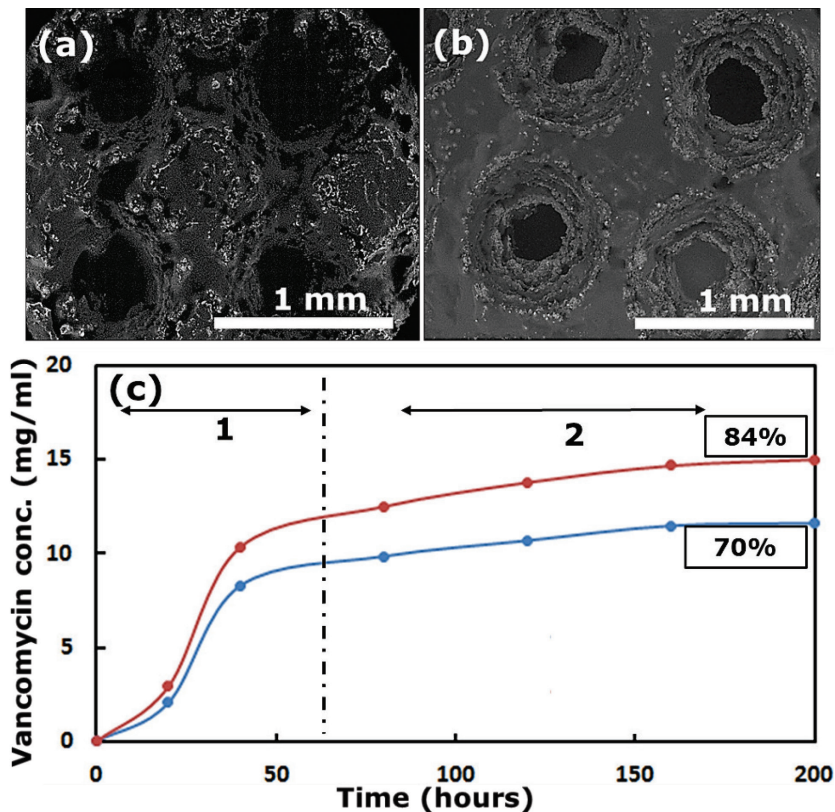


Figure 3.4 a) SEM morphology of silicon-wollastonite scaffolds, coated with a) 7.5 wt%/v of PCL and b) 10 wt%/v of PCL dissolved in dichloromethane; c) Vancomycin release profiles from the scaffolds in blue line curve with 7.5wt%/v and red with 10wt%/v of PCL content signifying 1-fast release and 2-slow release of vancomycin; adapted from Paper II

3.3 Cytocompatibility of silicon-wollastonite scaffolds and gene induction studies

3.3.1 Processing and characterisation

With the aim of having higher bioactive and degradable phase in the scaffolds coupled with more source of calcium in the scaffolds, wollastonite phase in the scaffolds was further increased by 70wt.% as compared to the scaffolds mentioned in Paper I and II with the wollastonite phase of 50wt.% to study osteo-lineage potential. The 70 wt.% acicular wollastonite-30wt.% silicon was evaluated for cytocompatibility and gene induction. The processing parameters and mechanical properties were divergent when compared to their counterparts mentioned in section 3.2.1. Laser power and energy density of 26 W and 217 J/mm³ were provided to the scaffolds; these were lesser than those of the scaffolds mentioned in section 3.2.1 (30 W and 250 J/mm³). This difference could be attributed to the fact that the scaffolds were now involved with a more brittle phase (wollastonite) and therefore, the laser power had to be decreased to obtain a better quality scaffold. More detailed information on the process parameters can be found in Paper III.

Homogeneous and gradient scaffolds were engineered based on the CAD design shown in Figs 2.3(a-b). The gradient scaffolds were designed for definitive bone types, as the long bones present a structural gradient in the radial direction and flat bones present a gradient axially (Di Luca et al., 2016). As a result, varied bone densities of the cortical and cancellous bones were observed in long and flat bones. Considering this fact as the main research ground, a comparative analysis was conducted between homogeneous and gradient scaffolds in terms of their mechanical properties, cytocompatibility and gene induction studies.

Figs. 3.5(a-b) shows the as-fabricated scaffolds by SLM showing differential pore morphology. The gradient scaffold presents a gradient in the pores both radially and axially. The smaller pores could aid in the infiltration of the body fluids, while the larger pores could expedite the bone tissue regeneration process. The homogeneous scaffold displayed four macro-pores connected by an interconnected stem, as shown in Fig. 3.5(a). The porosities of the homogeneous and gradient scaffolds were found to be 41% and 30%, respectively.

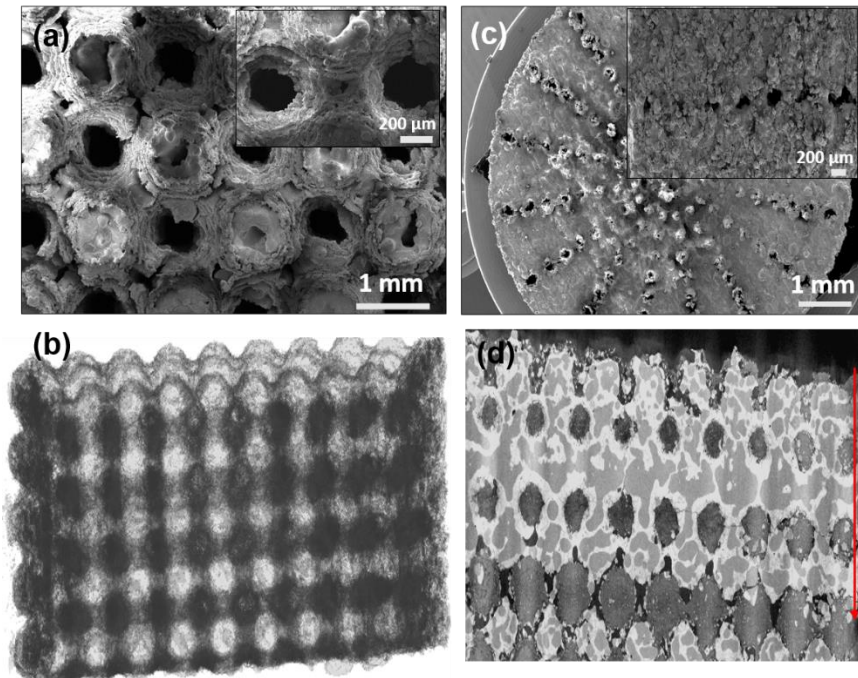


Figure 3.5 Homogeneous scaffold: a) SEM micrograph; b) μ -CT image. Gradient scaffold: c) SEM photograph; d) μ -CT image; adapted from Paper III

The phase analysis showed evidence of an additional phase of pseudo-wollastonite in the crushed SLM fabricated scaffolds apart from the silicon and wollastonite phases present in the powder feedstock. A detailed analysis is presented in Section 3.2.1. In addition, an in-depth analysis can also be obtained in Paper III.

The uniaxial compressive strength and effective elastic modulus of the homogeneous and gradient scaffolds were measured to be 37 MPa and 1.1 ± 0.9 GPa, and 72 MPa and 1.8 ± 0.9 GPa, respectively. Additionally, a difference in the behaviour of the stress-strain curve was noticed between the scaffolds. The homogeneous scaffold exhibited a progressive failure, as shown in Fig 3.6 (a); however, on the other hand, the gradient scaffold demonstrated sudden “incognito” failure zones, as shown in Fig. 3.6(b). The saw-tooth behaviour with the “incognito” failure zones (kinks) can be attributed to the differential stress on the pores of the gradient scaffold. The compressive strength of the scaffolds was greater than that of the cancellous bone (3-11 MPa) but lesser than that of the cortical bone (110-220 MPa) (Barui et al., 2017). However, the strength of the metalloid-based composite scaffold could be further enhanced by increasing the silicon wt.% in the scaffolds meant for the load-bearing component (cortical bone), for example, to 50-50 wt.%, as discussed in section 3.2.1.

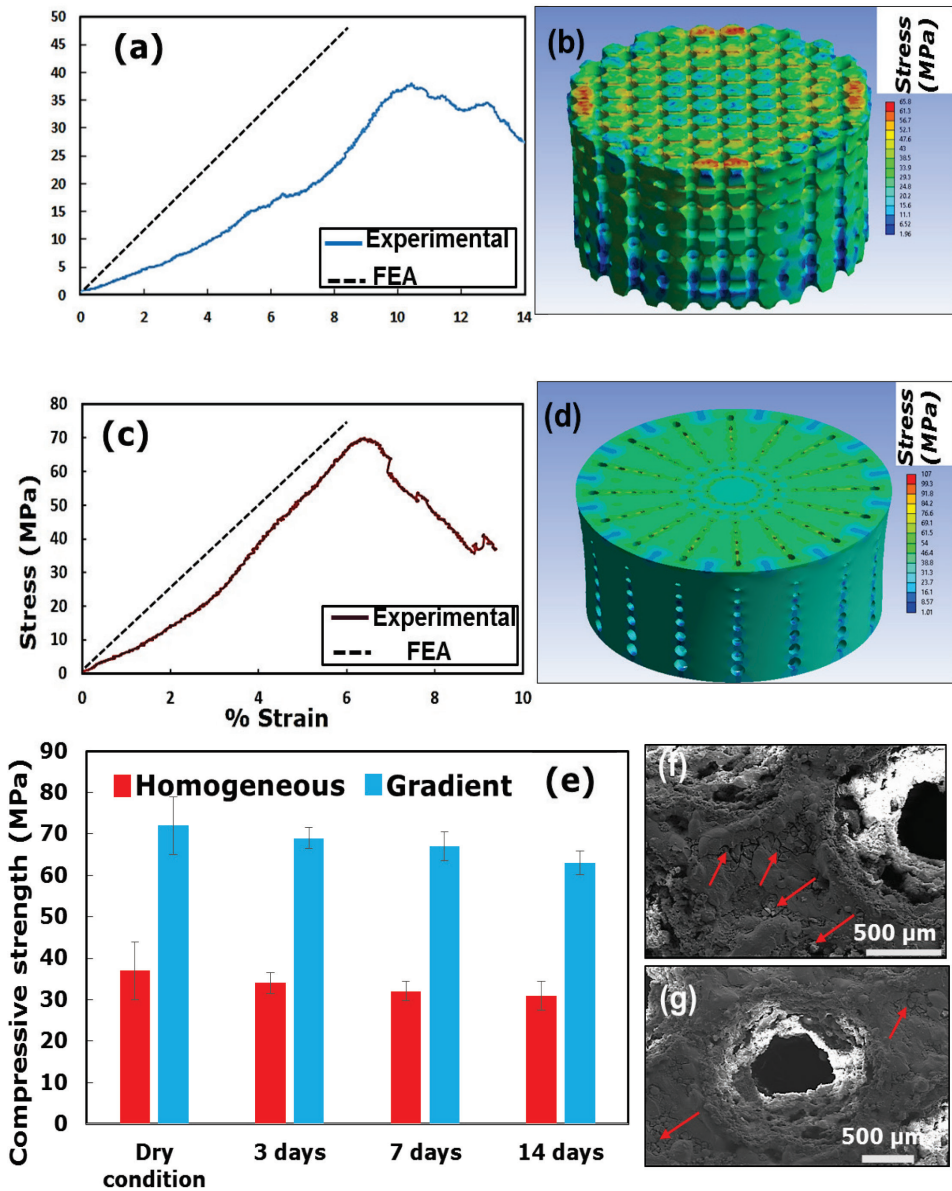


Figure 3.6 Results of the homogenous scaffold: a) comparison of experimental and FEA stress versus strain plot; b) FE stress contours. Results of the gradient scaffold: c) comparison of experimental and FEA stress versus strain plot; d) FE stress contours. e) Compressive strength of the scaffold after soaking in Tris versus number of days. SEM micrographs on the 14th day of immersion: f) homogenous scaffold; g) gradient scaffold; adapted from Paper III

The stress distribution was also evaluated by FE analysis, which was performed only on the linear pattern of the stress-strain curves as shown in Figs 3.6 (a,c); the non-linear part was omitted owing to the rationale of the abatement of the global stress under a constant deformation. The non-linear stress strain part of the curve in FEA as shown in Figs 3.6 (a,c) elicited from 8% and 6% of the strain (%) in the homogeneous and gradient scaffold respectively. Finally, it was concluded down that the estimated deviation from

the experimental compressive strength value for the homogeneous and gradient scaffolds was 21% and 6% respectively. Figs. 3.6(b-d) depict the stress distribution patterns on the homogeneous and gradient scaffolds. The red spots or patches exhibited the majority of the stressed areas, and the greenish-blue areas depict the regions around the pores. The greenish-blue contours correspond to stresses of approximately 77 and 47 MPa for the gradient and homogeneous scaffolds, respectively. In addition, for the scaffold immersed in the Tris buffer (wet-condition) after 14 days, there was a deterioration in the compressive strength of nearly 16% and 12%, respectively for the homogenous and gradient scaffolds as shown in Fig. 3.6 (e). The red arrows indicated in Figs. 3.6 (f-g) show the influence of immersing the scaffolds in the Tris buffer, which resulted in the loosening of the grains. More information is detailed in Paper III.

3.3.2 Assessment of scaffolds for osteo-lineages and cytocompatibility

The spindle-shaped hMSC adhered to the homogeneous and gradient scaffolds considerably. The cells appeared to have extended cytoplasmic lamellopodia, as shown in Figs. 3.7(b-c) depicting proper and suitable interconnectivity, which could be attributed to the 3D micro-environment of the scaffold. More detailed information on the cytocompatibility studies can be obtained from Paper III.

The induction of the osteoblastic genes shows the differential expression on both homogenous and gradient scaffolds. The primary transcription factors RUNX2 and OSX were expressed almost double in the gradient scaffolds when equated to the homogeneous scaffold. Similar trend was observed in the expression of ALP gene (mineralisation). The nascent bone formation (ossification) was also governed by the cytokines, apart from the transcription and mineralisation factors. The expression of the IL-8 and TGF β (anti-inflammatory) factors in as-fabricated constructs depicts the potential immunomodulation effect. The differential expression of the genes could be attributed to different pH values of the culture medium for the MSC culture, different dissolution of ions from the scaffolds into the DMEM medium, and different porosities and pore sizes. However, further deeper analyses are needed for a better understanding.

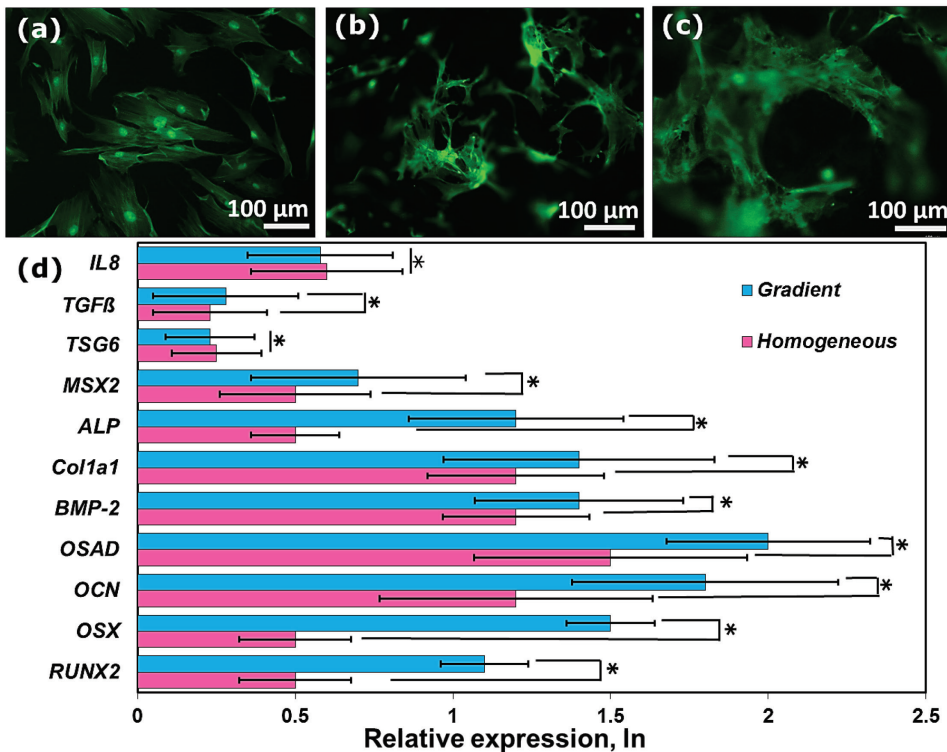


Figure 3.7 hMSC grown on a) glass (control), b) homogeneous scaffold, and c) gradient scaffold; d) qPCR performed on homogeneous and gradient scaffolds showing the dynamic potential of MSC differentiation to osteoblast genes with statistical significance (* $p < 0.05$); adapted from Paper III

3.4 Silicon-62 W glass scaffolds

The other category of scaffolds fabricated was of silicon-62 W glass. The method for the preparation of the novel 62 W glass powder by using ternary phase diagram of $\text{CaSiO}_3\text{-MgCa}(\text{SiO}_3)_2\text{-Ca}_3(\text{PO}_4)_2$ system was discussed in detail in (Sara Rodrigo-Vázquez et al., 2020). The scaffolds were shaped based on varying the 62 W glass wt.% content against that of silicon.

3.4.1 Processing and characterisation

Figure 3.8(a) shows the XRD pattern of the powder feedstocks of 50Si62W, 40Si62W, and 30Si62W. The evidence of the vitreous state of the 62 W glass powder was shown in Fig. 3.8(b), which depicts a broad band between 20 and 40°.

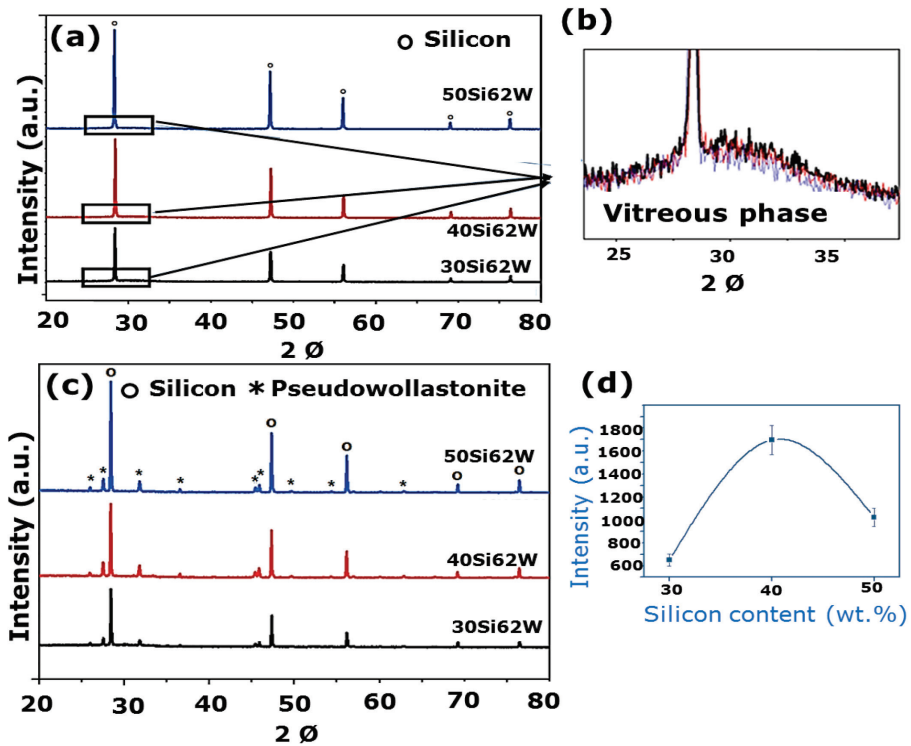


Figure 3.8 a) XRD pattern of the powder feedstock of 50Si62W, 40Si62W, and 30Si62W before the SLM process; b) broad band depicting 62 W vitreous state between 20 and 40 °; c) XRD pattern of the squashed constructs after the SLM process; d) pseudo-wollastonite main peak of (1 3 2) intensity signifying highest rate of crystallization when compared with silicon in wt.% of silicon-62 W scaffolds; adapted from Paper IV

The scaffolds were fabricated based on the process parameters described in detail, in Paper IV. The appearance of the pseudo-wollastonite peaks in all scaffolds could be attributed to the partial devitrification process. The polymorphic transformation of the wollastonite to a higher temperature polymorph (pseudo-wollastonite) for the pure system usually occurs above 1150 °C (Eitel, 1951; Ibañez et al., 1993). However, depending on the annealing time, the presence of this phase could also be detected at lower temperatures (900-1000 °C) (Barbieri et al., 2008; Maeda et al., 2013). Therefore, in our case, during the SLM process, the presence of the pseudo-wollastonite phase suggests that the temperature definitely increased to more than 900 °C of the vitreous glassy particles in all the compositions. The zenithal rate of the pseudo-wollastonite crystallisation was encountered in the 40Si62W construct, which was correlated with the energy density parameter of the SLM process and potent energy absorption by the silicon phase in three different compositions of the silicon-62 W glass scaffolds. This aspect is greatly discussed, in detail, in Paper IV.

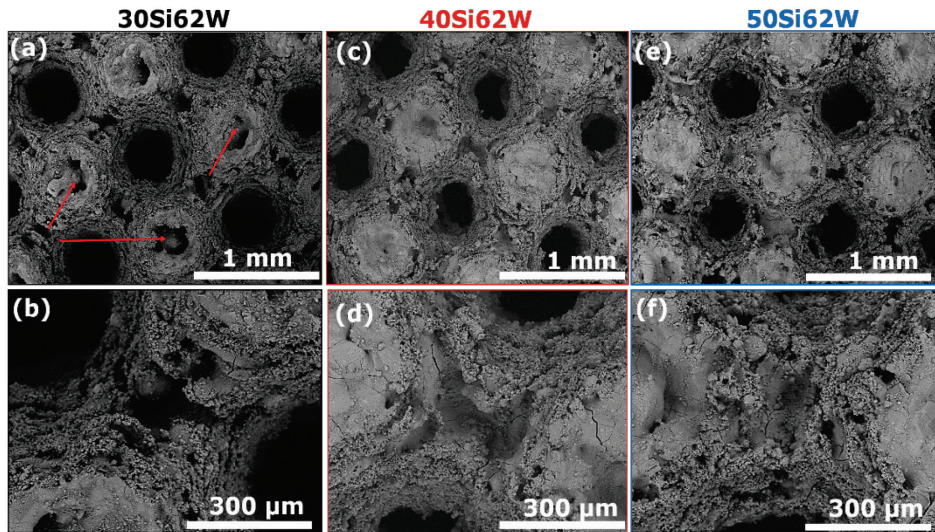


Figure 3.9 SEM micrograph and interconnected wall: a, b) 30Si62W; c, d) 40Si62W; e, f) 50Si62W

Figs. 3.9(a,c,e) show the SEM micrographs of 30Si62W, 40Si62W, and 50Si62W scaffolds, clearly depicting a pore size of 400 μm . It was also noticed that the interconnected stem of the 30Si62W had more residual pores, as indicated by the red arrows in Fig. 3.9(a), as compared to the scaffolds in Figs. 3.9(c-e). This could be ascribed to the addition of extra ceramic component (62 W glass) to the powder feedstock.

The interconnected wall of the scaffolds also had a direct influence on the amount of the ceramic component in the powder feedstock. Figs. 3.9(b,d,f) show the SEM micrographs of the interconnected wall of the as-fabricated constructs. 30Si62W presented the weakest interaction between the sintered particles (Fig. 3.9(b)), followed by 40Si62W and 50Si62W with improved interaction between the sintered particles by the SLM process. The results related to the mechanical properties (compression uniaxial deformation) were also in compliance with the SEM micrographs, with compressive strengths in the order of 50Si62W > 40Si62W > 30Si62W, as shown in Fig. 3.10 with nearly 60% improvement in the compressive strength from the weakest (30Si62W with 8 MPa) to the strongest (50Si62W with 21 MPa) constructs. The maximum strength of the 50Si62W composition could be attributed to the higher silicon (in wt.%) in the composite scaffolds and stronger interaction of the particles at the walls of the scaffolds facilitated by the SLM process.

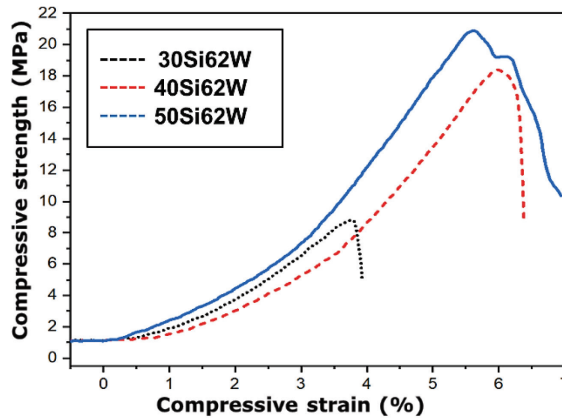


Figure 3.10 Compressive strength versus strain plot of Si-62 W glass scaffolds; adapted from paper IV

3.4.2 Bioactivity of silicon-62 W glass scaffolds

Silicon-62 W glass scaffolds exhibited a relatively good bioactivity response after seven days of immersion in the SBF solution. The rough globular surface and cauliflower-like morphology of the typical HAP was evident from Figs. 3.11(a-c). The EDS signal establishing the calcium and phosphorous implies precipitation of HAP on the surfaces of the scaffolds. In addition, a very dim signal of Mg^{2+} ions was also detected, which could be attributed to the diffusion of magnesium ions into the HAP nanostructures, as Mg^{2+} ions were also added to the powder mixture in the form of MgO. Magnesium substituted or incorporated into HAP was believed to expedite the osteogenesis process (Tao et al., 2016). Raman spectrum on the surface of the scaffolds on the seventh day of all the constructs was done to confirm the HAP formation, discussed, in detail, paper IV.

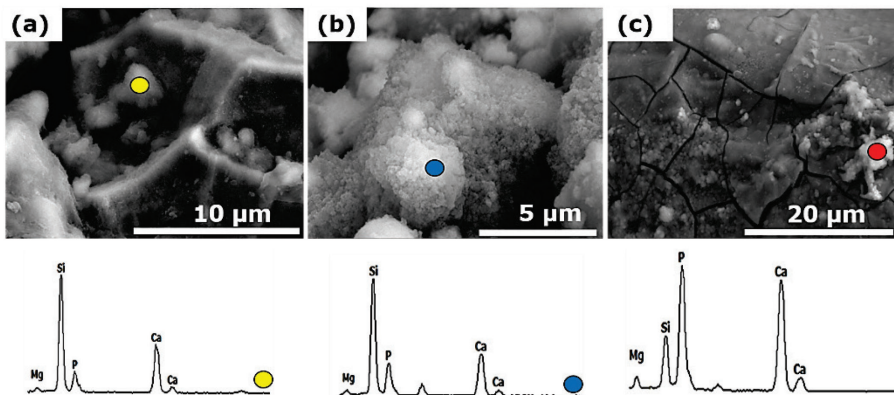


Figure 3.11 FE-SEM images of surfaces after the seven days of immersion in the SBF solution: a) 30Si62W; b) 40Si62W; c) 50Si62W; adapted from Paper IV

Conclusions

In this work, a novel silicon-bioceramic formulation was developed for the fabrication of silicon-ceramic-based composite scaffolds for BTE, using an AM technique, namely selective laser melting. The metalloid-based scaffolds were shaped without any binder addition or geometric constraints, in a single-step and with minor or no post-processing stages. This was accomplished by directly combining osteoconductive elements (wollastonite and 62 W glass). Two types of scaffolds, namely silicon-acicular wollastonite and silicon-62 W glass were fabricated. These scaffolds, fabricated using SLM, yielded promising results with regard to the mechanical properties, delivery of biological moieties, and bioactivity, and as a matrix for cell attachment for bone-tissue regeneration. The following conclusions can be drawn from this study:

1. Analysis of the phases demonstrated an additional pseudo-wollastonite phase in both the scaffolds after the interaction of the YAG laser with the powder feedstocks. The pseudo-wollastonite detected in the Si-62 W glass scaffolds can be attributed to the partial devitrification process induced by the laser.
2. A microstructural assessment of the scaffolds revealed that the addition of ceramic phase into the scaffolds led to a higher porosity and cracking of the final product and, as a consequence, led to a decrease in the compressive strength. Furthermore, altering the biomimetic design by changing the pore size in concurrence with the BTE resulted in a different mechanical strength of the silicon-wollastonite scaffolds, by keeping the same composition of the powder feedstock.
3. The scaffolds were bioactive and resulted in a different morphology of the HAP structures onto the scaffolds, based on the immersion time in the SBF. Additionally, hMSC were well-anchored onto the silicon-wollastonite scaffolds, serving as a potential matrix for supporting the cells.
4. Modulating the bio-inspired CAD of the silicon-wollastonite scaffolds in accordance to the assorted types of bones like long and flat bones eventuated in the differential expression of the primary transcription factors, such as RUNX2 and OSX. Activation of the IL-8 and TGF β , anti-inflammatory factors also designated the potential immunomodulation effect of the scaffolds.
5. The silicon-wollastonite scaffolds also exhibited a potential for sustained delivery of vancomycin.
6. Maximum laser current of 34 W was required to sinter/melt the silicon powder. On the other hand, lesser laser power was needed to shape the silicon-wollastonite (26-32 W) and silicon-62 W glass ceramic (16-22 W) scaffolds.
7. Process parameters with layer thickness of 25 μ m, point distance of 10 μ m, and scanning speed of 80 mm/s were optimised for the silicon-bioceramic composite scaffolds.
8. The silicon-wollastonite scaffolds displayed a compressive strength in the range of 37-110 MPa and the silicon-62 W glass scaffolds, in the range of 8-22 MPa. Therefore, based on the orthopaedic defect site, the scaffolds could be introduced onto a load bearing site (cortical bone) or a non-load bearing site (cancellous bone), by adjusting the ceramic wt.% in the scaffolds.

Scientific novelty and practical importance:

In this work, we have fabricated, for the first time, innovative bioactive porous silicon-wollastonite and silicon-62 W glass substrates for BTE. Unique materials-silicon, with an ability to absorb laser energy and with effective osteostimulation properties, combined with wollastonite and 62 wollastonite glassy ceramic particles with inherent osteoconductive properties were readily shaped by SLM. These metalloid-based composites could be a potential solution for the critical-sized defects ranging from 1.5 to 2.5 cm for the immediate support of the cranial bones or at the metaphysis region of the long bones. The early dissolution of wollastonite or 62 W glass ceramic phase from the composite scaffolds will lead to a nascent bone formation because of the early induction of the osteoblastic genes. However, in-vivo studies are also being conducted on the cranial bone of albino adult rats with calvaria bone defects of 20 mm in diameter to study the degradation of the silicon particles in a real application environment.

References

- Abdal-hay, A., Lim, J., Shamshi Hassan, M., & Lim, J. K. (2013). Ultrathin conformal coating of apatite nanostructures onto electrospun nylon 6 nanofibers: Mimicking the extracellular matrix. *Chemical Engineering Journal*, 228, 708–716. doi: 10.1016/j.cej.2013.05.022
- Aboudzadeh, N., Imani, M., Shokrgozar, M. A., Khavandi, A., Javadpour, J., Shafieyan, Y., & Farokhi, M. (2010). Fabrication and characterization of poly(D,L-lactide-co-glycolide)/hydroxyapatite nanocomposite scaffolds for bone tissue regeneration. *Journal of Biomedical Materials Research Part A*, 94A(1), 137–145. doi: 10.1002/jbm.a.32673
- Amini, A. R., Laurencin, C. T., & Nukavarapu, S. P. (2012). Bone Tissue Engineering: Recent Advances and Challenges. *Critical Reviews™ in Biomedical Engineering*, 40(5), 363–408. doi: 10.1615/CritRevBiomedEng.v40.i5.10
- Anselme, K. (2000). Osteoblast adhesion on biomaterials. *Biomaterials*, 21(7), 667–681. doi: 10.1016/S0142-9612(99)00242-2
- Aston, R., & Canham, L. T. (2007). *US7186267B2 - Porous and/or polycrystalline silicon orthopaedic implant - Google Patents*. Retrieved from <https://patents.google.com/patent/US7186267B2/en>
- Baino, F., Novajra, G., & Vitale-Brovarone, C. (2015). Bioceramics and Scaffolds: A Winning Combination for Tissue Engineering. *Frontiers in Bioengineering and Biotechnology*, 3, 202. doi: 10.3389/fbioe.2015.00202
- Barbieri, L., Karamanov, A., Corradi, A., Lancellotti, I., Pelino, M., & Rincon, J. M. (2008). Structure, chemical durability and crystallization behavior of incinerator-based glassy systems. *Journal of Non-Crystalline Solids*. doi: 10.1016/j.jnoncrysol.2007.07.080
- Barui, S., Chatterjee, S., Mandal, S., Kumar, A., & Basu, B. (2017). Microstructure and compression properties of 3D powder printed Ti-6Al-4V scaffolds with designed porosity: Experimental and computational analysis. *Materials Science and Engineering: C*, 70, 812–823. doi: 10.1016/j.msec.2016.09.040
- Birchall, J. D. (1995). The essentiality of silicon in biology. *Chemical Society Reviews*, 24(5), 351. doi: 10.1039/cs9952400351
- Bolander, J., Ji, W., Leijten, J., Teixeira, L. M., Bloemen, V., Lambrechts, D., Chaklader, M., & Luyten, F. P. (2017). Healing of a Large Long-Bone Defect through Serum-Free In Vitro Priming of Human Periosteum-Derived Cells. *Stem Cell Reports*, 8(3), 758–772. doi: 10.1016/j.stemcr.2017.01.005
- Breuls, R. G. M., Jiya, T. U., & Smit, T. H. (2008). Scaffold Stiffness Influences Cell Behavior: Opportunities for Skeletal Tissue Engineering. *The Open Orthopaedics Journal*. doi: 10.2174/1874325000802010103
- Bružauskaitė, I., Bironaitė, D., Bagdonas, E., & Bernotienė, E. (2016). Scaffolds and cells for tissue regeneration: different scaffold pore sizes—different cell effects. *Cytotechnology*, 68(3), 355–369. doi: 10.1007/s10616-015-9895-4
- Burchard, H. (1983). The Biology of Bone Graft Repair. *Clinical Orthopaedics and Related Research*, NA;(174), 28–42. doi: 10.1097/00003086-198304000-00005

- Cai, Q., Xu, Q., Feng, Q., Cao, X., Yang, X., & Deng, X. (2011). Biomineralization of electrospun poly(l-lactic acid)/gelatin composite fibrous scaffold by using a supersaturated simulated body fluid with continuous CO₂ bubbling. *Applied Surface Science*, 257(23), 10109–10118. doi: 10.1016/j.apsusc.2011.06.157
- Calignano, F., Manfredi, D., Ambrosio, E. P., Biamino, S., Pavese, M., & Fino, P. (2014). Direct Fabrication of Joints based on Direct Metal Laser Sintering in Aluminum and Titanium Alloys. *Procedia CIRP*, 21, 129–132. doi: 10.1016/j.procir.2014.03.155
- Chen, G., Dong, C., Yang, L., & Lv, Y. (2015). 3D Scaffolds with Different Stiffness but the Same Microstructure for Bone Tissue Engineering. *ACS Applied Materials & Interfaces*, 7(29), 15790–15802. doi: 10.1021/acsami.5b02662
- Chen, Q.-Z., Li, Y., Jin, L.-Y., Quinn, J. M. W., & Komesaroff, P. A. (2010). A new sol–gel process for producing Na₂O-containing bioactive glass ceramics. *Acta Biomaterialia*, 6(10), 4143–4153. doi: 10.1016/j.actbio.2010.04.022
- Chen, Z., Xiang, Y., Wei, Z., Wei, P., Lu, B., Zhang, L., & Du, J. (2018). Thermal dynamic behavior during selective laser melting of K418 superalloy: numerical simulation and experimental verification. *Applied Physics A: Materials Science and Processing*. doi: 10.1007/s00339-018-1737-8
- Colomban, P. (2004). Raman spectrometry, a unique tool to analyze and classify ancient ceramics and glasses. *Applied Physics A*, 79(2), 167–170. doi: 10.1007/s00339-004-2512-6
- CSIRO. (2014). *CSIRO produces 3D heel in world first surgery*. CSIRO.
- Di Luca, A., Ostrowska, B., Lorenzo-Moldero, I., Lepedda, A., Swieszkowski, W., Van Blitterswijk, C., & Moroni, L. (2016). Gradients in pore size enhance the osteogenic differentiation of human mesenchymal stromal cells in three-dimensional scaffolds. *Scientific Reports*. doi: 10.1038/srep22898
- Dimitriou, R., Mataliotakis, G. I., Angoules, A. G., Kanakaris, N. K., & Giannoudis, P. V. (2011). Complications following autologous bone graft harvesting from the iliac crest and using the RIA: A systematic review. *Injury*, 42, S3–S15. doi: 10.1016/j.injury.2011.06.015
- Eitel, W. (1951). *Silicate Melt Equilibria*. Retrieved from https://books.google.ee/books/about/Silicate_melt_equilibria.html?id=EHTPAAAAMAAJ&redir_esc=y
- El-Rashidy, A. A., Roether, J. A., Harhaus, L., Kneser, U., & Boccaccini, A. R. (2017). Regenerating bone with bioactive glass scaffolds: A review of in vivo studies in bone defect models. *Acta Biomaterialia*, 62, 1–28. doi: 10.1016/j.actbio.2017.08.030
- Eqtesadi, S., Motealleh, A., Miranda, P., Pajares, A., Lemos, A., & Ferreira, J. M. F. (2014). Robocasting of 45S5 bioactive glass scaffolds for bone tissue engineering. *Journal of the European Ceramic Society*, 34(1), 107–118. doi: 10.1016/j.jeurceramsoc.2013.08.003
- Flynn, J. M. (2011). Fracture repair and bone grafting. *OKU*, 10, 11–21.
- Frazier, W. E. (2014). Metal Additive Manufacturing: A Review. *Journal of Materials Engineering and Performance*, 23(6), 1917–1928. doi: 10.1007/s11665-014-0958-Genera Research Ltd. (2014). *Clinical Trials Register*. Retrieved from <https://www.clinicaltrialsregister.eu/ctr-search/trial/2014-005101-21/HR>

- Gentry, S. P., & Halloran, J. W. (2013). Depth and width of cured lines in photopolymerizable ceramic suspensions. *Journal of the European Ceramic Society*, 33(10), 1981–1988. doi: 10.1016/j.jeurceramsoc.2013.02.033
- Goldberg, V. M., & Akhavan, S. (2005). Biology of Bone Grafts. In Bone Regeneration and Repair (pp. 57–65). Totowa, NJ: Humana Press. doi: 10.1385/1-59259-863-3:057
- Ho-Shui-Ling, A., Bolander, J., Rustom, L. E., Johnson, A. W., Luyten, F. P., & Picart, C. (2018). Bone regeneration strategies: Engineered scaffolds, bioactive molecules and stem cells current stage and future perspectives. *Biomaterials*, 180, 143–162. doi: 10.1016/j.biomaterials.2018.07.017
- Holmes, B., Bulusu, K., Plesniak, M., & Zhang, L. G. (2016). A synergistic approach to the design, fabrication and evaluation of 3D printed micro and nano featured scaffolds for vascularized bone tissue repair. *Nanotechnology*, 27(6), 064001. doi: 10.1088/0957-4484/27/6/064001
- Holmes, D. (2017). Non-union bone fracture: a quicker fix. *Nature*, 550(7677), S193–S193. doi: 10.1038/550S193a
- Huang, S.-C., Wu, B.-C., & Ding, S.-J. (2015). Stem cell differentiation-induced calcium silicate cement with bacteriostatic activity. *Journal of Materials Chemistry B*, 3(4), 570–580. doi: 10.1039/C4TB01617C
- Huang, Y., Jin, X., Zhang, X., Sun, H., Tu, J., Tang, T., Chang, J., & Dai, K. (2009). In vitro and in vivo evaluation of akermanite bioceramics for bone regeneration. *Biomaterials*. doi: 10.1016/j.biomaterials.2009.05.077
- Huang, Y., Wu, C., Zhang, X., Chang, J., & Dai, K. (2018). Regulation of immune response by bioactive ions released from silicate bioceramics for bone regeneration. *Acta Biomaterialia*, 66, 81–92. doi: 10.1016/j.actbio.2017.08.044
- Hutmacher, D. W., Schantz, T., Zein, I., Ng, K. W., Teoh, S. H., & Tan, K. C. (2001). Mechanical properties and cell cultural response of polycaprolactone scaffolds designed and fabricated via fused deposition modeling. *Journal of Biomedical Materials Research*, 55(2), 203–216. doi: 10.1002/1097-4636(200105)55:2<203::AID-JBM1007>3.0.CO;2-7
- Hwa, L. C., Rajoo, S., Noor, A. M., Ahmad, N., & Uday, M. B. (2017). Recent advances in 3D printing of porous ceramics: A review. In Current Opinion in Solid State and Materials Science. doi: 10.1016/j.cossms.2017.08.002
- Ibañez, A., & Sandoval, F. (1993). La Wollastonita: propiedades, síntesis y aplicaciones cerámicas. *Boletín de La Sociedad Española de Cerámica y Vidrio, [En Línea]*, 32(6), 349–361.
- Ingber, D. E., Mow, V. C., Butler, D., Niklason, L., Huard, J., Mao, J., Yannas, I., Kaplan, D., & Vunjak-Novakovic, G. (2006). Tissue Engineering and Developmental Biology: Going Biomimetic. *Tissue Engineering*, 12(12), 3265–3283. doi: 10.1089/ten.2006.12.3265
- Jardini, A. L., Larosa, M. A., de Carvalho Zavaglia, C. A., Bernardes, L. F., Lambert, C. S., Kharmandayan, P., Calderoni, D., & Maciel Filho, R. (2014). Customised titanium implant fabricated in additive manufacturing for craniomaxillofacial surgery. *Virtual and Physical Prototyping*, 9(2), 115–125. doi: 10.1080/17452759.2014.900857

- Jules Poukens. (2011). *The world's first 3D printed total jaw reconstruction*. Total Jaw Implant | Xilloc. Retrieved from <https://www.xilloc.com/patients/stories/total-mandibular-implant/>
- Kamboj, N, Rodríguez, M. A., Rahmani, R., Prashanth, K. G., & Hussainova, I. (2019). Bioceramic scaffolds by additive manufacturing for controlled delivery of the antibiotic vancomycin. *Proceedings of the Estonian Academy of Sciences*, 68(2), 185. doi: 10.3176/proc.2019.2.10
- Kamboj, Nikhil, Aghayan, M., Rodrigo-Vazquez, C. S., Rodríguez, M. A., & Hussainova, I. (2019). Novel silicon-wollastonite based scaffolds for bone tissue engineering produced by selective laser melting. *Ceramics International*, 45(18), 24691–24701. doi: 10.1016/j.ceramint.2019.08.208
- Kato, E., Lemler, J., Sakurai, K., & Yamada, M. (2014). Biodegradation Property of Beta-Tricalcium Phosphate-Collagen Composite in Accordance with Bone Formation: A Comparative Study with Bio-Oss Collagen® in a Rat Critical-Size Defect Model. *Clinical Implant Dentistry and Related Research*, 16(2), 202–211. doi: 10.1111/j.1708-8208.2012.00467.x
- Koc, B., Acar, A. A., Weightman, A., Cooper, G., Blunn, G., & Bartolo, P. (2019). Biomanufacturing of customized modular scaffolds for critical bone defects. *CIRP Annals*, 68(1), 209–212. doi: 10.1016/j.cirp.2019.04.106
- Koons, G. L., Diba, M., & Mikos, A. G. (2020). Materials design for bone-tissue engineering. *Nature Reviews Materials*, 1–20. doi: 10.1038/s41578-020-0204-2
- Krell, E. S., & DiGiovanni, C. W. (2016). The Efficacy of Platelet-Derived Growth Factor as a Bone-Stimulating Agent. *Foot and Ankle Clinics*, 21(4), 763–770. doi: 10.1016/j.fcl.2016.07.002
- Kumar, A., Mandal, S., Barui, S., Vasireddi, R., Gbureck, U., Gelinsky, M., & Basu, B. (2016). Low temperature additive manufacturing of three dimensional scaffolds for bone-tissue engineering applications: Processing related challenges and property assessment. *Materials Science and Engineering: R: Reports*, 103, 1–39. doi: 10.1016/j.mser.2016.01.001
- Lee, M., Li, W., Siu, R. K., Whang, J., Zhang, X., Soo, C., Ting, K., & Wu, B. M. (2009). Biomimetic apatite-coated alginate/chitosan microparticles as osteogenic protein carriers. *Biomaterials*, 30(30), 6094–6101. doi: 10.1016/j.biomaterials.2009.07.046
- LeGeros, R. Z. (1993). Biodegradation and bioresorption of calcium phosphate ceramics. In *Clinical Materials*. doi: 10.1016/0267-6605(93)90049-D
- Liao, X., Lu, S., Zhuo, Y., Winter, C., Xu, W., Li, B., & Wang, Y. (2011). Bone Physiology, Biomaterial and the Effect of Mechanical/Physical Microenvironment on Mesenchymal Stem Cell Osteogenesis. *Cellular and Molecular Bioengineering*, 4(4), 579–590. doi: 10.1007/s12195-011-0204-9
- Lichte, P., Pape, H. C., Pufe, T., Kobbe, P., & Fischer, H. (2011). Scaffolds for bone healing: Concepts, materials and evidence. *Injury*, 42(6), 569–573. doi: 10.1016/j.injury.2011.03.033
- Liu, A., Sun, M., Shao, H., Yang, X., Ma, C., He, D., Gao, Q., Liu, Y., Yan, S., Xu, S., He, Y., Fu, J., & Gou, Z. (2016). The outstanding mechanical response and bone regeneration capacity of robocast dilute magnesium-doped wollastonite scaffolds in critical size bone defects. *Journal of Materials Chemistry B*, 4(22), 3945–3958. doi: 10.1039/C6TB00449K

- Liu, J., & Rynerson, M. (2003). Method for article fabrication using carbohydrate binder. In US Patent 6,585,930.
- Maeda, H., Okuyama, T., Ishida, E. H., & Kasuga, T. (2013). Preparation of porous spheres containing wollastonite by an electrospray method. *Materials Letters*, *95*, 107–109. doi: 10.1016/j.matlet.2013.01.008
- Maradze, D., Musson, D., Zheng, Y., Cornish, J., Lewis, M., & Liu, Y. (2018). High Magnesium Corrosion Rate has an Effect on Osteoclast and Mesenchymal Stem Cell Role During Bone Remodelling. *Scientific Reports*, *8*(1), 10003. doi: 10.1038/s41598-018-28476-w
- Matassi, F., Nistri, L., Paez, D. C., & Innocenti, M. (2011). New biomaterials for bone regeneration. In *Clinical Cases in Mineral and Bone Metabolism*.
- Mazzoli, A. (2013). Selective laser sintering in biomedical engineering. *Medical & Biological Engineering & Computing*, *51*(3), 245–256. doi: 10.1007/s11517-012-1001-x
- Minasyan, T., Liu, L., Aghayan, M., Kollo, L., Kamboj, N., Aydinyan, S., & Hussainova, I. (2018). A novel approach to fabricate Si₃N₄ by selective laser melting. *Ceramics International*, *44*(12), 13689–13694. doi: 10.1016/j.ceramint.2018.04.208
- Miranda, P., Pajares, A., Saiz, E., Tomsia, A. P., & Guiberteau, F. (2008). Mechanical properties of calcium phosphate scaffolds fabricated by robocasting. *Journal of Biomedical Materials Research Part A*, *85A*(1), 218–227. doi: 10.1002/jbm.a.31587
- Miranda, P., Saiz, E., Gryn, K., & Tomsia, A. P. (2006). Sintering and robocasting of β -tricalcium phosphate scaffolds for orthopaedic applications. *Acta Biomaterialia*, *2*(4), 457–466. doi: 10.1016/j.actbio.2006.02.004
- Moreno Madrid, A. P., Vrech, S. M., Sanchez, M. A., & Rodriguez, A. P. (2019). Advances in additive manufacturing for bone tissue engineering scaffolds. *Materials Science and Engineering: C*, *100*, 631–644. doi: 10.1016/j.msec.2019.03.037
- Murphy, C. M., Haugh, M. G., & O'Brien, F. J. (2010). The effect of mean pore size on cell attachment, proliferation and migration in collagen-glycosaminoglycan scaffolds for bone tissue engineering. *Biomaterials*. doi: 10.1016/j.biomaterials.2009.09.063
- Murugan, R., & Ramakrishna, S. (2005). Development of nanocomposites for bone grafting. In *Composites Science and Technology*. doi: 10.1016/j.compscitech.2005.07.022
- Muschler, G. F., Nakamoto, C., & Griffith, L. G. (2004). Engineering Principles of Clinical Cell-Based Tissue Engineering. *The Journal of Bone and Joint Surgery-American Volume*, *86*(7), 1541–1558. doi: 10.2106/00004623-200407000-00029
- Ni, S., Chang, J., & Chou, L. (2006). A novel bioactive porous CaSiO₃ scaffold for bone tissue engineering. *Journal of Biomedical Materials Research Part A*, *76A*(1), 196–205. doi: 10.1002/jbm.a.30525
- Noeaid, P., Li, W., Roether, J. A., Mouriño, V., Goudouri, O.-M., Schubert, D. W., & Boccaccini, A. R. (2014). Development of bioactive glass based scaffolds for controlled antibiotic release in bone tissue engineering via biodegradable polymer layered coating. *Biointerphases*. doi: 10.1116/1.4897217
- Qu, H. (2020). Additive manufacturing for bone tissue engineering scaffolds. *Materials Today Communications*, *24*, 101024. doi: 10.1016/j.mtcomm.2020.101024

- Rehfeldt, F., Engler, A., Eckhardt, A., Ahmed, F., & Discher, D. (2007). Cell responses to the mechanochemical microenvironment—Implications for regenerative medicine and drug delivery☆. *Advanced Drug Delivery Reviews*, 59(13), 1329–1339. doi: 10.1016/j.addr.2007.08.007
- Rezwan, K., Chen, Q. Z., Blaker, J. J., & Boccaccini, A. R. (2006). Biodegradable and bioactive porous polymer/inorganic composite scaffolds for bone tissue engineering. *Biomaterials*, 27(18), 3413–3431. doi: 10.1016/j.biomaterials.2006.01.039
- Roberts, T. T., & Rosenbaum, A. J. (2012). Bone grafts, bone substitutes and orthobiologics. *Organogenesis*, 8(4), 114–124. doi: 10.4161/org.23306
- Roseti, L., Parisi, V., Petretta, M., Cavallo, C., Desando, G., Bartolotti, I., & Grigolo, B. (2017). Scaffolds for Bone Tissue Engineering: State of the art and new perspectives. *Materials Science and Engineering: C*, 78, 1246–1262. doi: 10.1016/j.msec.2017.05.017
- Sara Rodrigo-Vázquez, C., Rodríguez, M. A., & De Aza, A. H. (2020). Devitrification study of a novel bioactive glass designed on the $\text{CaSiO}_3 - \text{Ca}_3(\text{PO}_4)_2 - \text{MgCa}(\text{SiO}_3)_2$ system. *Journal of Non-Crystalline Solids*, 528, 119705. doi: 10.1016/j.jnoncrysol.2019.119705
- Schemitsch, E. H. (2017). Size Matters:Defining Critical in Bone Defect Size! *Journal of Orthopaedic Trauma*, 31, S20–S22. doi: 10.1097/BOT.0000000000000978
- Schindeler, A., McDonald, M. M., Bokko, P., & Little, D. G. (2008). Bone remodeling during fracture repair: The cellular picture. *Seminars in Cell & Developmental Biology*, 19(5), 459–466. doi: 10.1016/j.semcd.2008.07.004
- Sears, N. A., Seshadri, D. R., Dhavalikar, P. S., & Cosgriff-Hernandez, E. (2016). A Review of Three-Dimensional Printing in Tissue Engineering. In *Tissue Engineering - Part B: Reviews*. doi: 10.1089/ten.teb.2015.0464
- Shao, H., Yang, X., He, Y., Fu, J., Liu, L., Ma, L., Zhang, L., Yang, G., Gao, C., & Gou, Z. (2015). Bioactive glass-reinforced bioceramic ink writing scaffolds: Sintering, microstructure and mechanical behavior. *Biofabrication*. doi: 10.1088/1758-5090/7/3/035010
- Simchi, A. (2006). Direct laser sintering of metal powders: Mechanism, kinetics and microstructural features. *Materials Science and Engineering: A*, 428(1–2), 148–158. doi: 10.1016/j.msea.2006.04.117
- Sola, A., & Nouri, A. (2019). Microstructural porosity in additive manufacturing: The formation and detection of pores in metal parts fabricated by powder bed fusion. *Journal of Advanced Manufacturing and Processing*, 1(3), 10021. doi: 10.1002/amp.2.10021
- Steffens, D., Alvarenga Rezende, R., Santi, B., Alencar de Sena Pereira, F. D., Inforçatti Neto, P., Lopes da Silva, J. V., & Pranke, P. (2016). 3D-printed PCL scaffolds for the cultivation of mesenchymal stem cells. *Journal of Applied Biomaterials & Functional Materials*, 14(1), 0–0. doi: 10.5301/jabfm.5000252
- Stevenson, S., & Horowitz, M. (1992). The response to bone allografts. *The Journal of Bone & Joint Surgery*, 74(6), 939–950. doi: 10.2106/00004623-199274060-00017
- Story, B. J., Wagner, W. R., Gaisser, D. M., Cook, S. D., & Rust-Dawicki, A. M. (1998). In vivo performance of a modified CSTi dental implant coating. *International Journal of Oral & Maxillofacial Implants*, 13(6).

- Subia, B., Kundu, J., & C., S. (2010). Biomaterial Scaffold Fabrication Techniques for Potential Tissue Engineering Applications. In *Tissue Engineering*. doi: 10.5772/8581
- Sumner, D. R., Turner, T. M., Igloria, R., Urban, R. M., & Galante, J. O. (1998). Functional adaptation and ingrowth of bone vary as a function of hip implant stiffness. *Journal of Biomechanics*, *31*(10), 909–917. doi: 10.1016/S0021-9290(98)00096-7
- Sun, W. (2007). *Porous silicon based biomaterials for bone tissue engineering*.
- Sun, W., Puzas, J. E., Sheu, T. J., & Fauchet, P. M. (2007). Porous silicon as a cell interface for bone tissue engineering. *Physica Status Solidi (A) Applications and Materials Science*. doi: 10.1002/pssa.200674377
- Tan, X. P., Tan, Y. J., Chow, C. S. L., Tor, S. B., & Yeong, W. Y. (2017). Metallic powder-bed based 3D printing of cellular scaffolds for orthopaedic implants: A state-of-the-art review on manufacturing, topological design, mechanical properties and biocompatibility. *Materials Science and Engineering: C*, *76*, 1328–1343. doi: 10.1016/j.msec.2017.02.094
- Tang, Y., Zhao, Y., Wong, C. S., Wang, X., & Lin, T. (2013). Apatite-coated three-dimensional fibrous scaffolds and their osteoblast response. *Journal of Biomedical Materials Research Part A*, *101A*(3), 674–683. doi: 10.1002/jbm.a.34362
- Tao, Z. S., Zhou, W. S., He, X. W., Liu, W., Bai, B. L., Zhou, Q., Huang, Z. L., Tu, K. K., Li, H., Sun, T., Lv, Y. X., Cui, W., & Yang, L. (2016). A comparative study of zinc, magnesium, strontium-incorporated hydroxyapatite-coated titanium implants for osseointegration of osteopenic rats. *Materials Science and Engineering C*. doi: 10.1016/j.msec.2016.01.034
- Traini, T., Mangano, C., Sammons, R. L., Mangano, F., Macchi, A., & Piattelli, A. (2008). Direct laser metal sintering as a new approach to fabrication of an isoelastic functionally graded material for manufacture of porous titanium dental implants. *Dental Materials*, *24*(11), 1525–1533. doi: 10.1016/j.dental.2008.03.029
- Vagaská, B., Bačáková, L., Filová, E., & Balík, K. (2010). Osteogenic cells on bio-inspired materials for bone tissue engineering. In *Physiological Research*.
- Van Bochove, B., Hannink, G., Buma, P., & Grijpma, D. W. (2016). Preparation of Designed Poly(trimethylene carbonate) Meniscus Implants by Stereolithography: Challenges in Stereolithography. *Macromolecular Bioscience*, *16*(12), 1853–1863. doi: 10.1002/mabi.201600290
- Wang, C., Lin, K., Chang, J., & Sun, J. (2013). Osteogenesis and angiogenesis induced by porous β -CaSiO₃/PDLGA composite scaffold via activation of AMPK/ERK1/2 and PI3K/Akt pathways. *Biomaterials*, *34*(1), 64–77. doi: 10.1016/j.biomaterials.2012.09.021
- Wang, W., & Yeung, K. W. K. (2017). Bone grafts and biomaterials substitutes for bone defect repair: A review. *Bioactive Materials*, *2*(4), 224–247. doi: 10.1016/j.bioactmat.2017.05.007
- Wang, X., Xu, S., Zhou, S., Xu, W., Leary, M., Choong, P., Qian, M., Brandt, M., & Xie, Y. M. (2016). Topological design and additive manufacturing of porous metals for bone scaffolds and orthopaedic implants: A review. *Biomaterials*, *83*, 127–141. doi: 10.1016/j.biomaterials.2016.01.012

- Wu, C., Ramaswamy, Y., & Zreiqat, H. (2010). Porous diopside (CaMgSi₂O₆) scaffold: A promising bioactive material for bone tissue engineering. *Acta Biomaterialia*, 6(6), 2237–2245. doi: 10.1016/j.actbio.2009.12.022
- Wu, S., Liu, X., Yeung, K. W. K., Liu, C., & Yang, X. (2014). Biomimetic porous scaffolds for bone tissue engineering. *Materials Science and Engineering: R: Reports*, 80, 1–36. doi: 10.1016/j.mser.2014.04.001
- Wubneh, A., Tsekoura, E. K., Ayranci, C., & Uludağ, H. (2018). Current state of fabrication technologies and materials for bone tissue engineering. *Acta Biomaterialia*, 80, 1–30. doi: 10.1016/j.actbio.2018.09.031
- Zhang, N., Molenda, J. A., Mankoci, S., Zhou, X., Murphy, W. L., & Sahai, N. (2013). Crystal structures of CaSiO₃ polymorphs control growth and osteogenic differentiation of human mesenchymal stem cells on bioceramic surfaces. *Biomaterials Science*, 1(10), 1101. doi: 10.1039/c3bm60034c
- Ziaee, M., & Crane, N. B. (2019). Binder jetting: A review of process, materials, and methods. *Additive Manufacturing*, 28, 781–801. doi: 10.1016/j.addma.2019.05.031

Acknowledgements

Firstly, I would like to express my special thanks and appreciation to my supervisor Professor Irina Hussainova for her immeasurable support of the thesis. Her guidance in the research is highly appreciated. Her support and encouragement allowed me to follow my dreams and flourish as a research scientist.

I would also like to extend my deepest appreciation to Professor Miguel A. Rodriguez for the common fruitful work and allowing me to use all the required facilities in Spain. Next, I would like to acknowledge and extend my gratitude to PhD. Jekaterina Kazantseva for analysing the scaffolds *in-vitro*; specifically, the discussions on cell-biology aspects are appreciated.

My special thanks to Tatevik Minaysan, PhD. Ramin Rahmaniahranjani, PhD. Roman Ivanov, Ali Saffarshamshirgar, Navid Alinejadian, Javad Karimi, PhD. Neera Singh, PhD. Rocio Rojas Hernandez, Rahul Kumar, Le Liu, PhD. Yaroslav Holovenko, Dr.-Ing. Raghunandan Ummethala, and Abrar Hussain for their friendship. Your positive attitude towards me is highly commendable. Next, my sincere thanks go to Hans Vallner, a brilliant Taltech engineer, who resolved all the technical issues regarding the SLM machine and various other things.

I am grateful to C. Sara Rodrigo-Vazquez, Professor Antonio H. de Aza, PhD. Sofiya Aydiyanyan, Professor Prashanth Konda Gokuldoss, PhD. Fernando Rubio-Marcos, PhD. Lauri Kollo and PhD. Marina Aghayan for the common and productive work.

I owe a lot to my parents and my extended family for their patience and encouragement at every stage of my personal and academic life.

Lastly, I want to dedicate my thesis to my loving wife PhD. Balpreet Kaur. It was not at all easy for both of us to manage together in the field of research; however, her affectionate and endlessly supporting attitude made my thesis work possible. You have been my supporting pillar and I am truly obliged for your practical and emotional support.

This work was partially supported by ASTRA “TUT Institutional Development Programme for 2016-2022”, Graduate School of Functional Materials and Technologies (2014-2020.4.01.16-0032), EU Regional Development Fund, and IUT 19-29 of the Estonian Ministry of Education and Research. The financial support of the European Social Fund’s Doctoral studies and Internalisation Programme DoRa, which is carried out by Foundation Archimedes, as well as Kristan Jaak scholarship, initiated in cooperation with the Estonian Ministry of Education and Research are highly appreciated. Finally, the projects from Estonian Research Council grants PUT1063 and PRG643 (I.Hussainova) are also immensely acknowledged.

I would also like to acknowledge a personal grant with the contract number 2018 186-11, which allowed me to participate at the January 2020 ACerS Winter Workshop, Florida, USA, financed by JECS Trust Board.

Abstract

Additive manufacturing of novel ceramic-based composite scaffolds for bone tissue engineering

Even though osseous tissue is endowed with the inherent property of regenerating itself from small micro-damages and micro-cracks, bone defects greater than 2 cm in size and outstripping critical-sized defects (depending on the anatomical site) do not heal, if left untreated. Additionally, the healing of the osseous tissue fractures poses significant problems, which are further exacerbated by the long-healing time required owing to a lack of knowledge of the precise geometry at the defect site, when conventional bone grafts, such as autografts are used. This can result in a failure of the healing process at the defected site.

New treatment approaches have converged onto bone tissue engineering (BTE) by facilitating the bone tissue formation through 3D scaffolds. The advent of additive manufacturing (AM) allows a precise control of the geometry of the 3D scaffolds, which can potentially mimic the natural features of the bone morphologically and physiologically. Therefore, these 3D scaffolds made by AM are in great demand. The patient's health, age, and the defect site on the bone are the decisive factors for the choice of the materials to be used for the 3D scaffolds. Moreover, assorted biomaterials usually require different AM technologies to be used for biomanufacturing, which is currently a research hotspot for BTE.

One such prominent 3D scaffolds includes bioactive ceramic materials, which can induce either ectopic or orthotopic bone formation. Osteoinductive materials are mostly preferred over osteoconductive materials, as the former contain dissolvable calcium ions, which can be lixiviated to the surface of the scaffolds or growth factors, such as rh-BMP, and rh-PDGF to achieve better clinical outcomes. Osteointegration is another imperative property for BTE, which can be attributed to the material stability for load bearing applications, resulting from the formation of a sturdy bond at the material interphase and bone.

In this work, we have designed a unique combination of novel composite porous bioactive materials by integrating a unique element i.e., silicon into the scaffolds. Novel silicon-wollastonite and silicon-62 wollastonite glass based ceramic composite scaffolds were fabricated by selective laser melting (SLM). The SLM biomanufacturing technique is preferred over the other additive manufacturing techniques because of its ability to present a wider range of the pore size of the scaffolds required for BTE. Silicon, with its ability to absorb laser energy, accompanied by the osteostimulatory effect makes it a potential candidate for BTE. The energy absorbed by the silicon phase allows coalescing of the bioactive ceramic particles. The SLM technique allows printing of the scaffolds in a single-step, without the addition of a binder or the geometric constraints or loopholes, mostly faced by the ceramic-based scaffolds reported in the literature.

A parametric study was also performed onto the novel scaffolds to unravel the printing parameters required to fabricate the scaffolds with proper integrity. An additional pseudo-wollastonite phase was detected in both the scaffolds, apart from the phases present in the constituent powder feedstock. The obtained compressive strength of both the scaffolds encompasses between 8-110 MPa, suggesting their potential to be used both in the spongy bone and cortical bone. It was also inferred that compressive strength of the scaffolds could be modulated by changing the biomimetic design of the scaffolds

and keeping the same composition of the powder feedstock. Furthermore, the scaffolds were also examined in wet conditions (Tris buffer), which indicated plummeting compressive strength values after 14 days. The scaffolds also demonstrated an ability to form HAP onto the scaffolds, illustrating the bioactivity of the scaffolds, which was further confirmed by Raman Spectroscopy.

Lastly, the scaffolds also showed a potential to serve as a supporting matrix for the osteoblasts invasion. The modulation of the biomimetic design of the silicon-wollastonite scaffolds also showed differential transcription factors expression data (RUNX2 and OSX). The scaffolds also stipulated the likely immunomodulation effect by expressing anti-inflammatory factors (IL-8 and TGF- β).

Lühikokkuvõte

Uudsete keraamikal põhinevate komposiitkarkasside kihtlisandustehnoloogia luukoetehnikas

Luustunud kude koos lahutamatu omadusega genereerida iseenesest väikeseid kahjustusi ja mikropragusid ei parane iseenesest kriitiliste luudefektide mõõtmetega üle 2 cm (sõltub anatoomilisest kohast) korral kui neid ei töödelda. Lisaks põhjustab purunenud luustunud koe paranemine märgatavaid probleeme, mis halvendavad tulevikus elukvaliteeti pika paranemisaja tõttu.

Uus lähenemine luukoetehnikas (bone tissue engineering) on koondunud luukoe moodustumisele läbi 3D karkassi. 3D tehnoloogia kasutus tagab täpse kontrolli 3D karkassi geomeetria üle, mis potentsiaalselt võimaldab jäljendada luu morfoloogia iseärasusi ja ka psühholoogiliselt. Siit tulenevalt on suur nõudlus 3D kihtlisandustehnoloogia järele. Üks selline prominentne 3D karkass koosneb bioaktiivsetest keraamilistest materjalidest, mis võivad esile kutsuda väärasetusega või ontoloogiliste luude formeerumist. Osteoinduktiivset luu moodustumist esile kutsuvad materjalid on eelistatud osteokonduktiivsete materjalide ees, kuna esimesed sisaldavad lahustuvaid Ca-ioone, mis võivad kleepuda karkassi pinnale saavutamaks paremaid kasvutegureid ja sellega paremaid kliinilisi väljundeid. Luuintegratsioon on üheks pakiliseks omaduseks luukoetehnikas, mis on oluline materjali stabiilsuse seisukohalt koormustkandvate lahenduste korral-oluline on tugev side materjali ja luupindade vahel.

Käesolevas töös disainiti uued unikaalsed bioaktiivsed materjalid unikaalsete elementide, nt räni kaasamisega karkass-struktuurides. Uudne räni-wollastoniit- ja räni62-wollastoniitklaasi baasil keraamiline komposiitkarkass valmistati selektiivse lasersulatuse (selective laser melting, SLM) teel. SLM biovalmistustehnoloogia on eelistatud teiste kihtlisandustehnoloogiate ees, eelkõige tulenevalt võimalusest saada laiema pooride suuruse vahemikuga materjale luukarkasside tarvis. Räni võimega absorbeerida laseri energiat kaasneb luuteket stimuleeriv efekt, mis teeb need materjalid potentsiaalseteks luukoetehnikas. Ränifaasiga sulamites absorbeerunud energia tagab bioaktiivsete keraamiliste osakeste kleepumist. SLM tehnoloogia võimaldab printida karkassstruktuure ühe etapi käigus ilma sideainete lisamiseta ja piiranduteta geomeetria ja pooride suhtes, mis pole realiseeritav kirjanduses toodud karkass-struktuuride korral.

Uudsete karkass-struktuuriga komposiitmaterjale vajalike valmistusparameetrite väljaselgitamiseks viidi läbi uuringud. Täheledatai täiendava pseudo-wollastoniitfaasi teke karkassi materjalis esinevalt lähtepulbri koostises esinevaist faasidest. Saavutati komposiitmaterjalist karkass-struktuuri survetugevus 8-110 MPa, pakkudes võimaluse nende potentsiaalseks kasutamiseks känd- kui ka kõhrluudes. Selgitati välja, et saadud karkass-struktuuride survetugevus on mõjutatud nende biomeetrilisest disainist sama lähtepulbri koostise korral. Veelgi enam, karkasside omadusi uuriti ka märgades tingimustes. Täheledatai suurepäraseid survetugevuse väärtusi peale 14 päeva. Karkass-struktuure iseloomustas ka hüdroapatiitide moodustumise võime selle pindadel, mida kinnitasid ka Raman spektroskoopia uuringud. Lisaks väljapakutud karkass-struktuurid käitusid toetava maatriksina osteoblastide invasioonil. Räni-wollastoniidi biomeetrilise disaini modulleerimine näitas erinevaid transkriptsioonfaktorite väljundeid (RUNX2 ja OSX). Karkass-struktuuridele oli omane ka nt immuunsusmodulatsiooni efekt läbi põletikuvastaste faktorite (IL-8 ja TGF- β) ilmnemise.

Appendix

Paper I

Nikhil Kamboj, Aghayan, M., Rodrigo-Vazquez, C.S., Rodríguez, M.A., and Hussainova, I., 2019. Novel silicon-wollastonite based scaffolds for bone tissue engineering produced by selective laser melting. *Ceramics International*, 45(18), 24691–24701, doi.org/10.1016/j.ceramint.2019.08.208.

Reproduced with the permission of Elsevier.



Contents lists available at ScienceDirect

Ceramics International

journal homepage: www.elsevier.com/locate/ceramint

Novel silicon-wollastonite based scaffolds for bone tissue engineering produced by selective laser melting



Nikhil Kamboj^a, Marina Aghayan^b, C. Sara Rodrigo-Vazquez^c, Miguel A. Rodríguez^c, Irina Hussainova^{a,*}

^a Tallinn University of Technology, Ehitajate 5, 19086, Tallinn, Estonia

^b FACT-Industries OÜ, Õismäe Tee 124, Tallinn, 13513, Estonia

^c Instituto de Cerámica y Vidrio (ICV-CSIC), C/Kelsen, 5, 28049, Madrid, Spain

ARTICLE INFO

Keywords:

Bioceramic
Scaffold
Bioactivity
Additive manufacturing
Selective laser melting

ABSTRACT

Engineered bone tissue or scaffold is a potential alternative to the common use of bone grafts due to limitless supply and no disease transmission. We present a novel way to manufacture the highly efficient bioceramics combining osteoinductive and bioactive elements using additive manufacturing through selective laser melting without polymer based binder addition and post-processing sintering steps. A formulation of powder feedstock for the production of the scaffolds with an optimized geometry and a high strength is proposed. The structure with circular pores of 400 μm in diameter and porosity level of 35% exhibits density of around 1.4 g/cm^3 and a compressive strength of 110 MPa, which is only slightly decreased after the immersion into Tris buffer for two weeks being of 90 MPa. The scaffolds demonstrate a high bioactivity and a controlled growth of the hydroxyapatite-like layer on the surface of the structures. The results of this work illustrate the ability for fabrication of complex-shaped ceramic based structures to be used as novel bone scaffolds and implants by SLM, and the promise for development of other ceramic – based materials using the proper precursor powders feedstock.

1. Introduction

The appropriateness of additive manufacturing (AM) to tissue engineering is evidenced by the increasing number of research works related to the production of porous scaffolds with custom-tailored architectures. The continuously growing number of surgeries due to injuries, incidence of orthopedic disorders and fractures is a strong driver for the development of bone grafts and/or scaffolds. Moreover, the congenital and acquired pathologies including trauma, infection, neoplasm and failed arthroplasty may result in bone defects being beyond a critical-size; therefore, an invasive surgical intervention to aid healing is often needed [1]. To meet the requirements for synthetic bone substitution materials, the orthopedic devices should represent porous, biocompatible structures with controllable geometry, high surface area, and suitable mechanical characteristics.

Traditionally, the autologous and allogeneic clinical treatments have been used to repair or replace the diseased, infected or lost bone [2]. The auto-grafts are considered as the gold standard in orthopaedic; however, the grafts are restricted in harvested size and represent the further risk of donor site morbidity including infection and ongoing pain following surgery [3,4]. Allograft tissue harvested from cadaveric

and living sources (such as femoral heads removed during hip replacements) is currently widely used. However, allografts carry the potential risk of disease transmission and immune response, whilst lacking a cellular component to aid tissue regeneration. Metalwork and bone substitutes can also be inserted to aid bone regeneration with limitations associated with their use include bone thinning due to stress shielding, wear and failure over time [5]. Non-invasive therapies including ultrasound treatment also demonstrates a promise in aiding bone healing, although their use is often restricted to stable, well-aligned and well-reduced fracture non-unions in adult patients [1,6].

To overcome these drawbacks, the scaffolds made of highly porous and mechanically reliable customized biomaterials with flexibility in design, which can be implanted directly into the injured site, are highly required. For an enhanced therapeutic effectiveness, the scaffolds should be mesoporous structured and have mechanical properties mimicking the natural bone. Table 1 lists the composition, mechanical and physical properties of both cortical and cancellous bones as a guideline for scaffold design.

The bioactive and bio-reabsorbable materials, which are capable of interacting with body tissues, forming chemical or biological bonds and favouring colonisation and tissue regeneration, allow facilitation of the

* Corresponding author.

E-mail address: irina.hussainova@ttu.ee (I. Hussainova).

<https://doi.org/10.1016/j.ceramint.2019.08.208>

Received 12 August 2019; Accepted 22 August 2019

Available online 22 August 2019

0272-8842/ © 2019 Elsevier Ltd and Techna Group S.r.l. All rights reserved.

Table 1
Properties of cortical and cancellous bone.

Property	Cortical bone	Cancellous bone
Composition	Ca ₁₀ (PO ₄) ₆ (OH) ₂ , type I collagen, lipids, non-collagenous proteins, and water	Blood vessels and bone marrow
Compressive strength	100–230 MPa [1,3]	2–12 MPa [4]
Young's modulus	7–30 MPa [1,3]	0.05–1 MPa [4]
Tensile strength	50–151 MPa [1]	1.5–38 MPa [4]
Flexural strength	50–150 MPa [4]	10–20 MPa [4]
Strain to failure %	1–3 [3]	5–7 [7]
Porosity %	2–10 [3]	30–95 [7]
Pore size	10–500 μm [3]	200–400 μm [8]

natural bone growth through the implant, host cells deposition in the matrix without function deviation and degradation being replaced by a new tissue in vivo. The biodegradation rate should be compatible with the natural bone growth rate. The materials should be degradable by host enzymatic or biological processes and allow invading host cells to produce their own extracellular matrix. The bone growth rate is peculiar in different individuals and depends on the age of the patient [4]. Therefore, the scaffolds composition also should be easy adaptable to the patient needs.

The pore structure of the scaffolds is one of the most important parameters for biological performance [6]. To succeed in functionality, the scaffolds should have interconnected pores to enable the cells migration and invasion of vasculature; and should possess a large enough surface area for the active interaction with cells. The incorrect design of porosity can result in necrosis, long healing time and infection [9]. A three-dimensional porous scaffold with an appropriate modulus can provide longevity by reducing stress shielding, which has an influence on the processes of osseointegration and bone healing [10]. In general, the mechanical properties of the bone depends on its type and shape. The mechanical properties of cancellous bone can vary from bone to bone up to 5 times. The cortical bone has a narrower range of difference [7]. Therefore, it is essential to explore the mechanical and biological effects of scaffolds aiming at the optimal design of implants.

In general, silicon and silicon containing bioglasses and bioceramics are considered to have a positive influence on bone mineralization and gene activation. The current trend is equally poised among CaP, bioactive glass, doped and silicates bioceramics, which are used for either trabecular bone or cortical bone as depicted in Fig. 1.

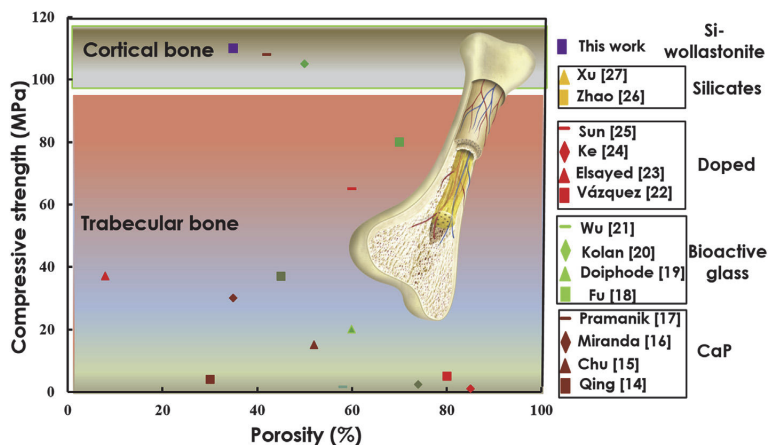


Fig. 1. Graphical summary of compressive strength and porosity of some bioceramic and bioactive glass composite scaffolds, CaP [15–18], bioactive glass [19–22], doped ceramics [23–26] and silicates [27,28].

Wollastonite is another widely used bioceramic material due to its good osteoconductivity and bioresorbability, which has been elucidated in the form of coatings, granules and sintered porous body of a pre-defined shape [11]. Considering the vital role of silicon in the development, repair and maintenance of various tissues, silicon has been widely used as a key element in the design of biomaterials. Silicon exerts a genetic control regulation over the osteoblast cycle and rapid expression of genes [1,12]. Additionally, it facilitates the osteogenic differentiation of mesenchymal stem cells and upregulates osteo-related proteins and production of bone-like apatite [13,14].

There are many methods for the production of bioceramic scaffolds, which includes freeze drying [19], spin coating [29], bioreactors [15], fused deposition modelling [30], hydration method [31], direct ceramic writing [32], stereo-lithography [33] and selective laser sintering [21]. However, most of the production methods encompasses a multi-step technology resulting in highly stressed scaffolds. Furthermore, removal of binder, sintering and other additional post-processing steps are not only time consuming, but also affects the degradation of physical-chemical characteristics of the scaffolds. Using SLM, the 3D complex architectural structures with required pore sizes and porosity level can be generated by computer-controlled design, layer-by-layer printing and sintering process.

Third generation biomaterials are designed to be both osteoconductive and osteoinductive, i.e. to stimulate regeneration of host tissues by combining tissue engineering and in situ tissue regeneration methods [4]. The objective of this study is manufacturing of the highly efficient bioceramic scaffolds by additive manufacturing through selective laser melting (SLM) avoiding any additional post-treatment steps for fabrication of the targeted product. The scaffolds are based on a material that combine both osteoinductive and bioactive elements in their composition.

2. Experimental

2.1. Powder feedstock

The starting powder materials were wollastonite of > 99.9% purity (NYCD® M1250) provided by NYCO with a particle size in the range 2–10 μm and silicon of > 99.9% purity (Silgrain-Elkem) with a particle size ranged from 10 to 44 μm. The powder feedstock for SLM was prepared by mixing 50 wt% of silicon and 50 wt% of wollastonite in the Turbula® shaker mixer for 3 h with ethanol using ZrO₂ balls. The obtained mixture was dried in an oven heated to 120 °C for 24 h.

Table 2
Parameters and conditions of SLM processing.

Parameters	Equipment parameters (Maximum)	Optimized production parameter of scaffolds
Laser power	120 W	20–50 W
Scanning speed	1000 mm/s	80 mm/s
Point distance	50 μm	10 μm
Layer thickness	50 μm	25 μm

Additionally, different silicon ratios starting from 5% to 45% with wollastonite composite were produced and were not used as the starting material since our goal was to maximize silicon in the composite to support osteoblast cell *in vivo*.

2.2. Selective laser melting of Si-wollastonite scaffolds

Metal 3D printer (ReaLizer GmbH SLM-50, Germany) was used for SLM processing of the scaffolds. The YAG: Nd³⁺ laser spot size of 15–80 μm and a computer-controlled laser beam scan velocity up to 1000 mm/s was used to produce the designed structures. Table 2 lists the optimized parameters of operation.

To avoid oxidation and degradation of the powder, the process was carried out in a chamber filled with a high purity argon (99.999 vol%). Fig. 2 schematically shows the process in which a laser beam of 1.06 μm wavelength is focused on the powder bed to develop a pattern according to CAD design. The designed structures represented the rectangular-shaped samples with dimensions of 10x20x5 mm³ and the disks with height of 10 mm and diameter of 6 mm with pore sizes of 400 μm . A rubber wiper spreads the composite powder over the surface of a stainless steel cylindrical platform.

2.3. Characterization of the scaffolds

Microstructure, elemental mapping distribution, and morphology of the scaffolds were studied by scanning electron microscopy (SEM Zeiss EVO MA 15, Germany) equipped with EDS of voltage up to 20 kV and magnifications up to 50 kX before and after the test on bioactivity and degradation. Additionally, the front and cross section details of the scaffolds were investigated using MEDIX technology MXT 225 HU-CT machine. A rotational step of 0.9° over an angle of 180° was implemented to obtain the images of the scaffolds. Phase composition of the samples was analyzed by X-ray diffraction (XRD; D5005, Bruker, USA) operating at CuK α 1 radiation ($\lambda = 1.5406 \text{ \AA}$) with a step of 0.02°

(2 θ) with the assessment and optimization of the relative counts by Rietveld refinement method. Mercury intrusion porosimetry (MIP) was used to calculate the porosity of the scaffolds.

To measure the compressive strength, the cylindrical samples of 6 mm ($\pm 0.1 \text{ mm}$) in diameter and 5 mm ($\pm 0.1 \text{ mm}$) in height were loaded at ambient humidity and temperature with crosshead speed of 0.5 mm/min until crushing failure using servo-hydraulic model 8500 universal testing machine (Instron Ltd., UK). The compressive load and displacement were recorded at 0.1 s intervals during testing. Compressive modulus and maximum compressive strength of scaffolds were determined using software associated with the universal testing machine. All measurements were performed three times per sample, the values were presented as mean \pm SD and analyzed with Student's t-test, which differences were considered statistically significant when $p < 0.05$. The commercial finite element package ANSYS 17.2 was exploited for the evaluation of a local stress distribution and compared with the experimental results. Additionally, the compression tests were conducted on Tris buffer treated samples to provide realistic data on the degradation of the scaffolds.

The bioactivity of the scaffolds was evaluated *in vitro* using the biomimetic method, based on ISO 10993, in which the specimens were immersed in a synthetic body fluid (SBF) solution. The rectangular scaffolds of 5x10x5 mm³ with mass of 1 gm were immersed in 50 ml of SBF clean conical flasks, which were rinsed by HCl and deionised water before using. The conical flasks were placed inside an incubator at controlled temperature of 37 °C. The pH of the solution remained constant at 7.3. The bioactivity of the scaffolds was evaluated for 3, 7 and 14 days, then the analysis of the chemical composition of the surface and its morphology was carried out.

The hydroxyapatite layer on the scaffolds was characterized by RAMAN spectroscopy (Ramanscope 1000, Renishaw Plc) using 514.5 nm laser line. The Raman spectra were collected over the range of 1500–200 cm⁻¹

To study the ion release from the scaffolds and their weight loss, the scaffolds were soaked in a Tris buffer solution for 3, 7 and 14 days (solution volume to scaffold mass: 1 L/g), dried at 120 °C and weighed via an analytical balance. The concentrations of calcium and silicon ions were measured by inductively coupled plasma atomic emission spectrometry (ICP-AES, Vista AX, Varian, Palo Alto, USA).

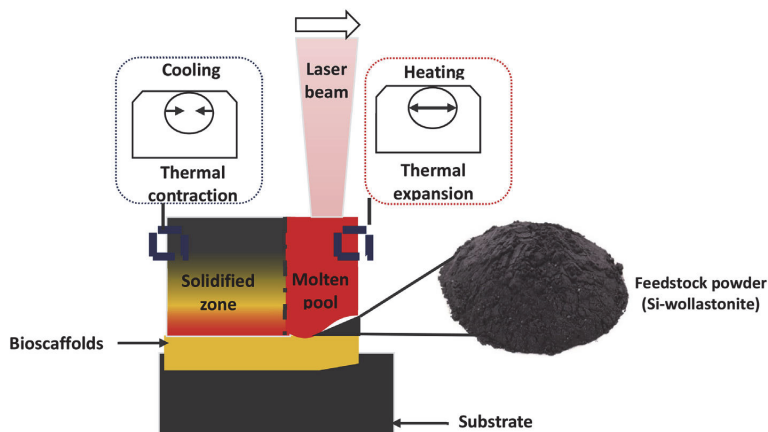


Fig. 2. The scheme of selective laser melting process of Si-wollastonite scaffolds.

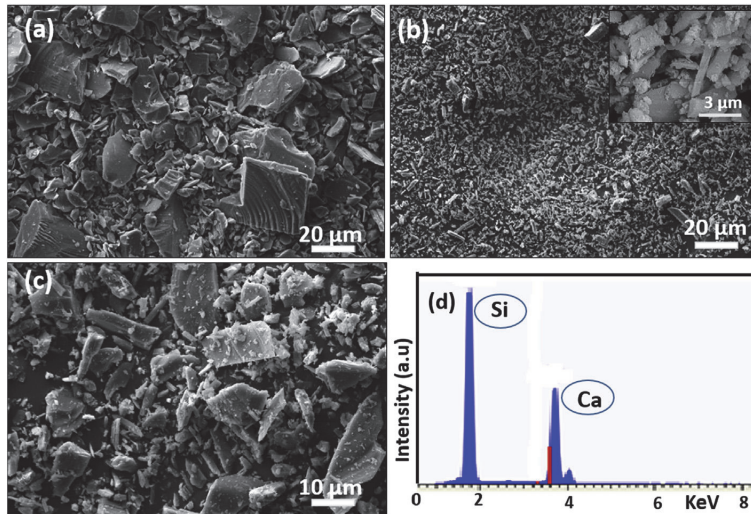


Fig. 3. SEM of the precursor powder: a) silicon; b) wollastonite; c) mixture of silicon (50 wt%) and wollastonite powder (50 wt%); d) Energy dispersive spectroscopy (EDS) of the mixture. (For interpretation of the references to colour in this figure legend, the reader is referred to the Web version of this article.)

3. Results and discussion

3.1. Powder characterization

The SEM images of the precursor powders are shown in Fig. 3a, b. Silicon particles are of irregular shape, while wollastonite particles are of needle-like elongated morphology (acicular). Fig. 3c depicts the SEM micrograph of the resultant composite powder after mixing. The coarse silicon particles act as a substrate coated by acicular wollastonite particles. The needle-shaped wollastonite particles may contribute into an increase in thermal shock resistance and strength of matrix by capturing the force against fracture by hampering and altering crack propagation [34].

3.2. Processing

Fig. 4 (a,b) represents the front and isometric view of the CAD model design. The pore size of biomaterial plays a critical role in bone formation *in vitro* and *in vivo*. The minimum requirement for pore size is considered $\sim 100 \mu\text{m}$ conditioned by the cell size, migration requirements of osteocytes and nutrients transport. However, the pore sizes $> 300 \mu\text{m}$ are recommended due to the boosted formation of a new bone and capillaries. Because of vascularization, the pore size has been shown to affect the progression of osteogenesis [35].

Henceforth, we selected spherical pores of $400 \mu\text{m}$ for the

production of bioceramic-based scaffold by the selective laser melting.

Both the laser energy and energy density have a key influence key influence on the process for the production of the scaffolds. With a relatively high laser current of 50W and 45W, the scaffolds developed a large number of cracks, which can be attributed to unstable and sometimes overheated formation of the exposed powder melt by the laser. Table 3 lists the process parameters for materials sintering.

The powder mixture consists of two types of particles; therefore, there is a unsubstancial temperature gradient in the molten pool, a steep surface tension gradient, and resultant Marangoni flow, which induces capillary forces for the liquid flow [36]. Differently orientated needle-like wollastonite particles are subjected to a significant torque resulting in crack formation. The S3 and S4 samples have reduced pore diameters as the high thermal energy provided by the laser decreases the viscosity of the molten powder allowing formation of the large droplets occupying the pore volume. With relatively low laser current results in brittle and easily breakable S7, S8 and S9 samples. Hereafter, the laser power of 30 W was considered as the optimal power for reliable product development.

3.3. XRD analysis and microstructure of as-fabricated scaffolds

The XRD spectrum of the feedstock powder and crushed scaffold materials after processing of the scaffolds are represented in Fig. 5 (a,b) illustrating presence of silicon, wollastonite and pseudowollastonite

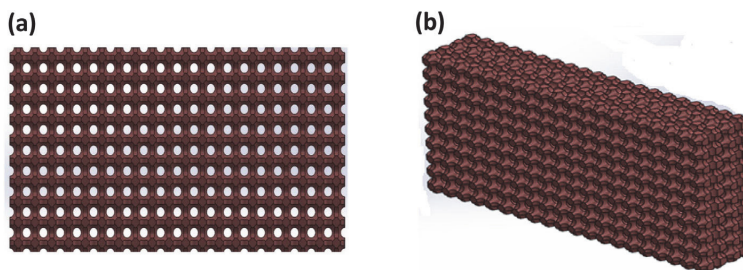


Fig. 4. CAD model of the silicon-wollastonite scaffolds: a) front view; b) isometric view. (For interpretation of the references to colour in this figure legend, the reader is referred to the Web version of this article.)

Table 3
Process parameters and structural features of the scaffolds.

Samples	Laser power (W)	Energy density (J/mm ³)	Characteristic features of the structures
S1	50	416	A lot of cracks
S2	45	375	Considerable amount of cracks
S3	40	333	Decreased pore size
S4	35	291	Decreased pore size
S5	32	266	Designed pore size and a low number of cracks
S6	30	250	Designed pore size with proper structural integrity
S7	25	208	Brittle
S8	22	183	Brittle
S9	20	167	Non-sintered

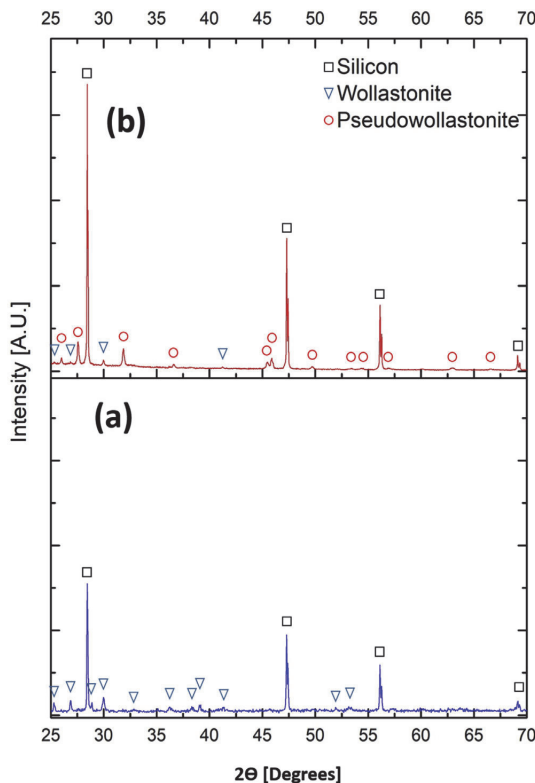


Fig. 5. XRD pattern of a) feedstock powder; b) Si-wollastonite scaffold obtained at 30 W.

based on ICSD 00-027-1402, ICSD 04-016-5334 and ICSD 04-012-1776 reference patterns. It is obvious that melting of the powder in the exposure of the laser has led to increase in the intensity of the peaks for silicon and wollastonite meaning the increasing of the crystallinity of the structure after SLM process. Additionally, pseudowollastonite phase is also observed after the SLM process, which can be attributed to the fact of transition of wollastonite 2M phase to pseudowollastonite (α -wollastonite) at the temperature above 1150 °C due to the laser interaction [37].

Fig. 6 (a,b) shows the SEM images of as-fabricated scaffold and Fig. 6 (g,h) the μ -CT images of the scaffolds which are well complemented to the CAD model in Fig. 4 (a,b). It is worthy to emphasize that no organic binder materials are used to synthesize porous structure

eradicating completely the problem of volumetric shrinkage in the product. In Refs. [38,39] a complex 3D ceramics architecture was found to be far unfeasible due to shrinkage and under-sintered parts, which can be attributed to a lack of binder material, some geometric limitations, and a complicated technology. On the contrary, the scaffolds produced in this work keep the CAD designed shape and size, Fig. 6 (a,g,h).

Additionally, a flaky-like surface morphology around the pores is observed on the as-fabricated scaffolds, Fig. 6b, due to significant thermal accumulation occurred in the molten pool induced by the laser.

The rough surfaces of the scaffolds exhibit a better bone healing response as compared to the smooth surfaces due to enhanced osteoblast differentiation [40]. Therefore, the rough flaky-like surface morphology would be conducive to bone cell adhesion and migration as well as an improved osteogenesis. Fig. 6d depicts the EDS analysis of the product with silicon in pink background and calcium in green background. From the analysis, it is evident that silicon from the precursor powder makes the matrix containing well-dispersed calcium from wollastonite.

The residual porosity observed in Fig. 6 (e,f) should not be seen as an issue (micropores size is of 15–40 μ m) but instead is favourable for cell adherence and penetration of body fluids. The development of the hierarchical porosity (designed macro-porosity coupled with micropores around the macro-pores) can contribute to a higher bone-inducing protein adsorption and bone-like apatite formation by dissolution and re-precipitation. Furthermore, recent studies have indicated that multi-scale porous scaffolds involving both micro- and macro-porosity have advantages over only macro-porous structures. Moreover, the presence of residual pores provides an appropriate surface area for the osteoblast adhesion and proliferation, and is expected to successfully serve for active bonding with the bone tissue [38].

3.4. Porosity and mechanical properties

Skeletal bone structure is characterized by open-cellular porous structure, where the bone stiffness depends not only on the intrinsic modulus of elasticity, but also on the porosity or pore size. The actual porosity of the scaffold evaluated by mercury intrusion porosimetry is of 35%. The bulk and apparent (skeletal) density of the scaffold is 1.4 g/cm³ and 1.8 g/cm³, respectively. The laser machined titanium scaffolds with porosity of 35% and pore size of 250 μ m have already been used in femoral defects in rabbits [35].

One of a drawback in using the bioceramic scaffolds is their low mechanical strength limiting their application in the load-bearing situations. One of the distinctive characteristics of the prepared scaffolds is their relatively high mechanical strength allowing for load bearing applications. Compression tests were stopped at the start of structure brittle failure, corresponding to the maximum compression strength. The measured compressive strength was determined to be linear till 110 MPa with a compressive strain of 6.4% at breakage followed by non-linear behaviour (saw-tooth) as depicted in Fig. 7a. Modulus of elasticity was found to be of around 2.9 GPa which is in vicinity to most of the metallic scaffolds for load bearing applications [10]. The compressive strength of the wollastonite is 14.9 MPa [39]. The compressive strength of the composite bioceramic-based scaffolds might have been increased because of incorporating wollastonite with a needle-like morphology.

The CAD modelled scaffold was considered to have the designed porosity, Fig. 7b. The porous scaffold was fixed on the surface as illustrated in Fig. 7c, while the load was applied from the top to maintain the uniformity with the experimental stress strain measurements. The boundary conditions shown in the arrows illustrates the direction of the constant deformation (0.5 mm/min) in Fig. 7c. The scaffold was continuously deformed in subsequent twenty-five sub steps until the compact structure was obtained in Fig. 7d. The stress was homogeneously disturbed onto the porous scaffold starting from the range of

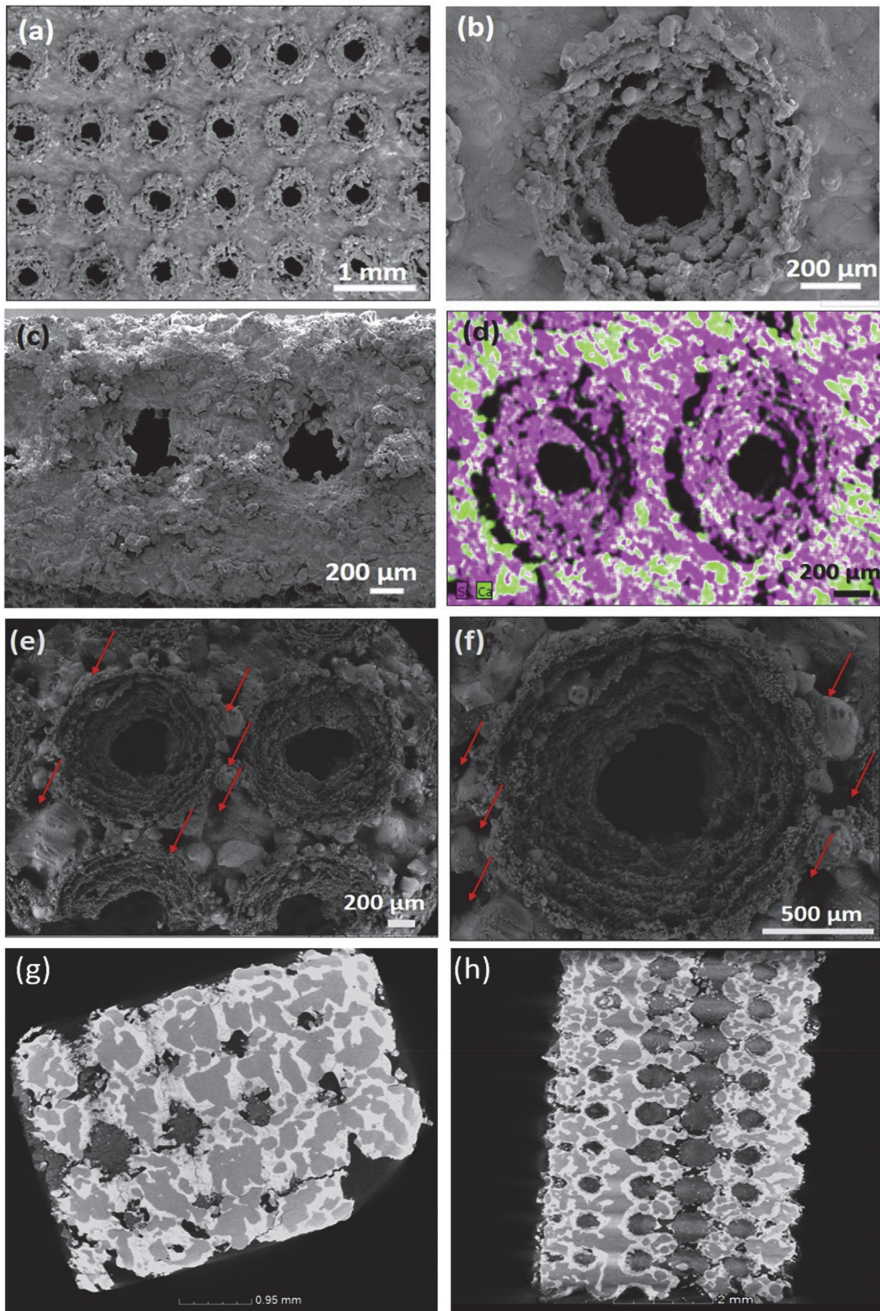


Fig. 6. a) SEM micrograph of the scaffolds as-obtained by SLM with pore size of 400 μm ; b) detailed pore morphology; c) cross-sectional details of the scaffold with interconnected pore; d) EDS element mapping of the scaffold with silicon in pink and calcium in green color; e) and f) show the residual porosity around the pores of the scaffolds indicated by red arrows; g) and h) $\mu\text{-CT}$ images of the front and cross section details of the scaffolds. (For interpretation of the references to colour in this figure legend, the reader is referred to the Web version of this article.)

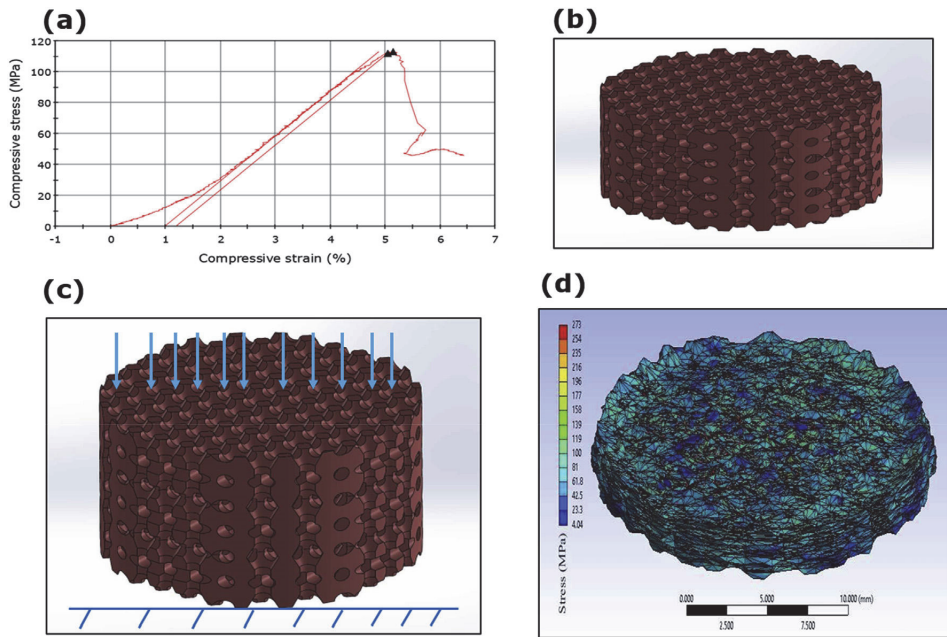


Fig. 7. a) Compressive stress-strain response of the as-produced scaffolds; b) CAD design of Si-wollastonite scaffold; c) Finite element simulation analysis of the porous composite scaffolds and the boundary conditions; d) Normal stress plot under compressive deformation.

68 MPa–273 MPa. Red dots depicted in Fig. 7d represent the separated particles after the compression test indicating that a local stress has even reached up to 293 MPa. Full analysis video documented in the Supplementary material S1 illustrates that FE models (ANSYS software) accounts for the increased volume fraction and thus proves the aptness of FE models to compute scaffold compressive strength prior to in-vivo experiments [41].

Supplementary video related to this article can be found at <https://doi.org/10.1016/j.ceramint.2019.08.208>

Additionally, the analysis of the compressive strength (strength decay) of the scaffolds was performed on the samples immersed into Tris for 3, 7 and 14 days with the results listed in Fig. 8. The mechanical strength of the scaffolds decreased down to 90 MPa when immersed for two weeks. Additionally, it can be also observed in the microstructure

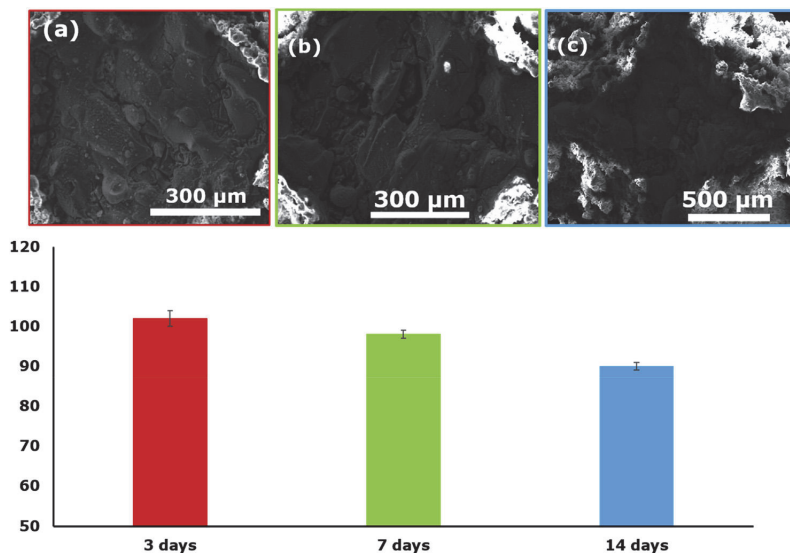


Fig. 8. Represents the bar graph of the compressive strength of the scaffolds after immersing in Tris buffer solution with the successive days and corresponding colour boundaries with the microstructure. (For interpretation of the references to colour in this figure legend, the reader is referred to the Web version of this article.)

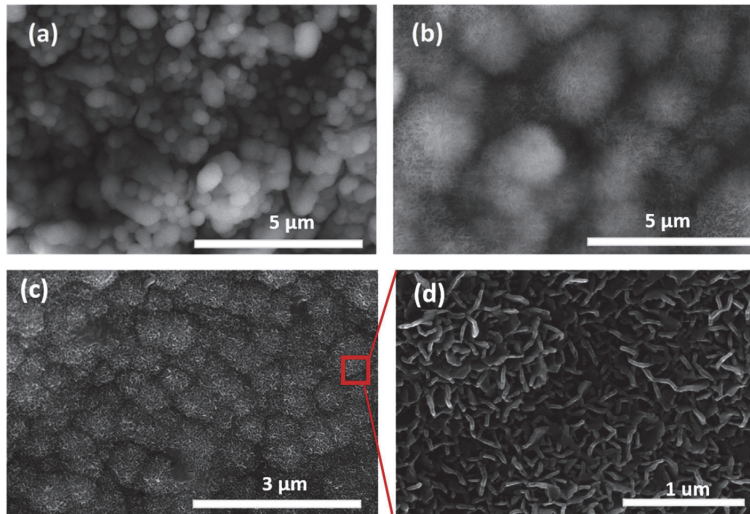


Fig. 9. Scanning electron microscopy (SEM) pictures of hydroxyapatite grown onto the scaffolds immersed in the SBF solution for (a) 3; (b) 7; (c) 14; (d) magnified hydroxyapatite granules from Fig. 8c.

that attack by the Tris buffer is clearly visible. The rugged surface of the scaffolds is clearly visible in Fig. 9 (a,b,c) which leads to the decrease in the strength of the scaffolds as compared to as-produced scaffolds in Fig. 12a.

3.5. Bioactivity

In vitro incubation in SBF solution is performed to access the ability of the composite scaffolds for the nucleation and controlled growth of the hydroxyapatite-like bioceramics. The specimens were immersed in SBF solution and placed in a culture oven at 37 °C for 3, 7 and 14 days; then the analysis of the chemical composition of the surface and its morphology were carried out. The microstructural features of the scaffolds after different time of immersion are shown in Fig. 9(a–d).

Hydroxyapatite (HA) crystals are well recognized by their globular shape as illustrated in Fig. 9a. Increase in a soaking time results in the development of a large surface area of the bioactive substrate to be exposed to SBF, and therefore, may be considered as a foam-like morphology, Fig. 9b. After 14 days of the test, the typical “cauliflower” morphologies of HA formed on a scaffold were developed as illustrated in Fig. 9(c,d). The apatite-like granules were observed around the pores produced by dissolution and re-precipitation mechanism and thus facilitates the strong bonding of the bioceramics scaffold and the host bone tissue [42].

Mechanism of deposition of HA granules can be explained based on the supersaturated solution of SBF. A supersaturated solution of ions provides nucleation sites to form HA layer onto the scaffolds. This nucleation is delivered by the silanol ions (Si–OH), which overcome the activation energy and give nucleus for the HA precipitation [43]. The dissolution of ions on the bioceramic surface locally increases their concentration leading to the heterogeneous precipitation of the biological apatite.

The hydroxyapatite profile is used as a standard for comparing the deposition of the HA onto the scaffold in Fig. 10. The vibrational bands at 432 cm^{-1} and 587 cm^{-1} are attributed to the O–P–O bending modes [44]. The internal modes of the PO_4^{3-} tetrahedral frequency 960 cm^{-1} corresponds to the symmetric stretching of P–O bonds. The three high intensities vibrational bands, as seen at the standard HA profile, are also profoundly found. An intensive sharp peak at $\sim 520 \text{ cm}^{-1}$ is attributed to the crystalline silicon presented in the material of scaffold.

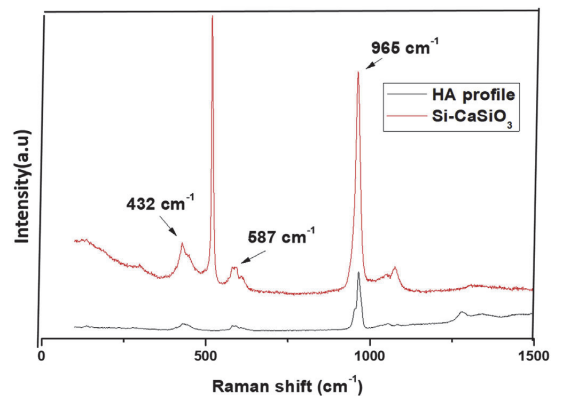


Fig. 10. Shows the RAMAN spectrum of the scaffolds immersed in the SBF solution for 3 days.

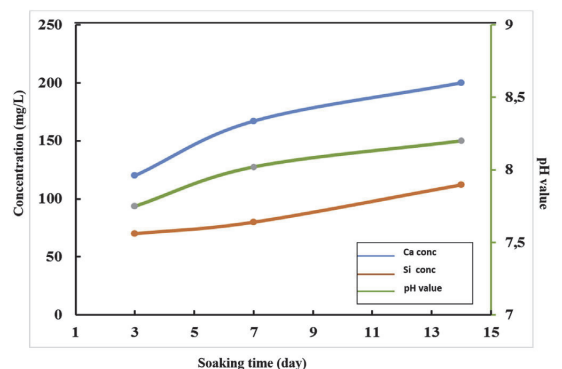


Fig. 11. Concentration of Ca and Si ions as a function of soaking time in Tris buffer solution and corresponding pH values.

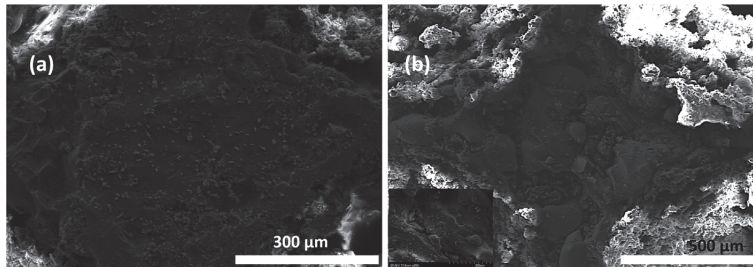


Fig. 12. a) The scaffold before immersion in Tris-HCl; b) scaffold after immersion in Tris-HCl on the 14th day.

3.6. Biodegradation of Si-wollastonite scaffolds

Fig. 11 shows the amounts of Si and Ca ions lixiviated to the solution and pH values in Tris solution after soaking scaffolds for different periods. A gradual increase in the concentration of Ca and Si ions released from scaffold material is observed as a function of the soaking time. Tris does not contain silicon ions and the concentration of silicon species in Tris increased to 70 mg/L during the first 3 days and to 112 mg/L after 14 days. With time, the scaffolds lost their weight from 5.5% of its original weight during 3 days followed by 6.6% and 7.9% lost on the 7th and 14th day, respectively.

On the other hand, the pH values of the scaffold-soaked Tris solution slowly increased with the soaking time probably due to the chelation effect of silicate group (SiO_4^{4-}) with H^+ during material dissolution. It has been reported that a weak alkaline microenvironment could enhance osteoblast viability and proliferation [45]. Thus, the limited increase in pH value is thought to be favourable for osteogenic cell growth in the porous constructs.

The microstructure of the scaffolds are analyzed to investigate the effect of dissolution onto the surface of the scaffolds. The changes in the microstructure of the scaffolds on the 3rd and 7th day is not that substantial as compared to the 14th day. Fig. 12b shows the surface of the scaffolds designating the dissolution mechanism that leads to the formation of the rugged surface after immersion of the scaffolds on the 14th day. The dissolution have been preferably taken on the specific crystallographic planes leaving behind the ripples or rugged surface, which have been attacked [46]. EDS analysis of area depicted in Fig. 12a with the ratio of Ca/Si was 1.60 and after the dissolution on the 14th day was 0.65.

4. Discussion

It is worth to mention that a complex 3D bioceramics architecture was found to be far unfeasible due to shrinkage and under-sintered parts, which are inevitable outcomes in the porous constructs and can be attributed to a lack of binder material, geometric limitations and a complicated technology. Herein, we propose a novel strategy in order to fulfil these loopholes by choosing a novel feedstock for the SLM process. The novel feedstock allows to directly print the scaffolds which comprises of silicon (osteoinductive) and wollastonite (bioactive) elements without involving binders and post-processing stages, which are generally expensive and time-consuming.

The SLM parameters optimization was done based on the energy density parameter. Laser current was modulated from 20W to 50W keeping the point distance of 10 μm and exposure time of 125 μs was constant for all the scaffolds. The pore size and porosity plays a crucial role in bone tissue engineering both in vitro and in vivo. The large pore size (macro-porosity) designed to be 400 μm is relevant to the enhanced osteogenesis since it favours angiogenesis and higher oxygenation of the osteoblasts. Additionally, the residual pores (micro-porosity) can be attributed to the powder morphology of the feedstock and mismatch of

the thermal expansion coefficients of silicon and wollastonite in the composite. These residual pores can enhance the transport of the nutrients, oxygen to the tissues, removal of metabolic wastes of the cells and infiltration of the simulating body fluid.

The compressive strength of the as-produced scaffolds is 110 MPa, which is much higher as compared to the compressive strength of the cancellous bone (1.5–7 MPa) and a little lower as compared to the cortical bone (120–150 MPa) [14,15,24,26,27]. The non-linear zone of the stress-strain curve (saw-tooth nature) in Fig. 7a is attributed to the non-linear stress distribution onto the scaffold and reaching the ultimate stress by some volume elements, which undergoes failure with a compressive strain of 6.4%. The finite element simulation analysis suggests that the red dots and the contours represent local stress up to 273 MPa (Fig. 7d), while the regions indicated in blue and light blue shows the stress of 101 MPa henceforth indicating that the compressive strength obtained from the finite element analysis well corroborated with the experimentally recorded values.

5. Conclusions

In this study, Si-wollastonite scaffolds were obtained by selective laser melting (SLM) with no addition of any binder material and without geometric constraints. For this purpose a novel powders feedstock was designed. The following are the key observations:

1. A novel powder feedstock for SLM, which comprises of silicon (osteoinductive) and wollastonite (bioactive) elements, was developed for fabrication of bio-active ceramic-based scaffolds.
2. Energy density was used to optimize the process of scaffolds fabrication. Applying a high energy density up to 416 J/mm^3 results in the development of cracked/defected scaffolds. On the contrary, a low energy density of 167 J/mm^3 leads to the un-sintered and brittle constructs. The energy density of 250 J/mm^3 was selected as an optimal one for the fabrication of silicon-wollastonite scaffolds with pre-designed spherical pore size of 400 μm in diameter.
3. The constructs exhibit the porosity of 35%, the compressive strength of 110 MPa and modulus of elasticity of 2.9 GPa, which are acceptable parameters for bone tissue engineering. The finite element simulation results of the compressive strength of the scaffolds are in a good agreement with the experimental values showing a local stress reaching up to 293 MPa.
4. The compressive strength decreases from 110 MPa down to 90 MPa after immersion of the scaffolds into Tris solution for 14 days.
5. The pore size, enhanced bioactivity and compressive strength of 110 MPa elucidated in this study for the scaffolds demonstrate the potential use of Si-wollastonite scaffolds fabricated using the SLM process in bone repair applications, especially for replacement of the bone defects by designing and producing scaffolds with a similar internal architecture or with required changes in the pore morphology.

In our previous study, we demonstrated that as-produced silicon-wollastonite scaffolds with a pre-defined pore structure can also be used as drug delivery vehicles with sustained delivery of antibiotic vancomycin [47], with sudden burst of the antibiotic release (almost 40%) in the first 40 h followed by sustain release of the almost next 30% of the antibiotic in the passage of 160 h. Henceforth, combining the ability of the additively manufactured novel scaffolds with the appropriate mechanical properties can extend applications of the developed structures not only in bone tissue engineering but also for in-situ thin-wall skull (maxillofacial) and dental applications.

Acknowledgements

This work was supported by the personal grant of the Estonian Research Council (PUT1063, I. Hussainova), and the Estonian Ministry of Higher Education and Research under Projects IUT19-29, Estonia; the European Regional Fund, project number 2014-2020.4.01.16-0183 (Smart Industry Centre) and Kristjan Jaak scholarship for short term study visit to ICV, Madrid, Spain. The authors would like to acknowledge the help of PhD Mart Viljus from Department of Mechanical and Industrial Engineering, TUT for SEM imaging.

References

- [1] G. Turnbull, J. Clarke, F. Picard, P. Riches, L. Jia, F. Han, B. Li, W. Shu, 3D bioactive composite scaffolds for bone tissue engineering, *Bioact. Mater.* (2018), <https://doi.org/10.1016/j.bioactmat.2017.10.001>.
- [2] B. Tandon, J.J. Blaker, S.H. Cartmel, Piezoelectric materials as stimulatory biomedical materials and scaffolds for bone repair, *Acta Biomater.* (2018), <https://doi.org/10.1016/j.actbio.2018.04.026>.
- [3] J. Jacob, N. More, K. Kalita, G. Kapuseti, Piezoelectric smart biomaterials for bone and cartilage tissue engineering, *Inflamm. Regen.* (2018), <https://doi.org/10.1186/s41232-018-0059-8>.
- [4] J. Henkel, M.A. Woodruff, D.R. Epari, R. Steck, V. Glatt, I.C. Dickinson, P.F.M. Choong, M.A. Schuetz, D.W. Hutmacher, Bone regeneration based on tissue engineering conceptions — a 21st century perspective, *Bone Res* (2014), <https://doi.org/10.4248/br201303002>.
- [5] S.M. Damaraju, Y. Shen, E. Elele, B. Khuisid, A. Eshghinejad, J. Li, M. Jaffe, T.L. Arinzech, Three-dimensional Piezoelectric Fibrous Scaffolds Selectively Promote Mesenchymal Stem Cell Differentiation, *Biomaterials*, 2017, <https://doi.org/10.1016/j.biomaterials.2017.09.024>.
- [6] G. Li, L. Wang, W. Pan, F. Yang, W. Jiang, X. Wu, X. Kong, K. Dai, Y. Hao, In vitro and in vivo study of additive manufactured porous Ti6Al4V scaffolds for repairing bone defects, *Sci. Rep.* (2016), <https://doi.org/10.1038/srep34072>.
- [7] J.Y. Rho, L. Kuhn-Spearing, P. Zioupos, Mechanical properties and the hierarchical structure of bone, *Med. Eng. Phys.* (1998), [https://doi.org/10.1016/S1350-4533\(98\)00007-1](https://doi.org/10.1016/S1350-4533(98)00007-1).
- [8] P.S. EGGLE, W. MOLLER, R.K. SCHENK, Porous hydroxyapatite and tricalcium phosphate cylinders with two different pore size ranges implanted in the cancellous bone of rabbits, *Clin. Orthop. Relat. Res.* (2006), <https://doi.org/10.1097/00003086-198807000-00017>.
- [9] S. Kunjalukkal Padmanabhan, F. Gervaso, M. Carrozzo, F. Scalera, A. Sannino, A. Licciulli, Wollastonite/hydroxyapatite scaffolds with improved mechanical, bioactive and biodegradable properties for bone tissue engineering, *Ceram. Int.* (2013), <https://doi.org/10.1016/j.ceramint.2012.06.073>.
- [10] X.P. Tan, Y.J. Tan, C.S.L. Chow, S.B. Tor, W.Y. Yeong, Metallic powder-bed based 3D printing of cellular scaffolds for orthopaedic implants: a state-of-the-art review on manufacturing, topological design, mechanical properties and biocompatibility, *Mater. Sci. Eng. C* (2017), <https://doi.org/10.1016/j.msec.2017.02.094>.
- [11] B. Thavornnyutikarn, N. Chantarampanich, K. Sithiseripratip, G.A. Thouas, Q. Chen, Bone tissue engineering scaffolding: computer-aided scaffolding techniques, *Prog. Biomater.* (2014), <https://doi.org/10.1007/s40204-014-0026-7>.
- [12] C. Deng, H. Zhu, J. Li, C. Feng, Q. Yao, L. Wang, J. Chang, C. Wu, Bioactive scaffolds for regeneration of cartilage and subchondral bone interface, *Theranostics* (2018), <https://doi.org/10.7150/thno.23674>.
- [13] C. Gao, Y. Deng, P. Feng, Z. Mao, P. Li, B. Yang, J. Deng, Y. Cao, C. Shuai, S. Peng, Current progress in bioactive ceramic scaffolds for bone repair and regeneration, *Int. J. Mol. Sci.* (2014), <https://doi.org/10.3390/ijms15034714>.
- [14] J.K. Carrow, A. Di Luca, A. Dolatshahi-Pirouz, L. Moroni, A.K. Gaharwar, 3D-printed bioactive scaffolds from nanosilicates and PEOT/PBT for bone tissue engineering, *Regen. Biomater.* (2018), <https://doi.org/10.1093/rb/rby024>.
- [15] Q. Lv, L. Nair, C.T. Laurencin, Fabrication, characterization, and in vitro evaluation of poly(lactic acid glycolic acid)/nano-hydroxyapatite composite microspheres-based scaffolds for bone tissue engineering in rotating bioreactors, *J. Biomed. Mater. Res. A* (2009), <https://doi.org/10.1002/jbm.a.32302>.
- [16] T.M.G. Chu, D.G. Orton, S.J. Hollister, S.E. Feinberg, J.W. Halloran, Mechanical and in Vivo Performance of Hydroxyapatite Implants with Controlled Architectures, *Biomaterials*, 2002, [https://doi.org/10.1016/S0142-9612\(01\)00243-5](https://doi.org/10.1016/S0142-9612(01)00243-5).
- [17] P. Miranda, A. Pajares, E. Saiz, A.P. Tomsia, F. Guiberteau, Mechanical properties of calcium phosphate scaffolds fabricated by robocasting, *J. Biomed. Mater. Res. A* (2008), <https://doi.org/10.1002/jbm.a.31587>.
- [18] S. Pramanik, A.K. Agarwal, K.N. Rai, A. Garg, Development of high strength hydroxyapatite by solid-state-sintering process, *Ceram. Int.* (2007), <https://doi.org/10.1016/j.ceramint.2005.10.025>.
- [19] Q. Fu, E. Saiz, A.P. Tomsia, Bioinspired strong and highly porous glass scaffolds, *Adv. Funct. Mater.* (2011), <https://doi.org/10.1002/adfm.201002030>.
- [20] N.D. Doiphode, T. Huang, M.C. Leu, M.N. Rahaman, D.E. Day, Freeze extrusion fabrication of 13-93 bioactive glass scaffolds for bone repair, *J. Mater. Sci. Mater. Med.* (2011), <https://doi.org/10.1007/s10856-011-4236-4>.
- [21] K.C.R. Kolan, M.C. Leu, G.E. Hilmans, R.F. Brown, M. Velez, Fabrication of 13-93 bioactive glass scaffolds for bone tissue engineering using indirect selective laser sintering, *Biofabrication* (2011), <https://doi.org/10.1088/1758-5082/3/2/025004>.
- [22] C. Wu, Y. Luo, G. Cuniberti, Y. Xiao, M. Gelinsky, Three-dimensional printing of hierarchical and a tight mesoporous bioactive glass scaffolds with a controllable pore architecture, excellent mechanical strength and mineralization ability, *Acta Biomater.* (2011), <https://doi.org/10.1016/j.actbio.2011.03.009>.
- [23] F.J. Martínez-Vázquez, M.V. Cabañas, J.L. Paris, D. Lozano, M. Vallet-Regí, Fabrication of novel Si-doped hydroxyapatite/gelatin scaffolds by rapid prototyping for drug delivery and bone regeneration, *Acta Biomater.* (2015), <https://doi.org/10.1016/j.actbio.2014.12.021>.
- [24] H. Elsayed, M. Sinico, M. Secco, F. Zorzi, P. Colombo, E. Bernardo, B-doped hard-ystonite bioceramics from preceramic polymers and fillers: synthesis and application to foams and 3D-printed scaffolds, *J. Eur. Ceram. Soc.* (2017), <https://doi.org/10.1016/j.jeurceramsoc.2016.12.002>.
- [25] D. Ke, S. Bose, Doped tricalcium phosphate bone tissue engineering scaffolds using sucrose as template and microwave sintering: enhancement of mechanical and biological properties, *Mater. Sci. Eng. C* (2017), <https://doi.org/10.1016/j.msec.2017.03.167>.
- [26] M. Sun, A. Liu, H. Shao, X. Yang, C. Ma, S. Yan, Y. Liu, Y. He, Z. Gou, Systematic evaluation of mechanically strong 3D printed diluted magnesium doping wollastonite scaffolds on osteogenic capacity in rabbit calvarial defects, *Sci. Rep.* (2016), <https://doi.org/10.1038/srep34029>.
- [27] W. Zhao, J. Wang, W. Zhai, Z. Wang, J. Chang, The Self-Setting Properties and in Vitro Bioactivity of Tricalcium Silicate, *Biomaterials*, 2005, <https://doi.org/10.1016/j.biomaterials.2005.04.025>.
- [28] S. Xu, K. Lin, Z. Wang, J. Chang, L. Wang, J. Lu, C. Ning, Reconstruction of Calvarial Defect of Rabbits Using Porous Calcium Silicate Bioactive Ceramics, *Biomaterials*, 2008, <https://doi.org/10.1016/j.biomaterials.2008.03.013>.
- [29] R. Murugan, S. Ramakrishna, Nano-Featured Scaffolds for Tissue Engineering: A Review of Spinning Methodologies, *Tissue Eng.* (2006), <https://doi.org/10.1089/ten.2006.12.435>.
- [30] S.J. Kalita, S. Bose, H.L. Hosick, A. Bandyopadhyay, Development of controlled porosity polymer-ceramic composite scaffolds via fused deposition modeling, *Mater. Sci. Eng. C* (2003), [https://doi.org/10.1016/S0928-4931\(03\)00052-3](https://doi.org/10.1016/S0928-4931(03)00052-3).
- [31] J.A. Puértolas, J.L. Vadillo, S. Sánchez-Salcedo, A. Nieto, E. Gómez-Barrena, M. Vallet-Regí, Compression behaviour of biphasic calcium phosphate and biphasic calcium phosphate-agarose scaffolds for bone regeneration, *Acta Biomater.* (2011), <https://doi.org/10.1016/j.actbio.2010.07.032>.
- [32] T. Minasyan, L. Liu, Y. Holovenko, S. Aydinian, I. Hussainova, Additively manufactured mesostructured MoSi₂-Si₃N₄ ceramic lattice, *Ceram. Int.* (2019), <https://doi.org/10.1016/j.ceramint.2019.02.035>.
- [33] X. Li, D. Li, B. Lu, C. Wang, Fabrication of bioceramic scaffolds with pre-designed internal architecture by gel casting and indirect stereolithography techniques, *J. Porous Mater.* (2008), <https://doi.org/10.1007/s10934-007-9148-9>.
- [34] N.S. Nikonova, I.N. Tikhomirova, A.V. Belyakov, A.I. Zakharov, Wollastonite in silicate matrices, *Glas. Ceram. (English Transl. Steklo i Keramika)* (2003), <https://doi.org/10.1023/B:GLAC.0000008241.84600.f9>.
- [35] V. Karageorgiou, D. Kaplan, Porosity of 3D Biomaterial Scaffolds and Osteogenesis, *Biomaterials*, 2005, <https://doi.org/10.1016/j.biomaterials.2005.02.002>.
- [36] D. Gu, H. Wang, D. Dai, P. Yuan, W. Meiners, R. Poprawe, Rapid fabrication of Al-based bulk-form nanocomposites with novel reinforcement and enhanced performance by selective laser melting, *Ser. Mater.* (2015), <https://doi.org/10.1016/j.scriptamat.2014.10.011>.
- [37] X. Wan, A. Hu, M. Li, C. Chang, D. Mao, Performances of CaSiO₃ ceramic sintered by Spark plasma sintering, *Mater. Char.* (2008), <https://doi.org/10.1016/j.matchar.2007.01.002>.
- [38] J.J. Blaker, J.E. Gough, V. Maquet, I. Notingher, A.R. Boccaccini, In vitro evaluation of novel bioactive composites based on Bioglass®-filled polylactide foams for bone tissue engineering scaffolds, *J. Biomed. Mater. Res. A* (2003), <https://doi.org/10.1002/jbm.a.20055>.
- [39] H. Ma, T. Li, Z. Huan, M. Zhang, Z. Yang, J. Wang, J. Chang, C. Wu, 3D printing of high-strength bioscaffolds for the synergistic treatment of bone cancer, *NPG Asia Mater.* (2018), <https://doi.org/10.1038/s41427-018-0015-8>.
- [40] K. Anselme, Osteoblast Adhesion on Biomaterials, *Biomaterials*, 2000.
- [41] J.M. Williams, A. Adewunmi, R.M. Schek, C.L. Flanagan, P.H. Krebsbach, S.E. Feinberg, S.J. Hollister, S. Das, Bone Tissue Engineering Using Polycaprolactone Scaffolds Fabricated via Selective Laser Sintering, *Biomaterials*, 2005, <https://doi.org/10.1016/j.biomaterials.2004.11.057>.
- [42] F. Baino, J. Minguella, N. Kirk, M.A. Montealegre, C. Fiaschi, F. Korkusuz, G. Orlygsson, V.B. Chiara, Novel full-ceramic monoblock acetabular cup with a bioactive trabecular coating: design, fabrication and characterization, *Ceram. Int.* (2016), <https://doi.org/10.1016/j.ceramint.2016.01.065>.
- [43] S. Jiang, W. Jin, Y.N. Wang, H. Pan, Z. Sun, R. Tang, Effect of the aggregation state of amorphous calcium phosphate on hydroxyapatite nucleation kinetics, *RSC Adv.*

- (2017), <https://doi.org/10.1039/c7ra02208e>.
- [44] J.C. Elliott, Structure and chemistry of the apatites and other calcium orthophosphates, <https://doi.org/10.1016/B978-0-444-81582-8.50001-8>, (1994).
- [45] Y. Shen, W. Liu, C. Wen, H. Pan, T. Wang, B.W. Darvell, W.W. Lu, W. Huang, Bone regeneration: importance of local pH - strontium-doped borosilicate scaffold, *J. Mater. Chem.* (2012), <https://doi.org/10.1039/c2jm16141a>.
- [46] H.Y. Yang, I. Thompson, S.F. Yang, X.P. Chi, J.R.G. Evans, R.J. Cook, Dissolution characteristics of extrusion freeformed hydroxyapatite-tricalcium phosphate scaffolds, *J. Mater. Sci. Mater. Med.* (2008), <https://doi.org/10.1007/s10856-008-3473-7>.
- [47] N. Kamboj, M.A. Rodríguez, R. Rahmani, K.G. Prashanth, I. Hussainova, Bioceramic scaffolds by additive manufacturing for controlled delivery of the antibiotic vancomycin, *Proc. Est. Acad. Sci.* (2019), <https://doi.org/10.3176/proc.2019.2.10>.

Paper II

Nikhil Kamboj, Rodríguez, M.A., Rahmani, R., Prashanth, K.G., and Hussainova, I., 2019. Bioceramic scaffolds by additive manufacturing for controlled delivery of the antibiotic vancomycin. *Proceedings of the Estonian Academy of Sciences*, 68(1), 185–190, doi.org/10.3176/proc.2019.2.10.

Reproduced with the permission of Estonian Academy of Sciences.



Bioceramic scaffolds by additive manufacturing for controlled delivery of the antibiotic vancomycin

Nikhil Kamboj^{a*}, Miguel A. Rodríguez^b, Ramin Rahmani^a, Konda Gokuldoss Prashanth^a, and Irina Hussainova^a

^a Department of Mechanical and Industrial Engineering, Tallinn University of Technology, Ehitajate tee 5, 19086 Tallinn, Estonia

^b Instituto de Ceramica y Vidrio (ICV-CSIC), C/Kelsen 5, 28049 Madrid, Spain

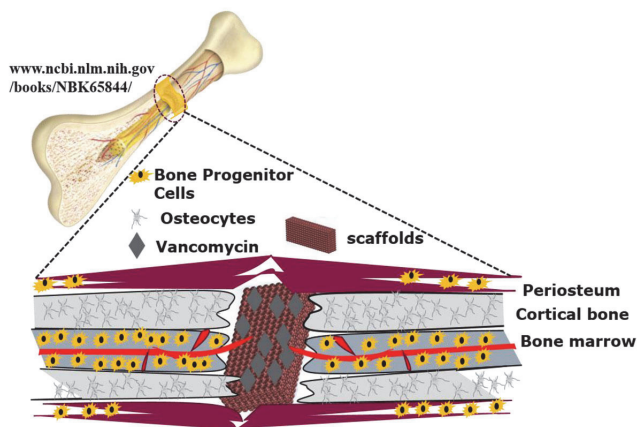
Received 20 December 2018, accepted 12 March 2019, available online 22 April 2019

© 2019 Authors. This is an Open Access article distributed under the terms and conditions of the Creative Commons Attribution-NonCommercial 4.0 International License (<http://creativecommons.org/licenses/by-nc/4.0/>).

Abstract. Silicon–calcium silicate scaffolds were fabricated by selective laser melting (SLM). Rectangular composite scaffolds with a pore size of 400 μm were designed with dimensions of $10 \times 20 \times 5 \text{ mm}^3$. For imparting controlled drug release capability, scaffolds were covered with polycaprolactone (PCL) coatings for the sustained delivery of vancomycin. The drug release profile of the coated scaffolds was studied by UV–visible spectroscopy. The encapsulated drug within the PCL coated scaffold exhibited a controlled release of vancomycin. Nearly 50% of the vancomycin release from the scaffolds was observed during the first 40 h followed by the sustained release of vancomycin of nearly 20% of the actual loaded drug for the next six days. These findings suggest that SLM synthesized scaffolds with PCL coating can expand their applicability to be used as a target for *Staphylococci aureus* bacteria, which often cause chronic infections such as chronic osteomyelitis in bone.

Key words: selective laser melting, 3D printing, bioceramic scaffolds, drug delivery.

Graphical abstract



Si-CaSiO₃ scaffolds for drug delivery and bone repair

* Corresponding author, nikhil.kamboj@taltech.ee

1. INTRODUCTION

Vancomycin is a peptide drug needed for the treatment of serious, life-threatening infections by Gram-positive bacteria, particularly for the treatment of chronic osteomyelitis [1]. ‘Small colony variants’, a subpopulation of *Staphylococci aureus*, have been described as emerging pathogens and as another mechanism by which *S. aureus* can evade the immune response and antimicrobial therapy [2]. These bacteria often cause antibiotic-refractory recurrent and chronic infections such as chronic osteomyelitis [3].

Various studies have suggested that the local application of antimicrobials clearly provides higher local antibiotic concentrations than those achieved with intravenous application [4,5]. The most frequently studied material is polymethylmethacrylate (PMMA) serving as a carrier for the local delivery of antibiotics [6]. However, PMMA beads are associated with some drawbacks including an antibiotic delivery, as the carrier material is not degradable, and induction of foreign body reaction of the immune system [7]. The emerging 3D printing technologies, 3D scaffolds, are nowadays used as carriers for a better and controllable local delivery of antibiotics.

The composite scaffolds manufactured by 3D printing are used for drug loading to study the sustained release properties for bone tissue engineering [8]. Du et al. [9] recently printed macro/meso-porous composite scaffolds, which are loaded with high dosages of isoniazid/rifampin against anti-osteoarticular tuberculosis. These scaffolds show a greatly prolonged drug release time as compared to the commercial calcium phosphate scaffolds both in vitro and in vivo, with the combined merits of osseous regeneration and local multi-drug therapy. In the study by Zhang et al. [10] magnetic Fe₃O₄ nanoparticles incorporated onto mesoporous bioactive glass/polycaprolactone (PCL) composite scaffolds were fabricated by 3D printing. Incorporation of magnetic Fe₃O₄ nanoparticles into bioactive glass/PCL scaffolds not only influenced the apatite mineralization (bioactivity) ability, but also resulted in an excellent magnetic heating ability and significantly stimulated cell proliferation and differentiation. Moreover, when doxorubicin was used as a model anticancer drug, Fe₃O₄/bioactive glass/PCL scaffolds exhibited a sustained drug release for use in local drug delivery therapy. Zhou et al. [11] tested and designed a novel composite scaffold with antibacterial efficacy for treating bone infections using a 3D printed poly(ϵ -caprolactone) (PCL) scaffold coated with polydopamine (PDA) for the adsorption of poly(lactic acid)-glycolic acid (PLGA) microspheres loaded with vancomycin.

The innovative concept of surgical implantation of high osteogenic scaffolds with tailored hierarchical meso-macroporosity followed by local drug delivery could provide a new synergistic strategy for treating bone repair and infection. Herein, we synthesized novel Si–CaSiO₃ composite scaffolds with the single-step technology and without addition of binders by selective laser melting (SLM) for local delivery of vancomycin. The high surface area, large pore volume, and mesoporous structure of Si–CaSiO₃ scaffolds printed by SLM is beneficial for the enhancement of local delivery of vancomycin. At the same time, the 3D printing technique allows controlling the level of porosity of the as-synthesized scaffolds. The aim of the study was to use bioceramic scaffolds synthesized by 3D printing and to investigate the local sustained delivery of vancomycin for treating chronic osteomyelitis infection.

2. EXPERIMENTAL

2.1. Synthesis of the bioceramic scaffolds

The starting powder materials were >99.9% purity wollastonite (CaSiO₃) (Aldrich) with a particle size of 1–5 μ m and >99.5% purity silicon (Silgrain-Elkem) with a mean particle size ranging from 10 to 44 μ m. The powders were mixed in 50/50 wt% in ethanol with 50 rpm for 3 h, and later the powder mixture was kept for drying in a furnace.

The melting of the mixed powder was performed by the SLM technique using a Metal 3D printer (ReaLizer GmbH SLM-50, Germany) equipped with a YAG: Nd³⁺ laser with a maximum output power of 120 W, laser spot size of 15–80 μ m, and computer-controlled laser beam scan velocity of up to 1000 mm/s. The process was performed in a chamber sealed with high-purity argon (99.999 vol%) to avoid oxidation and degradation of the powder.

2.2. Procedures of loading vancomycin onto PCL-coated bioceramic scaffolds

The coating of the as-fabricated bioceramic scaffolds (Si–CaSiO₃) was prepared by dissolving 7.5 wt% of polycaprolactone (PCL) solution in dichloromethane (DMC), both from Sigma Aldrich, for 10 min at 37 °C using a magnetic stirrer. Vancomycin hydrochloride (Fig. 1) with a concentration of 19.2 mg/mL was added to the coating solution and stirred additionally for 5 min. Then, the as-fabricated scaffolds with a weight of 1 gm were dipped into the coating solution for 10 min in vacuum. Under vacuum the coating solution containing

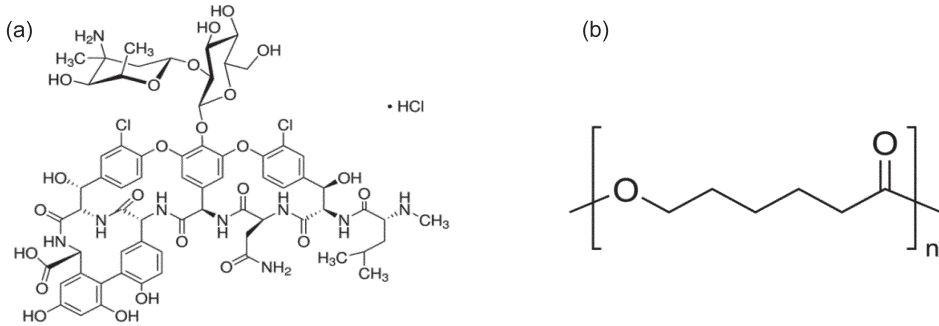


Fig. 1. Vancomycin hydrochloride molecule (a) and PCL molecule (b).

vancomycin promotes the penetration of the vancomycin inside the porous network of the bioceramic scaffolds. In fact, under normal pressure, the surface tension of the liquid prevents the infiltration of vancomycin into the pores of the scaffold. Allowing displacement of the air within the pores of the scaffolds with vancomycin solution by lowering the pressure can enhance the amount of vancomycin adsorbed and/or the rate of its penetration.

The scaffolds were placed in 60 mL vials containing simulating body fluid (SBF) into a shaking incubator at a constant speed of 240 rpm at 37 °C for some days. The vancomycin release measurements were carried out by using UV/vis spectroscopy at a wavelength of 280 nm with the correlation coefficient of $R^2 = 0.9999$ for the calibration curve between the absorbance and vancomycin concentration.

3. RESULTS AND DISCUSSION

3.1. Synthesis of the bioceramic scaffolds by selective laser melting

Figure 2(a) illustrates the as-synthesized bioceramic scaffold (Si–CaSiO₃) printed by SLM, and Fig. 2(b) depicts the microstructure of the scaffolds. Both of the figures show that scaffolds can be fabricated by layer-by-layer melting despite the fact that the ceramics have a low absorption of laser beam energy and poor thermal shock resistance [12].

The macroporosity (pore size $400 \pm 20 \mu\text{m}$) achieved was in accordance with the design of the model. Additionally, mesoporosity (pore size 15–50 μm), indicated by a blue circle on the image presented in Fig. 2(b), is observed and can be attributed to the interconnectivity of the macropores for the infiltration of SBF.

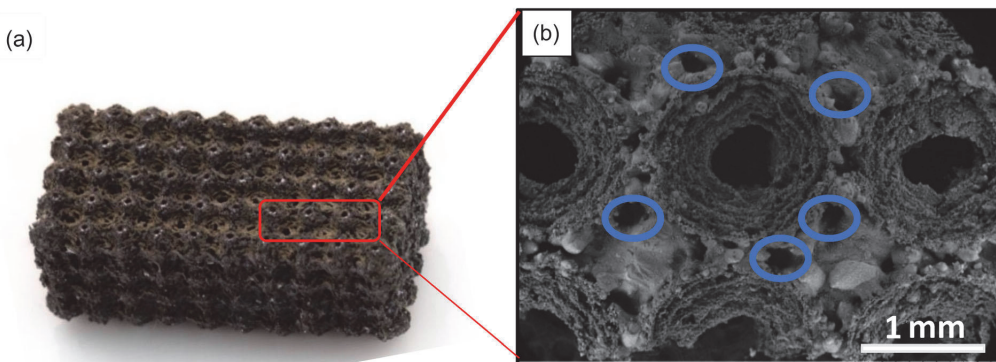


Fig. 2. As-synthesized Si–CaSiO₃ scaffolds printed by selective laser melting (a) and the microstructure of the scaffolds with macropores ($\sim 400 \mu\text{m}$) and mesopores (blue circles, pore size $\sim 15\text{--}50 \mu\text{m}$) (b).

The capability of 3D printing techniques of producing scaffolds with structural anisotropy is well documented [13]. Macroporosity is required for large drug loading capacity, osteoid growth, which facilitates the proliferation of cells, vascular growth, and internal mineralized bone formation (osseous regeneration) [14]. The mesoporosity obtained can serve for cell attachment and for the infiltration of the SBF [15]. Hence, the fabricated bioceramic scaffold with hierarchical porosity (designed macroporosity with mesoporosity around the pores) can mimic the structure of the native tissues with concurrent drug delivering ability and simultaneously mimic the biological requirements.

3.2. PCL coatings onto bioceramic scaffolds

The SEM images of the bioceramic scaffolds with PCL coating are represented in Fig. 3. The porosity of the

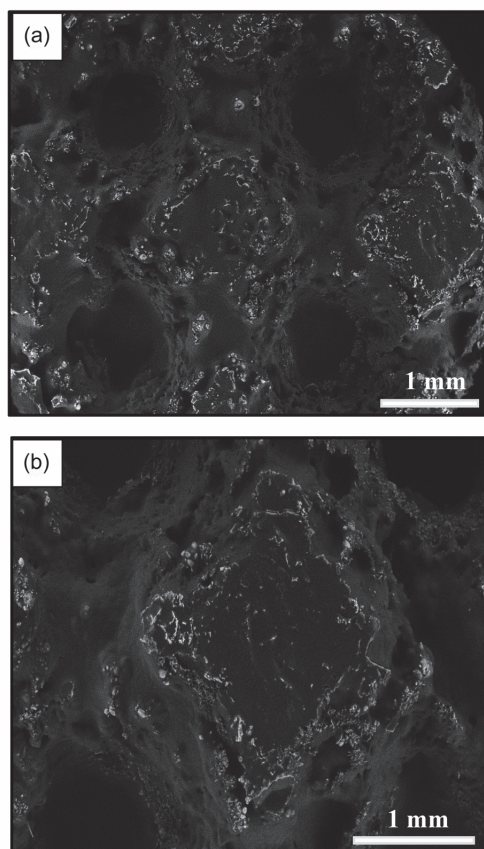


Fig. 3. PCL-coated bioceramic scaffold: (a) the whole scaffold after PCL addition and (b) the interconnective stem.

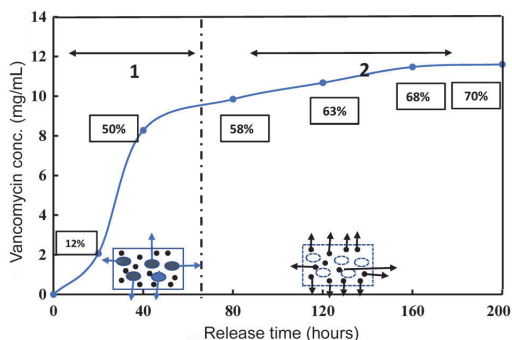


Fig. 4. Vancomycin release profiles from bioceramic scaffolds as a function of release time of vancomycin immersed in simulating body fluids SBF indicating typical drug release kinetics: 1 – fast/burst release, 2 – slow release of vancomycin.

Si–CaSiO₃ scaffolds measured by mercury intrusion porosimetry was approximately 35%. When PCL was coated onto the scaffolds, the morphology of the scaffolds changed slightly. The interconnective stem connecting the pores became thicker (Fig. 3b) and some mesopores were partially closed (Fig. 3a). As they possess good bioresorbability and biocompatibility and show a shielding behaviour for the controlled drug release applications, PCL coatings are widely used in bone tissue engineering [16]. The incorporation of PCL coatings onto bioceramic has yielded a class of biomaterials with remarkably improved mechanical properties, controllable degradation rates, and enhanced bioactivity, which makes these materials suitable for bone tissue engineering. Henceforth, scaffolds are coated with PCL to achieve controlled vancomycin delivery as illustrated in Fig. 4. The morphological features of the coating layer are similar to the reported scaffolds with exactly similar pore size [17].

3.3. Drug release profiles of scaffolds

The fabricated bioceramic scaffolds with porosity may have noteworthy applications for the release of vancomycin. The results demonstrated that the vancomycin loading efficiency ($m_{\text{loaded drug}}/m_{\text{carrier}}$, mg/g) reached up to 16.73 ± 0.82 mg/g. Figure 4 shows the release profiles of vancomycin drug from the scaffolds in SBF at 37 °C. It is clear that vancomycin loaded onto the scaffolds had an obvious two-step release behaviour with an initial fast release and a subsequent relatively slow release stage. The scaffolds exhibited sustained release behaviour throughout the whole study period. More than 50% of the cumulative loaded vancomycin was released from the scaffolds during the first 40 h, followed by a sustained release of nearly 20% of the

vancomycin during the next six days. The subsequent release rate significantly decreased with time, but the cumulative release kept slowly increasing during the next six days, reaching the maximum release of 70% of the loaded vancomycin. The fast drug release can be attributed to the macropores (open porosity) of the scaffolds [18,19]. On the contrary, a slow and sustained drug release can be ascribed to the microporosity of the scaffolds and the release of the vancomycin molecule on the external macropore walls bound by the PCL molecule. To put it in a nutshell, the macro/mesoporous structures of bioactive materials have a sustained release behaviour of vancomycin delivery.

4. CONCLUSIONS

Selective laser melting allows fabrication of 3D porous bioceramic (Si–CaSiO₃) scaffolds. The results showed that bioceramic scaffolds had a regular circular macropore structure with pore size and porosity of ~400 µm and 35%, respectively. Additionally, mesopores were obtained with pore size from 15 to 50 µm. The controllable porosity at both macro- and mesolevels combined with a biocompatible polymer (PCL) coating made it possible to fabricate scaffolds for bone regeneration and to sustain the release of vancomycin. Release of nearly 50% of the vancomycin from the scaffolds was observed during the first 40 h followed by sustained release of nearly 20% of the actually loaded vancomycin for the next six days.

ACKNOWLEDGEMENTS

This work was supported by the personal grant of the Estonian Research Council (PUT1063, I. Hussainova), the European Regional Fund, project No. 2014-2020.4.01.16-0183 (Smart Industry Centre), and Kristjan Jaak scholarship for a short-term study visit to Instituto de Ceramica y Vidrio, Madrid, Spain. The publication costs of this article were covered by the Estonian Academy of Sciences.

REFERENCES

- Bigucci, F., Luppi, B., Cerchiara, T., Sorrenti, M., Bettinetti, G., Rodriguez, L., and Zecchi, V. Chitosan/pectin polyelectrolyte complexes: selection of suitable preparative conditions for colon-specific delivery of vancomycin. *Eur. J. Pharm. Sci.*, 2008, **35**(5), 435–441.
- Joosten, U., Joist, A., Gosheger, G., Liljenqvist, U., Brandt, B., and von Eiff, C. Effectiveness of hydroxyapatite-vancomycin bone cement in the treatment of *Staphylococcus aureus* induced chronic osteomyelitis. *Biomaterials*, 2005, **26**, 5251–5258.
- Proctor, R. A., von Eiff, C., Kahl, B. C., Becker, K., McNamara, P., Herrmann, M., and Peters, G. Small colony variants: a pathogenic form of bacteria that facilitates persistent and recurrent infections. *Nat. Rev. Microbiol.*, 2006, **4**(4), 295.
- Zalavras, C. G., Patzakis, M. J., and Holtom, P. Local antibiotic therapy in the treatment of open fractures and osteomyelitis. *Clin. Orthop. Relat. R.*, 2004, **427**, 86–93.
- Kluin, O. S., van der Mei, H. C., Busscher, H. J., and Neut, D. Biodegradable vs non-biodegradable antibiotic delivery devices in the treatment of osteomyelitis. *Expert Opin. Drug Deliv.*, 2013, **10**(3), 341–351.
- Neut, D., van de Belt, H., van Horn, J. R., van der Mei, H. C., and Busscher, H. J. Residual gentamicin-release from antibiotic-loaded polymethylmethacrylate beads after 5 years of implantation. *Biomaterials*, 2003, **24**, 1829–1831.
- Henry, S. L. and Galloway, K. P. Local antibacterial therapy for the management of orthopaedic infections. *Clin. Pharmacokinet.*, 1995, **29**(1), 36–45.
- Deka, J. R., Song, Y., and Yang, Y. C. The influence of isothermal aging, surfactant and inorganic precursors concentrations on pore size and structural order of mesoporous bioactive glass. *Solid State Sci.*, 2018, **84**, 104–111.
- Du, X., Fu, S., and Zhu, Y. 3D printing of ceramic-based scaffolds for bone tissue engineering: an overview. *J. Mater. Chem. B*, 2018, **6**, 4397–4412.
- Zhang, Y., Zhai, D., Xu, M., Yao, Q., Chang, J., and Wu, C. 3D-printed bioceramic scaffolds with a Fe₃O₄/graphene oxide nanocomposite interface for hyperthermia therapy of bone tumor cells. *J. Mater. Chem. B*, 2016, **4**, 2874–2886.
- Zhou, Z., Yao, Q., Li, L., Zhang, X., Wei, B., Yuan, L., and Wang, L. Antimicrobial activity of 3D-printed poly (ε-caprolactone) (PCL) composite scaffolds presenting vancomycin-loaded polylactic acid-glycolic acid (PLGA) microspheres. *Med. Sci. Monit.*, 2018, **24**, 6934–6945.
- Lee, J. Y., An, J., and Chua, C. K. Fundamentals and applications of 3D printing for novel materials. *Appl. Mater. Today*, 2017, **7**, 120–133.
- Leong, K. F., Cheah, C. M., and Chua, C. K. Solid freeform fabrication of three-dimensional scaffolds for engineering replacement tissues and organs. *Biomaterials*, 2003, **24**, 2363–2378.
- Shruti, S., Salinas, A. J., Lusvardi, G., Malavasi, G., Menabue, L., and Vallet-Regi, M., 2013. Mesoporous bioactive scaffolds prepared with cerium-, gallium- and zinc-containing glasses. *Acta Biomater.*, 2013, **9**, 4836–4844.
- Elsayed, H., Rebesan, P., Crovace, M. C., Zanotto, E. D., Colombo, P., and Bernardo, E. Biosilicate® scaffolds produced by 3D-printing and direct foaming using preceramic polymers. *J. Am. Ceram. Soc.*, 2019, **102**, 1010–1020.
- Hajiali, F., Tajbakhsh, S., and Shojaei, A. Fabrication and properties of polycaprolactone composites containing calcium phosphate-based ceramics and bioactive

- glasses in bone tissue engineering: a review. *Polym. Rev.*, 2018, **58**(1), 164–207.
17. Kim, H-W., Knowles, J. C., and Kim, H-E. Hydroxyapatite porous scaffold engineered with biological polymer hybrid coating for antibiotic Vancomycin release. *J. Mater. Sci. Mater. Med.*, 2005, **16**(3), 189–195.
 18. Parent, M., Baradari, H., Champion, E., Damia, C., and Viana-Trecant, M. Design of calcium phosphate ceramics for drug delivery applications in bone diseases: a review of the parameters affecting the loading and release of the therapeutic substance. *J. Control. Release*, 2017, **252**, 1–17.
 19. Zhang, J., Zhao, S., Zhu, Y., Huang, Y., Zhu, M., Tao, C., and Zhang, C. Three-dimensional printing of strontium-containing mesoporous bioactive glass scaffolds for bone regeneration. *Acta Biomater.*, 2014, **10**, 2269–2281.

Biokeraamiliste nanovõrgustike aditiivne valmistamine vankomütsiini kontrollitud vabanemiseks

Nikhil Kamboj, Miguel A. Rodríguez, Ramin Rahmani, Konda Gokuldoss Prashanth ja Irina Hussainova

Selektiivset lasersulamit on käesolevas töös kasutatud 3D struktureeritud poorsete biokeraamiliste (Si–CaSiO₃) struktuursete nanovõrgustike valmistamiseks. Valmistati ristkülikukujulised komposiidist nanovõrgustikud mõõtmetega 10 × 20 × 5 mm³, mille pooride suurus on 400 µm. Tulemused näitasid, et biokeraamilised struktuurid olid regulaarsed ja ümara kujuga makropoorsusega, kusjuures pooride suurus ja poorsuse väärtus olid vastavalt ~400 µm ning 35%. Lisaks sellele saadi ka mesopoorid poori suurusega 15–50 µm. Kaetud nanovõrgustike puhul uuriti ravimi vabanemise profiili UV-nähtava spektroskoopia abil. Ligikaudu 50% vankomütsiini vabanemine nanovõrgustikust esimese 40 tunni jooksul, millele järgnes ühtlane vankomütsiini vabanemine järgmise kuue päeva jooksul peaaegu 20% ulatuses algsest ravimi kogusest.

Paper III

Nikhil Kamboj, Kazantseva, J., Rahmani, R., Rodríguez, M.A., and Hussainova, I., 2020. Selective laser sintered bio-inspired silicon-wollastonite scaffolds for bone tissue engineering. *Materials Science and Engineering: C*, p.111223, doi.org/10.1016/j.msec.2020.111223.

Reproduced with the permission of Elsevier.



Contents lists available at ScienceDirect

Materials Science & Engineering C

journal homepage: www.elsevier.com/locate/msec

Selective laser sintered bio-inspired silicon-wollastonite scaffolds for bone tissue engineering

Nikhil Kamboj^a, Jekaterina Kazantseva^b, Ramin Rahmani^a, Miguel A. Rodríguez^{c,*}, Irina Hussainova^a

^a Tallinn University of Technology, Department of Mechanical and Industrial Engineering, Ehitajate 5, 19086 Tallinn, Estonia

^b Center of Food and Fermentation Technologies, Akadeemia tee 15A, 12618 Tallinn, Estonia

^c Instituto de Cerámica y Vidrio (ICV-CSIC), C/Kelsen, 5, 28049 Madrid, Spain

ARTICLE INFO

Keywords:

Additive manufacturing
Scaffolds
Biomimetic design
Porous silicon
Wollastonite
Bone
Finite element analysis
Ossification

ABSTRACT

The scaffolds, which morphologically and physiologically mimic natural features of the bone, are of high demand for regenerative medicine. To address this challenge, we have developed innovative bioactive porous silicon-wollastonite substrates for bone tissue engineering. Additive manufacturing through selective laser melting approach has been exploited to fabricate scaffolds of different architecture. Unique material combining osteoinductivity, osteoconductivity and bioactive elements allows flexibility in design. As the porous structure is required for the ingrowth of the bone tissue, the CAD designed scaffolds with pore size of 400 μm and hierarchical gradient of pore size from 50 μm to 350 μm have been 3D printed and tested in vitro. The scaffolds have demonstrated not only the enhanced viability and differential patterning of human mesenchymal cells (hMSC) guided by the biomimetic design onto extra and intra scaffold space but also promoted the osteogenic differentiation in vitro. Both homogeneous and gradient scaffolds have shown the differential expression of primary transcription factors (RUNX2, OSX), anti-inflammatory factors and cytokines, which are important for the regulation of ossification. The effective elastic modulus and compressive strength of scaffolds have been calculated as 1.1 ± 0.9 GPa and 37 ± 13.5 MPa with progressive failure for homogeneous structured scaffold; and 1.8 ± 0.9 GPa and 71 ± 9.5 MPa for gradient-structured scaffold with saw-tooth fracture mode and sudden incognito failure zones. The finite element analysis reveals more bulk stress onto the gradient scaffolds when compared to the homogeneous counterpart. The findings demonstrate that as-produced composite ceramic scaffolds can pave the way for treating specific orthopaedic defects by tailoring the design through additive manufacturing.

1. Introduction

The fusion of additive manufacturing (AM) with tissue engineering has revolutionized the production of novel customized scaffolds. A biomimetic approach to design a substrate inspired by a bone structure combined with capability of the AM to create complex architectures allow fabrication of constructs applicable for tissue engineering and regenerative medicine. With AM as a manufacturing tool and advanced methods of synthesis, the novel composite materials of tailored geometry and properties can be successfully produced to overcome limitations in medicine, renewable energy, and many other fields. In particular, the expansion of AM technology to bone tissue engineering has resulted in production of free-form porous scaffolds of well-controlled pore size, shape and volume without sacrificing the mechanical

performance.

Bone performance can be characterized in terms of geometry, stiffness and toughness due to the hierarchical organization of the structure, which has been perfectly elaborated by nature. Therefore, there are certain requirements for the scaffold to be ideally applied for bone tissue engineering. The predominant objective of the scaffold is to mimic the natural features of the bone; the substrate should be biocompatible, bioactive and biodegradable, osteoconductive and osteoinductive, providing open porosity, while possessing suitable strength and toughness to facilitate bone repair through remodelling and regeneration [1]. Consequently, an impeccable scaffold or biomaterial should not only act as a matrix promoting the osteoblast adhesion but also regulate the biochemical signalling pathways simulating the osteoblast behaviour for bone tissue engineering [2]. Moreover, a

* Corresponding author.

E-mail address: mar@icv.csic.es (M.A. Rodríguez).

<https://doi.org/10.1016/j.msec.2020.111223>

Received 17 April 2020; Received in revised form 15 June 2020; Accepted 19 June 2020

Available online 20 June 2020

0928-4931/© 2020 Elsevier B.V. All rights reserved.

versatile scaffold shaped by additive manufacturing techniques can closely fit into the patient's body to heal either long size or critical sized defects.

A wide variety of biomaterials for bone tissue engineering has recently been developed. Amongst them, there are metallic, ceramics, polymeric and composite scaffolds. The most commonly used metallic scaffolds encircled around stainless steel and titanium-based and metal matrix based biomaterials. However, their low degradability and resorption, relatively high stiffness and stress-shielding phenomenon impede a native tissue from mechanical stimulation [3]. On the counterpart various natural and synthetic clustering ceramics and polymers, have been extensively used. The ceramics and polymers attempt to fulfill the gap left by metallic scaffolds by exhibiting good degradability, biocompatibility, controlled resorption for consecutive neoformation of the bone, and untroublesome tampering in the degradation through copolymerisation and changes in hydrophobicity and crystalline structure [3]. Nonetheless, the single phase scaffold comprising either ceramic or polymer material limits the applications to non-loading bearing applications and non-critical sized defects.

In order to unravel the problem, various bio-composites have been tested. The primary objective of the composite scaffold is to coalesce two or more materials to improve the printability of the constructs with tailored architecture and required mechanical performance [4]. Wollastonite, a naturally occurring calcium silicate mineral, has been extensively used as an active filler in both ceramic-ceramic and ceramic-polymer composites due to the mechanical properties, which can be accredited to its acicular structure, and its ability to hamper the fracture by impeding the crack pathway [5]. The hydrophilic nature of the wollastonite facilitates the formation of the apatite layer promoting wollastonite usage for bone tissue regeneration. Moreover, the early stage lixiviated calcium ions from wollastonite regulate the osteoblast proliferation and differentiation [6] and have the potential to upregulate several bone markers genes expression of the stem cells such as BMP-2, RUNX2 gene, transforming growth factor (TGF- β), ALP and osteocalcin in-vitro. Ions of silicon are not only involved into secretion of extracellular matrix, but also play a crucial role in activation or deactivation of mitogen-activated protein kinase (MAPK) MAPK/ERK and MAPK/p38 signalling pathway [7]. Additionally, wollastonite based silicate materials may influence the regulation of immunomodulation causing the downregulation of the inflammatory MAPK and NF- κ B signalling pathways and the upregulation of the apoptosis of macrophages by a caspase-dependent pathway [8].

Wollastonite added ceramic-polymer composites, which were explored as the potential orthopaedic implants, are mostly fabricated with the help of physicochemical and thermomechanical methods, which are constrained in freedom of design. Over the past few years, additive manufacturing has been used as a tool to fabricate the wollastonite-based composites for bone tissue engineering. Recently, the "diamond cell" architected wollastonite-dioside glass-ceramics biocomposites were produced by digital light processing (DLP) with [9] apatite-wollastonite reinforced PLLA matrix scaffolds was fabricated using a fused filament approach [10]. The new dilute Mg-doping β phase of wollastonite scaffolds was prepared by direct ink writing [11]. The apatite-wollastonite-poly (lactic acid) scaffolds was fabricated by two step technology comprising 3D printing of PLA matrix which was subsequently followed by thermal treatment to form hybrid material [12]. The bioactive wollastonite and wollastonite-based composites have the property of osteoconduction and bonding with the living bone tissue by the so-called process of "bonding osteogenesis". However, the bioactivity is not only the important key factor to determine the ideal scaffold but also it should possess good degradability and osteoinductive properties too. The scaffolds for the bone repair should degrade over the passage of time; and the degradation should be neither too fast [13] nor too slow [14].

One of the osteoinductive and biodegradable materials, which is used over the past two decade, is porous silicon, as silicon plays a

crucial role in the development and nourishment of the bone. Silicon matrix is well sustained in the human body with neither inflammatory nor infectious reactions of the host. Additionally, the porous silicon matrix, when hydrolysed by body fluids, is converted to non-toxic silicic acid - the major form of silicon in the human body [15] and may be beneficial for creation of a cell interface to support osteoblast and collagen fibrils [16] and inhibition of osteoclasts development and bone resorption activities [17]. Porous silicon is also proven to play a vital role in assisting and promoting the formation of the actin microfilaments from the stem cells [18]. Pairing of porous silicon and human mesenchymal cells (hMSC) has led to various therapeutic effects for the regenerative medicine and personalized medicine, which can be attributed to the ability of MSC to differentiate and self-renew to multiple tissues [16,19,20].

Tailoring the pore morphology, porosity and size can affect the physiological fluid rate; particle size distribution can hamper extracellular enzyme activity, divergent gene expression; and crystallinity can alter intercellular activity. For instance, tuning of the pore size of porous silicon has resulted in differential expression of bone marker genes and neuronal associated genes [21]. The micropores of 10–50 μ m are required for physiological fluid infiltration, cell adhesion, rapid exchange and diffusion of oxygen and nutrients and waste clearance [22]. The macropores sizes from 100 to 400 μ m are needed for the cell infiltration and building of new bone tissue layers [22,23]. The porous silicon matrix has been usually fabricated by conventional anodization and stain etching methods for porosification. The laser-assisted approaches combined with precise bioinspired design have never been reported in the literature.

In this work, the approach of additive manufacturing through a selective laser melting (SLM) as an effective technique to fabricate a novel metalloid/ceramic composite scaffold is used for the first time. Unique material combining osteoinductivity with osteoconductivity and bioactivity is developed allowing flexibility in design and lack of volumetric shrinkage. The material of macro-porous silicon reinforced by bioactive acicular wollastonite, which is produced with customized complex geometry and porosity, is an effective solution for bone tissue engineering. Homogeneous and gradient scaffolds of distinct geometries, which previously could not be easily engineered, were designed to mimic the microenvironment of the bone. For instance, structural gradient of the radially distributed pores can facilitate a long bone formation; whereas the axially distributed pores can enhance a flat bone formation [22]. The gradient scaffold not only improve the cell-seeding efficiency, but also assist the osteogenic differentiation due to availability of nutrients and subsequent tissue development [24]. This kind of fabrication technology with biomimetic design for homogeneous and gradient scaffolds can further guide the stem cells behaviour to the differential expression of the biological signalling molecules.

2. Experimental

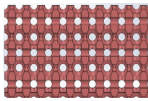
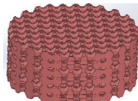
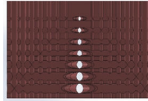
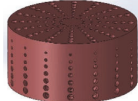
2.1. Scaffolds design

To fabricate three-dimensional scaffolds of 6 mm in height and 5 mm in diameter, a computer aided design was sketched with the pore diameters for the homogeneous(H) scaffolds to be 400 μ m and the gradient scaffolds(G) from 50 μ m to 350 μ m using SOLIDWORKS® (Dassault Systems, USA) as shown in Table 1.

2.2. Powder feedstock

The material used was a mixture of 30 wt% silicon and 70 wt% wollastonite. The powders of silicon (> 99.9% purity, particle size range 10–44 μ m, *Silgrain-Elkem*, Fig. 1a) and wollastonite (> 99.9% purity, particle size range 1–10 μ m, *NYCD® M1250*, Fig. 1b) were mixed in the Turbula® shaker for 3 h with ethanol using ZrO₂ balls. The obtained mixture was dried in an oven heated to 120 °C for 24 h.

Table 1
Morphology and CAD 3D design of the scaffolds.

Type of scaffold	Pore size	Designed pores	CAD 3D design
Homogenous (H)	400 μm		
Gradient (G)	50 μm ↓ 350 μm		

2.3. Processing

Scaffolds were fabricated by metal 3D printer using a commercial ReaLizer GmbH SLM-50, Germany, SLM system. The optimized process parameters were applied for production of the porous substrates with layer thickness of 25 μm , hatch distance of 60 μm , and point distance of 10 μm at a scanning speed of 80 mm/s. Additionally, the macroporous silicon scaffolds of the same CAD design were manufactured exploiting the process parameters as specified in Table 2. The procedure was performed under the high purity argon (99.999 vol%) in order to avoid undesirable oxidation. During SLM, a rubber wiper spreads the composite powder feedstock over the surface of a stainless steel cylindrical platform. No post-treatment of the sintered materials was required after SLM, which ultimately reduces the cost of the whole process. The loose powder adhered to the scaffolds was removed by a sonicator kept in ethanol for 15 min.

2.4. Microstructural analysis

Phase composition of the crushed scaffolds was evaluated by X-ray diffraction (XRD; D5005, Bruker, USA) operating at $\text{CuK}\alpha 1$ radiation ($\lambda = 1.5406 \text{ \AA}$) with a step of $0.02^\circ (2\theta)$ in the range of $20^\circ - 70^\circ$ with the assessment and optimization of the relative counts by Rietveld refinement method. Scanning electron microscopy (SEM Zeiss EVO MA 15, Germany) equipped with EDS with a voltage of up to 20 kV and magnifications up to 50 kX was used for examination of the as-produced products. The gold-coated samples were studied under secondary and backscattered electrons modes. The front and cross section details of the scaffolds were examined using MEDIX technology MXT 225 HU-CT machine. A rotational step of 0.9° over an angle of 180° was imposed to obtain the images of the scaffolds. The images of the (H) and (G) scaffolds were taken from three different samples of each type. The visualization and 3D representation of the scaffold were performed through $\mu\text{-CT}$ analyser. The scaffolds were reconstructed comprising

Table 2
Process parameters.

Samples	Laser power (W)	Energy density (J/mm^3)
Macroporous silicon	34	283
Bulk composite	32	267
(H) and (G) scaffolds	26	217

120 slices using a circular region of interest (ROI). Subsequently, the identical threshold values were defined for the same region of (H) and (G) scaffolds in all three different samples of each type in-order to minimize the image noise and differentiate between the dense materials from pores. The threshold values were reformulated and inverted to obtain the porosity of the scaffolds.

2.5. Compression tests

The cylindrical porous samples of 6 mm (± 0.1 mm) in diameter and 5 mm (± 0.1 mm) in height were tested under compression at room temperature at an applied strain rate of 0.5 mm min^{-1} using the servo-hydraulic model 8500 universal testing machine (Instron ltd., UK). The compressive load and displacement were recorded at each 0.1 s intervals during testing. Elastic modulus and maximum compressive strength were determined using software associated with the testing machine. The compressive strength of the scaffolds were also measured after immersing in Tris buffer solution at pH 7.4 and 37°C for 3, 7 and 14 days (solution volume to scaffold mass: 1 L/g), which later were dried at 120°C . All the compressive strength measurements on the scaffolds were performed at room temperature.

The mechanical performance of the structures was also evaluated computationally using a finite element (FE) analysis. Modelling was carried out on the scaffolds with a constant deformation rate of 0.5 mm min^{-1} in order to be consistent with the experimental compression uniaxial deformation. The commercial FE ANSYS® 17.2 package was used for the estimation of a local stress distribution. The 10 noded tetrahedral elements were introduced in order to achieve the fine mesh structure.

2.6. Cell cultures and cell staining

Human MSCs were obtained from a freshly isolated subcutaneous adipose tissue as detailed in [25]. Cells were grown in DMEM with 10% FBS, 1 mg/mL penicillin and 0.1 mg/mL streptomycin at 37°C in 5% CO_2 . UV-C treatment was imparted to the scaffolds to prevent any contamination to the cell culture. The scaffolds were infiltrated with nutrients from DMEM consecutively three times in the passage of 24 h prior to cell seeding in order to saturate the scaffolds with the active components from the medium.

The hMSCs were seeded on the surface of the scaffolds in 12-well plate at 4×10^4 per well, correspondently. On the counterpart, similar

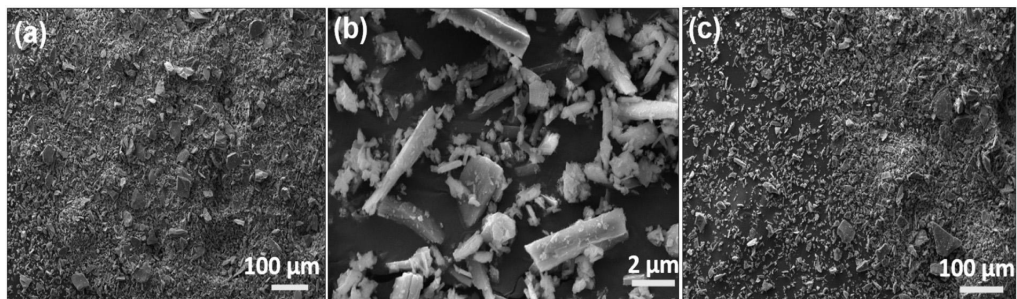


Fig. 1. Microstructure of the precursor powders: a) silicon; b) acicular wollastonite; c) mixed powder.

cells were grown on the flat glass with the same culture condition to be used as the control and reference. The visualization of the cells adhered onto the scaffolds was performed using a specific to filamentous actin (F-actin) phalloidin tagged by FITC (Sigma). The cells were fixed by 4% PFA at 48 h after seeding, washed by PBS and permeabilized by 0.3% TRITON X-100 in PBS for 5 min. The scaffolds were kept for 18 h at 4 °C, which allows Phalloidin-FITC (1:100) staining, and 2 h at RT for cells cultured on the flat glass (control). For nucleus staining, cells were incubated with Hoechst 33342 (Invitrogen, 1 µg/mL) for 10 min. After a final PBS wash, the phalloidin-stained cells were analysed by Nikon Eclipse 80i microscope

2.7. RNA extraction, cDNA synthesis and RT-qPCR of osteogenic genes

4×10^4 cells were seeded per each scaffold or cell culture well. RNAs were extracted directly from cells grown on the scaffolds by in-vitrogen kit according to the manufacturer's recommendations. Equal amount of RNA concentrations were used for (H) and (G) scaffold with the concentration of 30 ng/µl. The cDNAs were synthesized from 9.75 µl of DNase-treated (Ambion) RNA with 22.75 µl RevertAid Reverse Transcriptase (Thermo Fisher Scientific). The quality of the cDNA was affirmed by RT-PCR using GAPDH primers and HOT FIREpol® Master Mix (Solis Biodyne, Estonia). To evaluate the level of osteogenic differentiation, such kind of genes were analysed after 21 days: OCN, OPN, COL1a1, RUNX2, OSAD, ALP, MSX2, TFGβ, IL8 and TSG6. The experiments were performed in triplicates using EvaGreen qPCR mix plus no Rox (Solis Biodyne, Estonia) and the StepOnePlus™ Real-Time PCR System (Thermo Fisher Scientific). The fold change of the gene taken into consideration was calculated relatively to the control (cells grown without scaffolds) after normalisation to GAPDH expression, using 2- $\Delta\Delta C_t$ method (double difference of C_t). The values were respectively calculated as $\Delta C_t = C_t(\text{gene of interest}) - C_t(\text{GAPDH})$, and $\Delta\Delta C_t = \Delta C_t(\text{treated}) - \Delta C_t(\text{control})$ [26]. Henceforth the illustrated data represents the two different and independent analyses normalized to the level of expression of hMSC [cells grown excluding porous silicon-wollastonite scaffolds] and further converted to log scale.

2.8. Statistical analysis

The values were presented as the mean \pm SD and analysed with Student's *t*-test, in which differences were considered statistically significant when $p < 0.05$.

3. Results

3.1. Silicon scaffolds

Fig. 2(a, b) shows the SLM fabricated porous silicon scaffold. The

CAD designed pores of 400 µm are well recognized in the SEM images.

The morphology of the scaffolds depends on the process parameters (laser power and energy density) to a great degree. Recent study [27] has demonstrated that the laser power of 34 W with the energy density of 283 J/mm³ is suitable for complete densification of the silicon powder by SLM. Herein, the laser current of 32 W with the energy density of 266 J/mm³ was applied for fabrication of the silicon scaffolds with the pore size of 400 µm (Table 2) conditioned by the fact that a high laser energy can significantly reduce the viscosity of the molten silicon, which can readily flow to join the large droplets in the melt pool, and decrease the pore size in the construct. Furthermore, the Nd³⁺: YAG laser contributes to the sintering of silicon particles and formation of a porous silicon matrix as shown in Fig. 2(a, b). The differential pattern of the silicon particles adhesion after the SLM processing and the intrinsic feature of the SLM technique imparts surface roughness on the scale of several micrometres [28].

The next step was to fabricate the silicon-wollastonite composite scaffold with a different geometrical design (H or G, Table 2) compatible for bone tissue engineering and taking into consideration the process parameters window working for SLM of the pure silicon.

3.2. Analysis of composition

After SLM processing, the main phases detected in the scaffolds were silicon [ICSD, 00-027-1402, cubic], wollastonite [ICSD, 04-016-5334, Triclinic] and pseudo-wollastonite [ICSD, 04-012-1776, Monoclinic]. In the previous study [29], the silicon-wollastonite based scaffolds with 50-wt% of each component have shown an evidently pronounced increase in the crystallinity of the phases after SLM as compared to the powder feedstock.

As it can be observed from Fig. 3(a, b) there is no noticeable difference in the phases presented in homogenous and gradient scaffolds suggesting the homogeneous mixtures of the powders, as well as repeatability and reproducibility of the process. The acicular wollastonite interaction with the Nd³⁺ YAG laser had led to a higher temperature polymorph of wollastonite or pseudo-wollastonite. The upper temperature stability of wollastonite is 1150 °C, and beyond that, there is a transition to pseudo-wollastonite phase. The pseudo-wollastonite can also be recognized in Fig. 3(a, b), which confirms the co-existence of wollastonite and pseudo-wollastonite. This can be attributed to the fact that the melt pool formed was not uniform, which was conditioned by irregular shaped powder particles. The wollastonite and pseudo-wollastonite phases were detected in both (H) and (G) scaffolds. In principal, the pseudo-wollastonite is considered as a promising material for bone generation and can enhance cell activity and osteoblast differentiation [30]. The difference between the phases is the crystal structure: a "three-ring silicate" crystal structure of a stable wollastonite as compared to a "chain-silicate" structure of unstable wollastonite, i.e. pseudo-wollastonite [31].

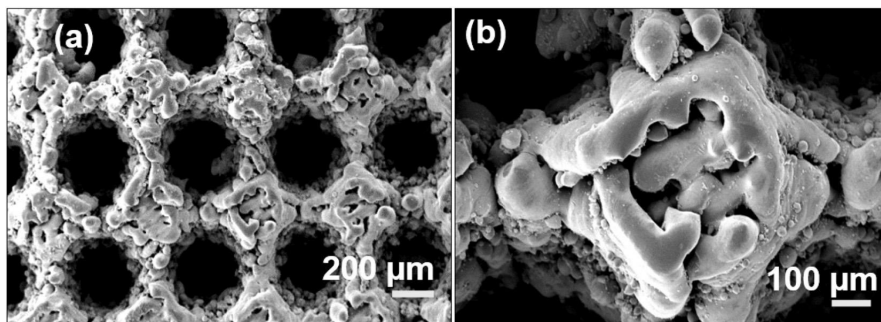


Fig. 2. SEM micrographs of macroporous silicon scaffolds.

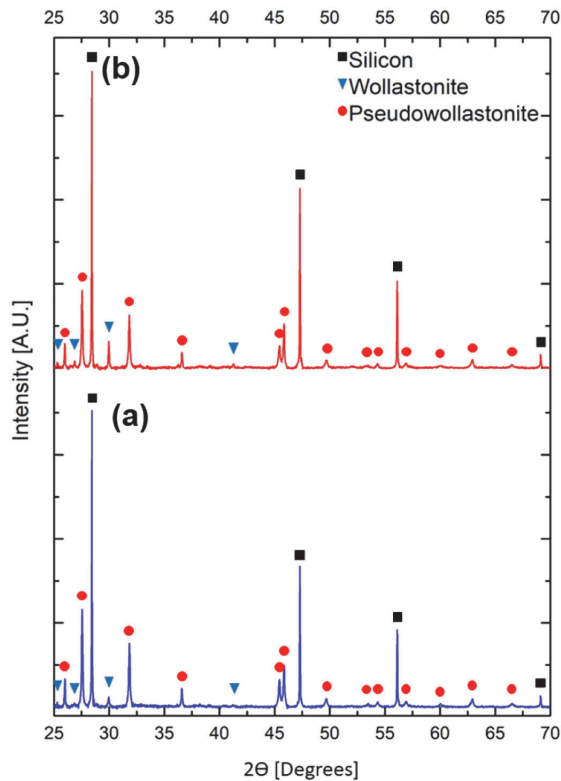


Fig. 3. XRD of the SLM processed crushed scaffolds; a) (H); b) (G) scaffolds.

3.3. SLM fabricated composite scaffolds

Fig. 4 represents the scaffolds design depicting its pore morphology and 3D models. The (H) scaffolds with pore size of 400 μm and (G) scaffolds with gradient pore size from 50 to 350 μm clearly replicated the scaffolds microstructure given in Fig. 4(a, d). The (G) scaffold was designed to have both radial and longitudinal gradient in pore size required for both long bones and flat bones, as small pores allow high vascularization and large pores facilitate direct osteogenesis and formation of the multiple tissues and tissue interfaces [22].

The gradient in (G) scaffold longitudinal pore size is demonstrated in Fig. 4(d). The pores connectivity is slightly different in (G) and (H) scaffolds. Representative SEM images of (H) scaffolds in Fig. 4(a, c) shows the continuous connectivity of at least four macropores with the interconnected strut as observed in the porous silicon scaffolds in Fig. 2b. On the counterpart, the pores of the gradient scaffolds are not connected being separated in longitudinal and radial direction (Fig. 4(d)).

Wollastonite is quite homogeneously dispersed throughout silicon as depicted by the EDS elemental mapping, which displays Si in green and calcium in red, Fig. 4(b, e).

Fig. 4(c, f) show the $\mu\text{-CT}$ images of the (H) and (G) scaffolds with the macropores, respectively. The composition of silicon and wollastonite was opted since silicon being osteoconductive and osteoinductive and wollastonite imparts bioactivity to the scaffold. For (H) and (G) scaffolds, the $\mu\text{-CT}$ of the five samples was taken into consideration and a total porosity of 41 vol% and 30 vol% was measured, correspondingly. The pores gradient from the small to larger ones is demonstrated with the help of a red arrow in $\mu\text{-CT}$ image of the (G) scaffold, Fig. 4(f).

The supremacy of the SLM technique as compared to other AM approaches can be accredited to the fabrication of substrates with different porosity, controllable pore size, no binder addition and no post-processing stages. Furthermore, removal of binder, geometric constraints, sintering and other additional treatment steps are not only time consuming, but also affects the degradation of physical-chemical characteristics of the as-produced porous scaffolds.

3.4. Silicon matrix containing acicular wollastonite

Fig. 5 demonstrates the localization of silicon and wollastonite particles throughout the (H) scaffold and a bulk comprising the same composition. Relatively large areas of Si can be attributed to much more likely laser interaction with the large particles (silicon) than with smaller acicular particles (wollastonite).

The wollastonite particles are clearly recognizable being embedded onto the silicon matrix as indicated by arrows in Fig. 5(b). The bioactive particles of wollastonite are supposed to leach in the body fluids first. The authors' study [29] has indicated the degradation of as-fabricated scaffolds with 50 wt% of each component and revealed that the Ca/Si ratio was 1.60 after the first day of the test, and decreased to 0.65 after the 14th day. Such kind of behaviour suggests the release of wollastonite in Tris buffer, which evidences the attachment of wollastonite to the particles onto the silicon matrix. The high magnification image in Fig. 5(b) displays the relatively homogenous distribution of wollastonite particles on the matrix' silicon, which may be accredited to robust convention muster by rapid heating and solidification. It is worth mentioning that the top layer of the SLM printed bulk exposed the microstructure with heterogeneous grain boundaries of the silicon particles rich with acicular wollastonite.

3.5. Compression test

In Fig. 6, the stress – strain curves of the structures developed are demonstrated. The stress-strain curves begin with a linear elastic response followed by nonlinear behaviour with the applied stress. The plot depicted for (H) scaffold reveals a linear response until about 40 MPa followed by a multi-peaks profile, which is typical for cellular structures, Fig. 6a. The curve has a positive slope up to the highest stress of 37 MPa, and then gradually proceeds with a negative slope pointing at the cracks system development. The gradient scaffold (G) withstands twofold higher stress level linearly reaching 72 MPa, Fig. 6c. The effective elastic modulus and the compressive strength are calculated to be 1.1 ± 0.9 GPa and 37 ± 14 MPa for (H) scaffold; and 1.8 ± 0.9 GPa and 71 ± 10 MPa for (G) scaffold, respectively. The stress-strain response of the (H) scaffolds shows continuous progressive failure of the construct owing to its uniform and homogeneously distributed pores. Correspondingly, the (G) scaffolds demonstrates the sudden “incognito” failure zone, which can be attributed to the fact of non-homogeneous stress distribution towards differently sized pores. Such kind of behaviour may have real implications when scaffolds are implanted for long or flat bones restitution since the gradient in porosity can support the interphase separating the dense from the porous part in the long bones axially and in the flat bones longitudinally.

The compressive strength of the as-fabricated scaffolds is greater than the strength of a trabecular bone (1–10 MPa) but less than the stress of a cortical bone (110–230 MPa). One of the remarkable features of the powder feedstock for the scaffolds of the developed composition is a flexibility in production of powders of the specified ratio of the components, which can be tailored for custom needs. For instance, the effective elastic modulus and compressive strength of 2.9 ± 0.3 GPa and 110 ± 5 MPa was measured for the material comprising 50 wt% of each component; therefore, such kind of materials may be considered as a promising candidate for treating the cortical bone defects [29].

Furthermore, the stress distribution was assessed by finite element analysis. The compressive force was uniaxial applied onto the top

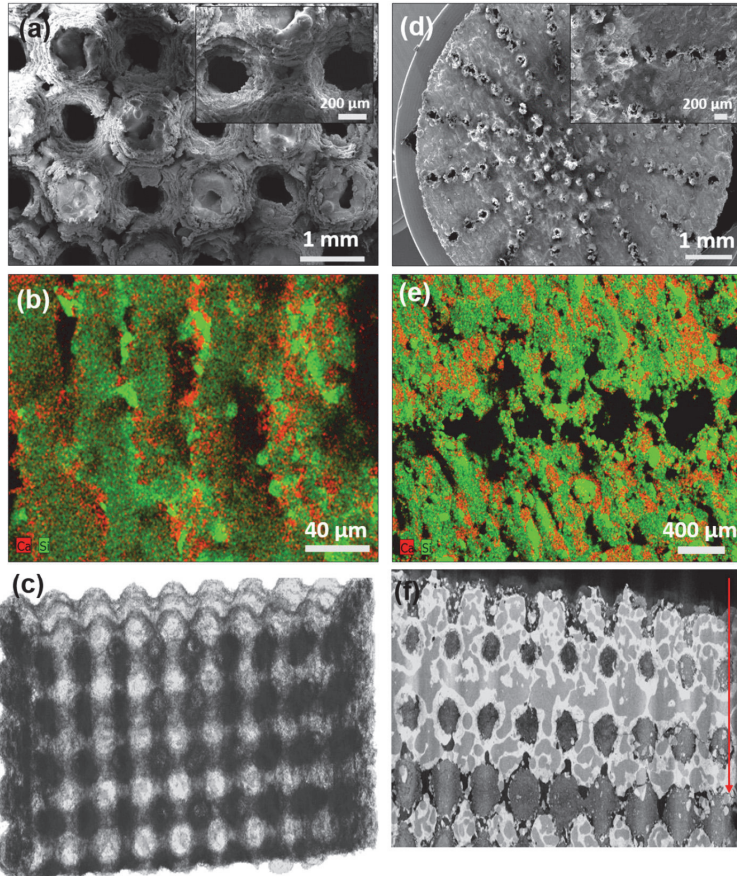


Fig. 4. (H) a) SEM micrographs of the (H) scaffolds; b) EDS element mapping of the (H) scaffold; c) μ -CT image of the (H) scaffold; (G) d) SEM micrographs of the (G) scaffold; e) EDS element mapping of the (G) scaffold; f) μ -CT image of the (G) scaffold.

surface of the CAD model keeping the bottom fixed. The response of the structures were modelled in the linear portion of the stress-strain curve. The non-linear stress-strain section of the curve was not modelled since it leads to the reduction in the overall stress with the constant increase in the deformation. The non-linear stress - strain section of the curve evoked from 8% and 6% strain in (H) and (G) scaffold, respectively. The Fig. 6(b, d) illustrate the patterns of the stress distribution onto the (H) and (G) scaffolds under the constant deformation. The red spots or patches denote the most stressed areas; and the greenish yellow ones points to the stress concentration around the pores. The greenish blue contour corresponds to stress of ~ 47 MPa and ~ 77 MPa for homogeneous and gradient scaffolds, respectively. For both constructs, the least stress was observed at the middle region and at the point of scaffold fixation to the support. The highest stress was concentrated at the surface of both scaffolds in a close proximity with the mesh.

The changes in the compressive strength of the (H) and (G) scaffolds in the after be in contact with Tris buffer solution is depicted in Fig.7(a, c) with the passage of days. It was observed that the compressive strength of the (H) and (G) scaffolds decreased with the immersion time by 16% and 12% during the passage of two weeks respectively when compared with the original scaffolds (dry conditions). In-order to deduce the effect of the dissolution, the morphologies of the scaffolds were studied by SEM as shown in Fig. 7(b, d). The red arrows indicated in Fig. 7(b, d) shows the ramifications of the dissolution behaviour in

Tris buffer which leads to the loosening of the grains. The dissolution may have taken onto preferred crystallographic planes, which consequently depends on the orientation of the grains. The orientation of the grains relies on the melting/sintering phenomenon and thus can have several repercussions on the patterning of loosening of the grains [32].

3.6. Cytocompatibility assessment of the scaffolds

The most essential requisite for the scaffolds to be used in bone tissue engineering is a relevant biomaterial with a desired pore size. Both of the porous silicon wollastonite and pseudo-wollastonite scaffolds are considered as excellent substrates for the cell attachment and proliferation [16,30,31]. Fig. 8(c-f) shows that hMSCs are capable to grow on the silicon-wollastonite composite (H) scaffold, Fig. 8(c, d), and on the (G) scaffold, Fig. 8(e, f). Additionally, migration of the cells are vital that can change the cell density, oxygen and nutrient availability. These factors are seemed to be associated with the pore size [33]. The distinguishing feature of the hMSCs grown on the scaffolds and on the reference glass is the presence of pores and the complex 3D geometry affecting the stem cells morphology after 48 h. The hMSC appeared to be well anchored to the (H) scaffolds, Fig.8(c, d).

The spindle shaped cells with more than usually extended cytoplasmic lamellipodia extensions were well-connected indicating a better initial cell attachment onto the 3D printed (H) scaffold. The

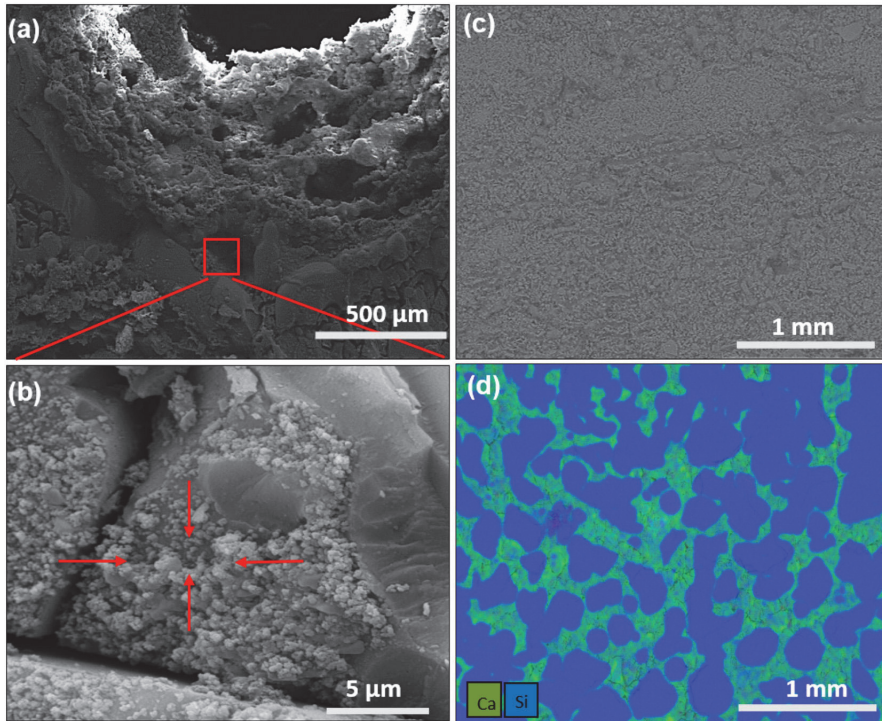


Fig. 5. Schematic representation and mechanism of the produced silicon-wollastonite scaffolds by SLM; a) and b) (H) scaffold; c) and d) bulk composite.

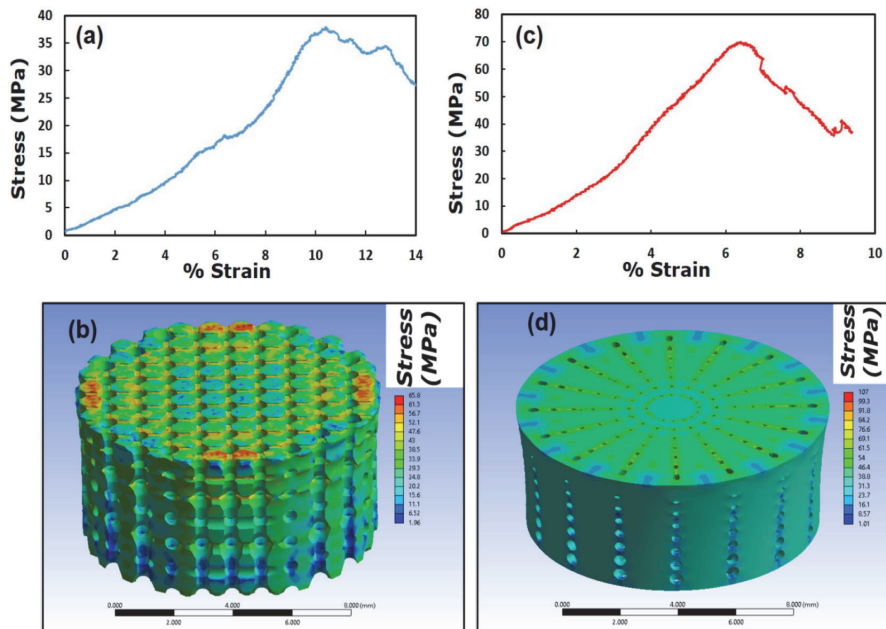


Fig. 6. a) and b) Experimental stress-strain response and finite element analysis of (H) scaffolds; c) and d) (G) scaffolds.

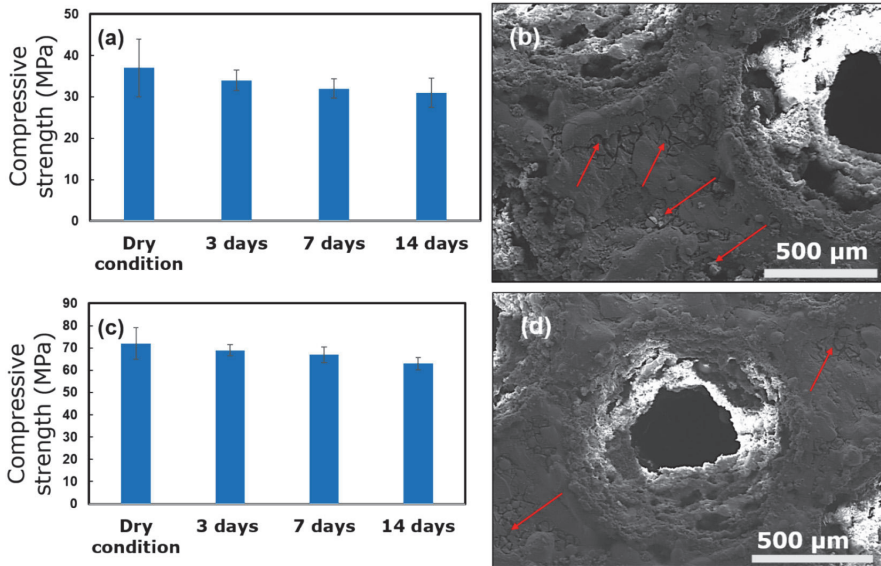


Fig. 7. a) Changes in the compressive strength of the (H) scaffold with the passage of days (soaking time) in Tris buffer solution when compared with dry condition scaffold (As obtained) and each value mean \pm error bar with standard error of the mean, $n = 5$, (b) SEM morphology of the (H) scaffold after 14 days immersion in Tris buffer solution; c) and d) (G) scaffold.

extended morphology of the hMSC can be attributed to a suitable connectivity, which is one of the major pre-requisites for favoured osteo-lineage differentiation to extracellular matrix needed by osteoblasts to proliferate. It was observed that hMSCs were well-adhered onto the (G) scaffold surface (extra scaffold space) encircling and guided by the biomimetic design of the pores, Fig. 8e. The hMSC were

seen communicating each other in the intra-scaffold space provided by the largest pores, Fig. 8f. Cell migration in and out (from extra-scaffold space to intra-scaffold space) in the (G) scaffold through the pores sized from 100 μm to 350 μm can be beneficial for the bone tissue regeneration. The arrangement of the cells can facilitate the cell-surface interaction by promoting direct bonding and, therefore, enhance the

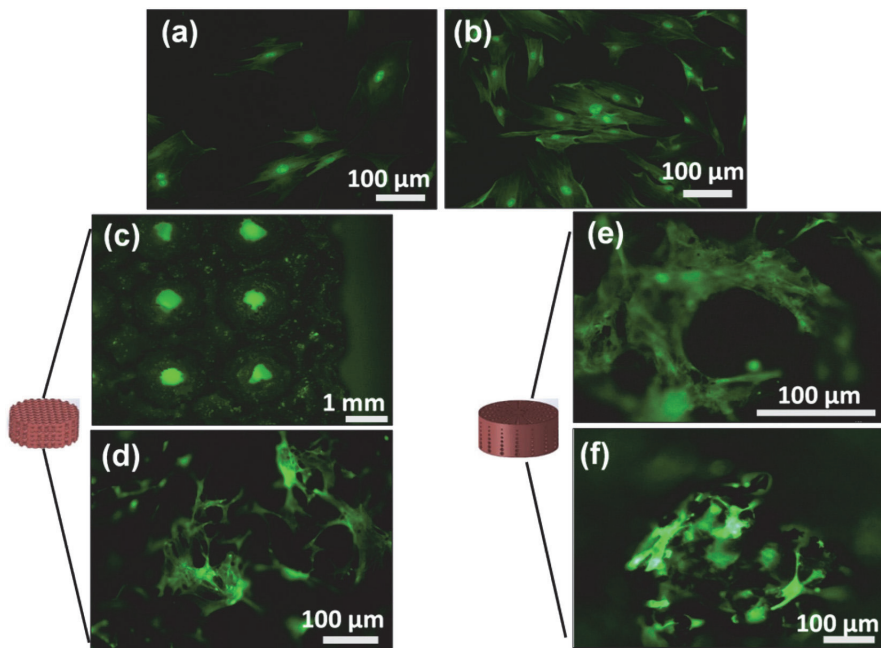


Fig. 8. The fluorescence microscopy images of hMSCs grown on glass (a, b), (H) scaffolds (c, d) and (G) scaffolds (e, f).

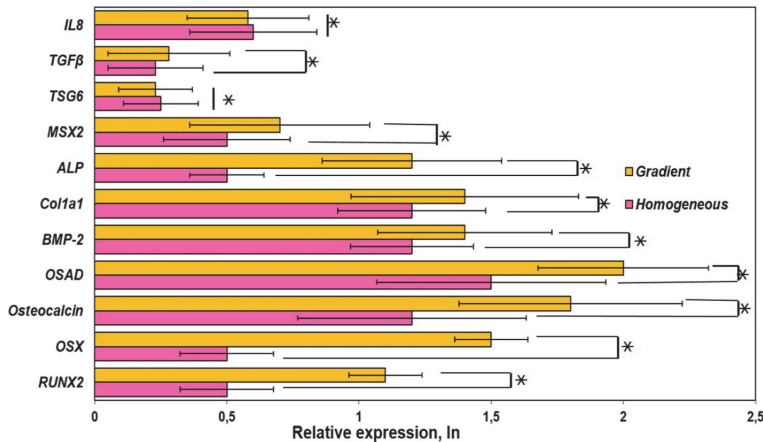


Fig. 9. RT-qPCR shows the dynamic potential of MSC differentiation to osteo lineages by (H) and (G) scaffolds. * symbol indicates statistical significance ($P < 0.05$).

bone tissue formation with profound media flow of nutrients allowing the differentiation of hMSC to osteoblast cells [33]. Additionally, it could affect cell behaviour in regard to extracellular matrix deposition and differentiation [34].

3.7. Osteo-lineages studies

The induction of the osteogenic features by (H) and (G) scaffolds were evaluated by mRNA levels of RUNX2, OSX, osteocalcin, OSAD, BMP-2, Col1, ALP, MSX2, TSG6, TGFβ1 and IL8 through MSC seeded onto the scaffolds microenvironment, Fig. 9. Analysis of the MSC was performed in the absence of either chemical or biological stimulus. Induction of the RUNX2 and OSX, the primary transcription factors for osteogenic differentiation, was found in both scaffolds. The expression of both transcription factors were expressed nearly twice in (G) scaffolds as compared to (H) scaffolds. The induction of the RUNX2 plays a pivotal and stimulatory role in the osteoblast differentiation. ALP, type I collagen (Col1a1) genes clearly shows the up-regulation of the relative expression in gradient scaffolds. Although the cell number seeded and the calcium production per volume onto the (H) and (G) scaffolds were not evaluated, the elevation of the certain early osteogenic transcription factors like RUNX2 and OSX can be observed in the gradient scaffold. This can be attributed to re-distribution of the hMSC along the differential pores with a higher nutrient and oxygen availability as compared to (H) scaffolds.

The ossification is controlled not only by the transcription and mineralization factors, but also by certain cytokines such as TGFβ, IL8 and TSG6, which were also evaluated in this study. The relative expression of the cytokines was relatively similar in (H) and (G) scaffolds. The up-regulation of IL-8 and TGFβ, which are anti-inflammatory factors, demonstrates the possible immunomodulation effect. The induction of TSG6 in both scaffolds was considered advantageous as TSG-6 regulates the bone remodelling by maintaining the stasis between osteoblasts and osteoclasts.

4. Discussion

Large bone defects as the result of various injuries results in non-unions and non-healing of bone [35]. The autologous, allogenic and xenografts had been used in the past and were regarded as the gold standard for bone repair [36]. However, these grafts were exposed to several limitations like donor-site infection etc. [36]. Therefore, synthetic grafts including have been promising approach for repairing bone tissue [37]. Synthetic bone grafts especially bioceramics based scaffolds

comply with the requirements for bone tissue engineering.

Silicon plays a prominent role in osteogenesis and essentially as an ion, it has proven its potential with enhanced osteogenic activity for the last 50 years [38]. Silicon is crucial for calcification of the bone tissue and boosting of the bone density [39]. Pure silicon passes to the solutions through the dissolution of the SiO_2 or silicon hydroxide layers that eventually forms on its surface because of high enthalpies of formation ($-915 \text{ kJ}\cdot\text{mol}^{-1}$) of silicon oxide [40]. Particles of the silicon can be easily excreted out by the human kidneys through silicic acid [41]. Orthosilicic acid, major dietary form of silicon has also proven the COL-1 synthesis by stabilising the glycosaminoglycan network via silanolate bonds and elevated osteoblastic differentiation [42]. Sun et al. [43] observed higher amount of bone tissue on macroporous silicon (MacPsi) than bulk silicon to heal cortical bone defects for bone tissue engineering [44]. Pure silicon coatings were also used to control corrosion and bioactivity of some alloys based implants [44]. However, pure silicon for bone tissue engineering can experience several problems due to its lower solubility and since, physiological fluid is a dynamic system, which could result in degradation problem. Henceforth, in order to unravel the problem of slow degradation of the silicon, new composites were designed using wollastonite and pure silicon, since wollastonite have relatively higher rate of dissolution in the simulating body fluids [45]. These composites can be the potential solution for the fractures where immediate support is needed as the early dissolution of wollastonite could trigger the formation of nascent bone due to the bioactivity and induction of the early osteoblastic genes. Simultaneously, silicon particles still holding the fracture and can provide the crucial support with matched biodegradation rate, which is vital to achieve an ideal repair outcome.

In our work, a comparative analysis was made between (H) scaffolds of pore size (400 μm) and (G) scaffolds of pore size (50–350 μm). The scaffolds were fabricated using silicon and wollastonite as the starting material by selective laser melting. The (G) scaffold of the pores (50–350 μm) were designed having the gradient in the pore sizes both radially and axially since radially distributed pores can facilitate a long bone formation; whereas the axially distributed pores can enhance a flat bone formation [22]. Differential pore sizes in the (H) and (G) scaffolds has affected the differentiation of hMSC towards osteo-lineages genes.

Very few studies in the literature were devoted to annihilate the role of the pore size and porosity onto the osteo-lineages in-vitro and cell migration. One study demonstrated the cell migration in the pore size ranging from 40 to 100 μm [46,47]. The rat osteoblasts were seeded onto the scaffolds with pore size ranging from 40 to 100 μm and more

cells were found clustering the small pore of 40 μm . Additionally, they also observed that more cells were migrated onto intra and extra scaffold space through pore size of 100 μm , which consequently can enhance the nutrients transfer ability of the pores [47]. The similar patterning of the MSC clustering was observed around pore size < 50 μm [48]. Pore diameter ranging from 20 to 30 μm have simulated more activity of osteocalcin and alkaline phosphatase than the pore size > 50 μm [48]. In the same study, higher porosity (scaffolds) did not contribute to the cell attachment but conclusively facilitated cell movement with nutrients transfer [48,49]. On the contrary, scaffolds with lower porosity demonstrated higher cell differentiation with more alkaline phosphatase activity and substantially higher level of osteocalcin than higher porosity scaffolds with the same composition [48]. Henceforth, in summary it was proposed by Kalpan and Abassi et al. [23,50], that osteogenic activity is not driven by the pore size but eventually depends on the porosity. The lower the porosity, the more prone will be MSC cells towards osteogenic differentiation and vice versa. This hypothesis can only be true if the scaffolds pore size is in the magnitude of 50–450 μm [23,50]. Our data clearly supports the statement completely since (G) scaffolds with porosity of 30% vol, which is lower than (H) scaffolds with porosity of 41% vol shows more ALP activity and other crucial transcription factors related to osteo-marker genes like RUNX2 and OSX with other genes. However, in deep analyses is needed to study differential expression of IL-8 and TGF β (anti-inflammatory factors) onto the pore size and porosity of the scaffolds.

5. Conclusions

For the first time, the novel powder feedstock combining osteoconductive, osteoinductive and bioactive elements was developed for 3D printing of the bio-mimetically designed scaffolds for bone engineering. The innovative metalloid/ceramic porous silicon-wollastonite substrates were additively manufactured exploiting the approach of the selective laser melting (SLM). The addition of silicon provided various advantages including (a) good absorptivity for the Nd:YAG laser; (b) osteoinductivity of the scaffold; (c) mechanical strength; (d) printability in single step technology; (e) bio-interface to support osteoblasts.

The parameters of SLM 3D printing were optimized in terms of laser power and energy density. The CAD designed scaffolds with pore size of 400 μm (H) possesses effective elastic modulus and compressive strength of 1.1 ± 0.9 GPa and 37 ± 13.5 MPa, respectively. The scaffolds with the hierarchical gradient of pore size from 50 μm to 350 μm (G) exhibit the effective elastic modulus and compressive strength of 1.8 ± 0.9 GPa and 71 ± 9.5 MPa, respectively. The total porosity exhibited by (H) and (G) scaffolds was 41 vol% and 30 vol% respectively. The compressive strength of the (H) and (G) scaffolds decreased with the immersion time by 16% and 12% during the passage of two weeks respectively. The computational analysis through ANSYS revealed the least stress region at the middle region and at the point of scaffold fixation to the support. The highest stress was concentrated at the surface of both scaffolds in a close proximity with the mesh. The hMSC were well-anchored onto the (H) and (G) scaffolds. Induction of the RUNX2 and OSX, the primary transcription factors for osteogenic differentiation, was expressed nearly twofold in (G) scaffolds as compared to the (H) scaffolds. Induction of the IL-8 and TGF β anti-inflammatory factors demonstrated the possible immunomodulation effect of the scaffolds.

CRedit authorship contribution statement

Nikhil Kumar: Investigation, Data Curation, Formal analysis, Writing - original draft. **Jekaterina Kazantseva:** Investigation, Data Curation, Formal analysis, Writing - review & editing. **Ramin Rahmani:** Investigation, Data Curation, Formal analysis. **Miguel A. Rodriguez:** Conceptualization, Investigation, Methodology,

Supervision, Validation, Writing - review & editing. **Irina Hussainova:** Funding acquisition, Project administration, Conceptualization, Methodology, Supervision, Validation, Writing - review & editing.

Declaration of competing interest

The authors declare that they have no known competing financial interests or personal relationships that could have appeared to influence the work reported in this paper.

Acknowledgements

This work was supported by the Estonian Research Council grant PRG643 (I. Hussainova). The authors would like to acknowledge the help of PhD Olga Volobujeva from Department of Materials and Environmental Technology Engineering, TalTech, for SEM imaging. N. Kamboj would like to acknowledge the personal grant with contract number 2018 186-11 to participate to the January 2020 ACerS Winter Workshop financed by JECS Trust Board.

References

- [1] C. Xu, P. Su, X. Chen, Y. Meng, W. Yu, A.P. Xiang, Y. Wang, Biocompatibility and osteogenesis of biomimetic bioglass-collagen-phosphatidylserine composite scaffolds for bone tissue engineering, *Biomaterials* 32 (2011) 1051–1058, <https://doi.org/10.1016/j.biomaterials.2010.09.068>.
- [2] A. Aidun, A. Zamanian, F. Ghorbani, Novel bioactive porous starch-siloxane matrix for bone regeneration: physicochemical, mechanical, and in vitro properties, *Biotechnol. Appl. Biochem.* 66 (2019) 43–52, <https://doi.org/10.1002/bab.1694>.
- [3] P. Lichte, H.C. Pape, T. Pufe, P. Kobbe, H. Fischer, Scaffolds for bone healing: concepts, materials and evidence, *Injury* 42 (2011) 569–573, <https://doi.org/10.1016/j.injury.2011.03.033>.
- [4] X. Wang, J. Shao, M. Abd El Raouf, H. Xie, H. Huang, H. Wang, P.K. Chu, X.-F. Yu, Y. Yang, A.M. Abdel-Aal, N.H.M. Mekki, R.J. Miron, Y. Zhang, Near-infrared light-triggered drug delivery system based on black phosphorus for in vivo bone regeneration, *Biomaterials*. 179 (2018) 164–174, <https://doi.org/10.1016/j.biomaterials.2018.06.039>.
- [5] N.S. Nikonova, I.N. Tikhomirova, A.V. Belyakov, A.I. Zakharov, Wollastonite in silicate matrices, *Glas. Ceram.* 60 (2003) 342–346, <https://doi.org/10.1023/B:GLAC.000008241.84600.19>.
- [6] M.-Y. Shie, S.-D. Ding, H.-C. Chang, The role of silicon in osteoblast-like cell proliferation and apoptosis, *Acta Biomater.* 7 (2011) 2604–2614, <https://doi.org/10.1016/j.actbio.2011.02.023>.
- [7] L. Fei, C. Wang, Y. Xue, K. Lin, J. Chang, J. Sun, Osteogenic differentiation of osteoblasts induced by calcium silicate and calcium silicate/ β -tricalcium phosphate composite bioceramics, *J. Biomed. Mater. Res. Part B Appl. Biomater.* 100B (2012) 1237–1244, <https://doi.org/10.1002/jbm.b.32688>.
- [8] Y. Huang, C. Wu, X. Zhang, J. Chang, K. Dai, Regulation of immune response by bioactive ions released from silicate bioceramics for bone regeneration, *Acta Biomater.* 66 (2018) 81–92, <https://doi.org/10.1016/j.actbio.2017.08.044>.
- [9] H. Elsayed, J. Schmidt, E. Bernardo, P. Colombo, Comparative analysis of wollastonite-diopside glass-ceramic structures fabricated via stereo-lithography, *Adv. Eng. Mater.* 21 (2019) 1801160, <https://doi.org/10.1002/adem.201801160>.
- [10] P. Melo, A.-M. Ferreira, K. Waldron, T. Swift, P. Gentile, M. Magallanes, M. Marshall, K. Dalgarno, Osteoinduction of 3D printed particulate and short-fiber reinforced composites produced using PLLA and apatite-wollastonite, *Compos. Sci. Technol.* 184 (2019) 107834, <https://doi.org/10.1016/j.compscitech.2019.107834>.
- [11] J. Xie, H. Shao, D. He, X. Yang, C. Yao, J. Ye, Y. He, J. Fu, Z. Gou, Ultrahigh strength of three-dimensional printed diluted magnesium doping wollastonite porous scaffolds, *MRS Commun* 5 (2015) 631–639, <https://doi.org/10.1557/mrc.2015.74>.
- [12] I. Teacencu, N. Rodrigues, N. Alharbi, M. Benning, S. Toumpaniari, E. Mancuso, M. Marshall, O. Bretcanu, M. Birch, A. McCaskie, K. Dalgarno, Osseointegration of porous apatite-wollastonite and poly(lactic acid) composite structures created using 3D printing techniques, *Mater. Sci. Eng. C*. 90 (2018) 1–7, <https://doi.org/10.1016/j.msec.2018.04.022>.
- [13] J. Sanzherrera, J. Garciaaznar, M. Doblare, On scaffold designing for bone regeneration: a computational multiscale approach, *Acta Biomater.* 5 (2009) 219–229, <https://doi.org/10.1016/j.actbio.2008.06.021>.
- [14] J.L. Drury, D.J. Mooney, Hydrogels for tissue engineering: scaffold design variables and applications, *Biomaterials* 24 (2003) 4337–4351, [https://doi.org/10.1016/S0142-9612\(03\)00340-5](https://doi.org/10.1016/S0142-9612(03)00340-5).
- [15] D.M. Reffitt, R. Jugdaohsingh, R.P.H. Thompson, J.J. Powell, Silicic acid: its gastrointestinal uptake and urinary excretion in man and effects on aluminium excretion, *J. Inorg. Biochem.* 76 (1999) 141–147, [https://doi.org/10.1016/S0162-0134\(99\)00126-9](https://doi.org/10.1016/S0162-0134(99)00126-9).
- [16] W. Sun, J.E. Puzas, T.-J. Sheu, X. Liu, P.M. Fauchet, Nano- to microscale porous

- silicon as a cell interface for bone-tissue engineering, *Adv. Mater.* 19 (2007) 921–924, <https://doi.org/10.1002/adma.200600319>.
- [17] A.-S. Wagner, M. Schumacher, M. Rohmke, K. Glenske, M. Gelinsky, S. Arnhold, S. Mazurek, S. Wenisch, Incorporation of silicon into strontium modified calcium phosphate bone cements promotes osteoclastogenesis of human peripheral mononuclear blood cells, *Biomed. Mater.* 14 (2019) 025004, <https://doi.org/10.1088/1748-605X/aaf701>.
- [18] P.-Y. Collart-Dutilleul, I. Panayotov, E. Secret, F. Cunin, C. Gergely, F. Cuisinier, M. Martin, Initial stem cell adhesion on porous silicon surface: molecular architecture of actin cytoskeleton and filopodial growth, *Nanoscale Res. Lett.* 9 (2014) 564, <https://doi.org/10.1186/1556-276X-9-564>.
- [19] S. Kaihara, J. Borenstein, R. Koka, S. Lalan, E.R. Ochoa, M. Ravens, H. Pien, B. Cunningham, J.P. Vacanti, Silicon micromachining to tissue engineer branched vascular channels for liver fabrication, *Tissue Eng.* 6 (2000) 105–117, <https://doi.org/10.1089/107632700320739>.
- [20] S.D. Gittard, A. Ovsianikov, B.N. Chichkov, A. Doraiswamy, R.J. Narayan, Two-photon polymerization of microneedles for transdermal drug delivery, *Expert Opin. Drug Deliv.* 7 (2010) 513–533, <https://doi.org/10.1517/17425241003628171>.
- [21] J. Hernandez-Montelongo, A. Muñoz-Noval, J.P. García-Ruiz, V. Torres-Costa, R.J. Martí-n-Palma, M. Manso-Silvín, Nanostructured porous silicon: the winding road from photonics to cell scaffolds. A review, *Front. Bioeng. Biotechnol.* 3 (2015) 60, <https://doi.org/10.3389/fbioe.2015.00060>.
- [22] A. Di Luca, B. Ostrowska, I. Lorenzo-Moltero, A. Lepedda, W. Swieszkowski, C. Van Blitterswijk, L. Moroni, Gradients in pore size enhance the osteogenic differentiation of human mesenchymal stromal cells in three-dimensional scaffolds, *Sci. Rep.* 6 (2016) 1–13, <https://doi.org/10.1038/srep22898>.
- [23] V. Karageorgiou, D. Kaplan, Porosity of 3D biomaterial scaffolds and osteogenesis, *Biomaterials* 26 (2005) 5474–5491, <https://doi.org/10.1016/j.biomaterials.2005.02.002>.
- [24] A. Seidi, M. Ramalingam, I. Elloumi-Hannachi, S. Ostrovdivov, A. Khademhosseini, Gradient biomaterials for soft-to-hard interface tissue engineering, *Acta Biomater.* 7 (2011) 1441–1451, <https://doi.org/10.1016/j.actbio.2011.01.011>.
- [25] J. Kazantseva, A. Kivil, K. Tints, A. Kazantseva, T. Neuman, K. Palm, Alternative splicing targeting the hTAF4-TAFH domain of TAF4 represses proliferation and accelerates chondrogenic differentiation of human mesenchymal stem cells, *PLoS One* 8 (2013) e74799, <https://doi.org/10.1371/journal.pone.0074799>.
- [26] J. Kazantseva, R. Ivanov, M. Gasik, T. Neuman, I. Hussainova, Graphene-augmented nanofiber scaffolds demonstrate new features in cells behaviour, *Sci. Rep.* 6 (2016) 30150, <https://doi.org/10.1038/srep30150>.
- [27] T. Minasyan, L. Liu, M. Aghayan, L. Kollo, N. Kamboj, S. Aydinyan, I. Hussainova, A novel approach to fabricate Si3N4 by selective laser melting, *Ceram. Int.* 44 (2018) 13689–13694, <https://doi.org/10.1016/j.ceramint.2018.04.208>.
- [28] Z. Chen, X. Wu, D. Tomus, C.H.J. Davies, Surface roughness of selective laser melted Ti-6Al-4V alloy components, *Addit. Manuf.* 21 (2018) 91–103, <https://doi.org/10.1016/j.addma.2018.02.009>.
- [29] N. Kamboj, M. Aghayan, C.S. Rodrigo-Vazquez, M.A. Rodríguez, I. Hussainova, Novel silicon-wollastonite based scaffolds for bone tissue engineering produced by selective laser melting, *Ceram. Int.* 45 (2019) 24691–24701, <https://doi.org/10.1016/j.ceramint.2019.08.208>.
- [30] C. Sarmiento, Z.B. Lukinska, L. Brown, M. Anseau, P.N. De Aza, S. De Aza, F.J. Hughes, L.J. McKay, In vitro behavior of osteoblastic cells cultured in the presence of pseudowollastonite ceramic, *J. Biomed. Mater. Res.* 69A (2004) 351–358, <https://doi.org/10.1002/jbm.a.30012>.
- [31] N. Zhang, J.A. Molenda, S. Mankoci, X. Zhou, W.L. Murphy, N. Sahai, Crystal structures of CaSiO₃ polymorphs control growth and osteogenic differentiation of human mesenchymal stem cells on bioceramic surfaces, *Biomater. Sci.* 1 (2013) 1101–1110, <https://doi.org/10.1039/c3bm60034c>.
- [32] H.Y. Yang, I. Thompson, S.F. Yang, X.P. Chi, J.R.G. Evans, R.J. Cook, Dissolution characteristics of extrusion freeformed hydroxyapatite–tricalcium phosphate scaffolds, *J. Mater. Sci. Mater. Med.* 19 (2008) 3345–3353, <https://doi.org/10.1007/s10856-008-3473-7>.
- [33] I. Bružauskaitė, D. Bironaitė, E. Bagdonas, E. Bernotienė, Scaffolds and cells for tissue regeneration: different scaffold pore sizes—different cell effects, *Cytotechnology* 68 (2016) 355–369, <https://doi.org/10.1007/s10616-015-9895-4>.
- [34] J.R. Woodard, A.J. Hilldore, S.K. Lan, C.J. Park, A.W. Morgan, J.A.C. Eurell, S.G. Clark, M.B. Wheeler, R.D. Jamison, A.J. Wagoner Johnson, The mechanical properties and osteoconductivity of hydroxyapatite bone scaffolds with multi-scale porosity, *Biomaterials* 28 (2007) 45–54, <https://doi.org/10.1016/j.biomaterials.2006.08.021>.
- [35] A. Ho-Shui-Ling, J. Bolander, L.E. Rustom, A.W. Johnson, F.P. Luyten, C. Picart, Bone regeneration strategies: engineered scaffolds, bioactive molecules and stem cells current stage and future perspectives, *Biomaterials* 180 (2018) 143–162, <https://doi.org/10.1016/j.biomaterials.2018.07.017>.
- [36] B. Long, L. Dan, L. Jian, H. Yunyu, H. Shu, Y. Zhi, Evaluation of a novel reconstituted bone xenograft using processed bovine cancellous bone in combination with purified bovine bone morphogenetic protein, *Xenotransplantation* 19 (2012) 122–132, <https://doi.org/10.1111/j.1399-3089.2012.00694.x>.
- [37] H.J. Haugen, S.P. Lyngstadaas, F. Rossi, G. Perale, Bone grafts: which is the ideal biomaterial? *J. Clin. Periodontol.* 46 (2019) 92–102, <https://doi.org/10.1111/jcpe.13058>.
- [38] E.M. Carlisle, Silicon: a possible factor in bone calcification, *Science* (80-) 167 (1970) 279–280, <https://doi.org/10.1126/science.167.3916.279>.
- [39] M. Arora, E. Arora, The promise of silicon: bone regeneration and increased bone density, *J. Arthrosc. Jt. Surg.* 4 (2017) 103–105, <https://doi.org/10.1016/j.jajs.2017.10.003>.
- [40] L.K. Rutz, H. Bockhorn, Theoretical studies on the mechanism of formation of silicon dioxide (SiO₂), *Chemie Ing. Tech.* 77 (2005) 975–976, <https://doi.org/10.1002/cite.200591077>.
- [41] J.R. Henstock, L.T. Canham, S.I. Anderson, Silicon: the evolution of its use in biomaterials, *Acta Biomater.* 11 (2015) 17–26, <https://doi.org/10.1016/j.actbio.2014.09.025>.
- [42] D. Reffitt, N. Ogston, R. Jugdaohsingh, H.F. Cheung, B.A. Evans, R.P. Thompson, J. Powell, G. Hampson, Orthosilicic acid stimulates collagen type 1 synthesis and osteoblastic differentiation in human osteoblast-like cells in vitro, *Bone* 32 (2003) 127–135, [https://doi.org/10.1016/S8756-3282\(02\)00950-X](https://doi.org/10.1016/S8756-3282(02)00950-X).
- [43] W. Sun, Porous Silicon Based Biomaterials for Bone Tissue Engineering, University of Rochester, 2008.
- [44] M. James, G. Wu, Y. Zhao, P.K. Chu, Effects of silicon plasma ion implantation on electrochemical corrosion behavior of biodegradable mg–Y–RE alloy, *Corros. Sci.* 69 (2013) 158–163, <https://doi.org/10.1016/j.corsci.2012.11.037>.
- [45] S. Palakurthy, K. V.G.R., R.K. Samudrala, A.A. P., In vitro bioactivity and degradation behaviour of β -wollastonite derived from natural waste, *Mater. Sci. Eng. C.* 98 (2019) 109–117, <https://doi.org/10.1016/j.msec.2018.12.101>.
- [46] S. Wang, Y. Yang, G.L. Koons, A.G. Mikos, Z. Qiu, T. Song, F. Cui, X. Wang, Tuning pore features of mineralized collagen/PCL scaffolds for cranial bone regeneration in a rat model, *Mater. Sci. Eng. C.* 106 (2020) 110186, <https://doi.org/10.1016/j.msec.2019.110186>.
- [47] G. Akay, M.A. Birch, M.A. Bokhari, Microcellular polyHIPE polymer supports osteoblast growth and bone formation in vitro, *Biomaterials* 25 (2004) 3991–4000, <https://doi.org/10.1016/j.biomaterials.2003.10.086>.
- [48] Y. Takahashi, Y. Tabata, Effect of the fiber diameter and porosity of non-woven PET fabrics on the osteogenic differentiation of mesenchymal stem cells, *J. Biomater. Sci. Polym. Ed.* 15 (2004) 41–57, <https://doi.org/10.1163/156856204322752228>.
- [49] B.T. Smith, S.M. Bittner, E. Watson, M.M. Smoak, L. Diaz-Gomez, E.R. Molina, Y.S. Kim, C.D. Hudgins, A.J. Melchiorri, D.W. Scott, K.J. Grande-Allen, J.J. Yoo, A. Atala, J.P. Fisher, A.G. Mikos, Multimaterial dual gradient three-dimensional printing for osteogenic differentiation and spatial segregation, *Tissue Eng. Part A.* 26 (2020) 239–252, <https://doi.org/10.1089/ten.tea.2019.0204>.
- [50] N. Abbasi, S. Hamlet, R.M. Love, N.-T. Nguyen, Porous scaffolds for bone regeneration, *J. Sci. Adv. Mater. Devices.* 5 (2020) 1–9, <https://doi.org/10.1016/j.jsamd.2020.01.007>.

Paper IV

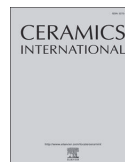
Rodrigo-Vázquez, C.S., **Nikhil Kamboj**, Aghayan, M., Sáez, A., Antonio, H., Rodríguez, M.A. and Hussainova, I., 2020. Manufacturing of silicon-Bioactive glass scaffolds by selective laser melting for bone tissue engineering. *Ceramics International*, doi.org/10.1016/j.ceramint.2020.07.171.

Reproduced with the permission of Elsevier.



Contents lists available at ScienceDirect

Ceramics International

journal homepage: www.elsevier.com/locate/ceramint

Manufacturing of silicon – Bioactive glass scaffolds by selective laser melting for bone tissue engineering

C. Sara Rodrigo-Vázquez^a, Nikhil Kamboj^b, Marina Aghayan^c, Ada Sáez^a, Antonio H. De Aza^a, Miguel A. Rodríguez^{a,*}, Irina Hussainova^b

^a Instituto de Cerámica y Vidrio (CSIC), C/Kelsen 5, Madrid, 28049, Spain

^b Tallinn University of Technology, Ehitajate 5, 19086, Tallinn, Estonia

^c FACT-Industries OÜ, Raja 15, 12618, Tallinn, Estonia

ARTICLE INFO

Keywords:

Selective laser melting
Biomaterials
Bioactive
Glass
Scaffolds
Bone

ABSTRACT

The irruption of additive manufacturing techniques opens the possibility to develop three-dimensional structures with complex geometries and high precision. In the current investigation a newly designed composite combining silicon (30, 40 and 50 wt%) with a bioactive glass and printed into scaffolds was obtained, using a direct selective laser melting (SLM) approach for the first time. Samples were computer-aided designed (CAD) to have cylindrical pores of 400 μm in diameter in order to be used as biomaterials for bone replacement. X – Ray diffraction was used to characterize the appearance of a new phase of pseudowollastonite precipitated by the partial devitrification of the glassy phase after the incidence of laser radiation. The mechanical behaviour of each composition was studied through stress-strain curves, obtaining higher values of compressive strength as the silicon content increases. Scanning electron microscopy coupled to energy dispersive X – Ray spectroscopy (SEM-EDS) and Raman spectroscopy were used to study the bioactivity of each composite after soaking in the simulated body fluid (SBF) for 7 days, confirming this behaviour.

1. Introduction

Designed in 1967, the glass composition of $\text{SiO}_2\text{-CaO-P}_2\text{O}_5\text{-Na}_2\text{O}$ is capable to develop a continuous chemical bonding in the implant/bone interface through the formation of a hydroxyapatite phase [1]; and, therefore, is considered as being bioactive. However, biomaterials are dependent on other equally important factors. The total biocompatibility of the materials, as well as the possible reaction products, is a fundamental question [2]. It should not be the source of chemical species that can trigger an immune rejection response or release toxic or harmful substances for the tissue environment or for the body itself. In addition, the chemical compounds used should favor osteoconductivity and act as a suitable substrate for cellular activity.

To induce cellular responses contributing into acceleration of bone repair and remodeling, the porous structures mimicking in vivo microenvironment are of crucial importance for the formation of tissue. The scaffold has to contain an interconnected network of hierarchically structured porosity for the complete osteointegration of the synthetic scaffold into the bone environment [3,4], and is essential for osteoblastic cells colonization, as well as enzymes and proteins absorption. Moreover, pore size of 300–500 μm [5] is found to be critical

for the process of angiogenesis and complete vascularization of the area. Furthermore, the scaffold' components are preferred to be bioresorbable for prevention of any problems associated with the interface between implant and surrounding tissue such as chronic pain or undergoing a new surgery to proceed with an orthopedic replacement.

The use of synthetic materials also avoids the use of autografts and allografts [6]. Thus, risks associated with these procedures are dodged with infection and ongoing pain following additional surgeries [7] or disease transmission and immune response [8–10], respectively.

Silicon and bioactive glass (along with other ceramic and polymeric biomaterials) have been historically used in bone repair medicine. They showed an adequate stimulus for the phenomena of gene activation and bone mineralization [11]. The high bioactivity of Bioglass® and the huge variety of bioactive glasses tailored in the $\text{SiO}_2\text{-CaO-P}_2\text{O}_5\text{-MgO}$ system, including the 62W glass [12], has been widely confirmed. On the other hand, silicon is an excellent osteoinductive material, up-regulating osteo-related proteins and favors osteoblastic cell differentiation [13,14]. Combining these two materials allows designing a bioactive, osteoconductive and bioresorbable composite. The development of previous in vitro studies of bioactivity and biodegradation before proceeding to clinical trials is a fundamental step. The material

* Corresponding author.

E-mail addresses: nikhil.kamboj@ttu.ee (N. Kamboj), mar@icv.csic.es (M.A. Rodríguez), Irina.Hussainova@ttu.ee (I. Hussainova).

<https://doi.org/10.1016/j.ceramint.2020.07.171>

Received 24 April 2020; Received in revised form 30 June 2020; Accepted 15 July 2020
0272-8842/ © 2020 Elsevier Ltd and Techna Group S.r.l. All rights reserved.

must be capable to promote hydroxyapatite precipitation to confirm its bioactive nature [15]. It is also important the ability of the material to partially degradation in a controlled environment establishing the basis for considering its reabsorption capacity in the physiological environment.

There are many techniques for obtaining composite based scaffolds. However, the appearance of Additive Manufacturing techniques (AM) in the 1980's meant a great change. The possibility of obtaining 3D prototypes using Computer-Aided Design (CAD) was an advance in the design and processing of complex structures. Some of the most commonly used techniques are Stereolithography (SLA) [16,17], Fused Deposition Modeling (FDM) [18–20], Electron Beam Additive Manufacturing (EBAM) [21] and powder bed fusion techniques, i.e. Selective Laser Sintering (SLS) [22–25] and Selective Laser Melting (SLM) [26–29].

Selective Laser Melting (SLM) is an additive manufacturing technique based on the selective melting of an initial powder deposited in successive layers by the action of laser radiation in a controlled atmosphere [30]. The use of SLM to manufacture metal parts is widespread and so far, metal powders of different nature have been the almost exclusive feedstock [31–33]. However, the use of this technology for obtaining 3D structures without using metallic elements has recently been studied [34]. Kamboj et al. successfully obtained porous scaffolds composed of Silicon/CaSiO₃ (wollastonite) with the controlled delivery of vancomycin [35]. The present work develops the process by which Silicon/62W glass (bioactive glass) porous scaffolds have been obtained. The use of SLM over other 3D printing techniques offers the inherent advantages (capable of geometric accuracy at macro- and microscale, direct production from 3D CAD models, digital files implies simple modifications or the ability to reuse waste material), but also is an one-step technique due to time effectiveness and structural stability of the final scaffold. Likewise, it is not necessary to use a polymeric binder when the starting powder is capable of melting by the action of the laser, avoiding the subsequent removal step.

In this work, we have engineered a novel metalloid silicon – bioactive glass porous scaffolds to be produced by AM through SLM without any metallic phase. Silicon' ability to absorb energy together with its osteostimulation properties makes it an ideal candidate for a structural matrix. The addition of bioactive vitreous phase provides the material with ability to establish chemical bonding with the surrounding tissue by precipitating a layer of hydroxyapatite. Mechanical behavior, microstructural features and bioactivity response of three compositions were thoroughly analyzed and compared. Design of 3D scaffolds, favorably modulating bio-processes for tissue healing, combined with tailorable material, can make a vital step in regenerative medicine.

2. Experimental

2.1. Materials

Commercially available silicon (Silgrain < 20 µm, > 99.8% purity; Elkem, Norway) of a medium particle size ~ 4.0 µm was used. The 62W glass composition was prepared from a mixture of reagent grade CaCO₃ (98.5–100 wt% Merck KGaA, Darmstadt, Germany, Ref: 1.02066), SiO₂ (99.7 wt%, Strem Chemicals, Inc. Ref: 93–1435), MgO (97 wt% MERCK KGaA, Darmstadt, Germany, Ref: 1.05865) and Ca₃(PO₄)₂ (Pharma grade, PanReac AppliChem, Darmstadt, Germany, Ref: 141228). The mixture was melted in a double melting process using a Pt–Rh 10% crucible at 1500 °C in an electric furnace for 2 h in total (1 h for each melt) and poured over cold water obtaining a fritted glass. To obtain glass powder, the glass was milled using a tungsten-carbide vibrating cup mill. The powder was sieved below 63 µm and re-milled by attrition milling in isopropyl alcohol medium using 1 mm yttria stabilized zirconia balls at a rotation speed of 880 rpm. Zirconia balls were removed and the milled powder was dried in a stove heated to 65 °C for 24 h and

sieved below 45 µm. The final size distribution was analyzed in a Mastersizer S (Malvern, England) obtaining a medium particle size ~ 2.5 µm.

The powder feedstock for SLM was prepared by dry mixing of 50, 40 and 30 wt % silicon powder with 62W glass to complete 100% composition in a horizontal ball milling. The mixing process was carried out during 8 h with the addition of a 15 wt % of zirconia balls (3 mm diameter) to facilitate mixing performance. After the mixing, zirconia balls were removed. Formulations were named as: 62W50Si, 62W40Si and 62W30Si materials, respectively.

2.2. Selective laser melting (SLM)

A Metal 3D printer (ReaLizer GmbH SLM-50, Germany) equipped with a YAG: Nd³⁺ laser (IPQ Laser GmbH, YLM-120-AC, 120 W and 1.06 µm wavelength, in quasi-continuous-wave mode) with a laser spot size of 15–80 µm was used. The process was performed in the closed chamber purged with a high purity argon (99.999 vol %). Fixed parameters of the process were as following: point distance – 10 µm, layer thickness - 25 µm, exposure time - 125 µs; and scanning speed - 80 mm/s. These parameters were based on the previous studies on Si-wollastonite based scaffolds [25] and were applied to the Si-62 W glasses.

Fig. 1 shows the CAD model used for the manufactured scaffolds. The pores of 400 µm are well-connected by a crest or interconnection joint (between 600 and 800 µm) as depicted in Fig. 1a. The interconnection points should facilitate the adherence of the scaffold with the fractured or the mangled bone forming a tight junction.

Selected printing conditions were selected in order to obtain the desired scaffolds with the different compositions and they are listed in Table 1. However, the great versatility of this technique has allowed the formation of different scaffolds, varying pore size or interconnection joint size. Differences in these parameters for different compositions will be discussed later, in Results and Discussion. Cylindrical samples with dimensions of 5 × 5 mm² with pore size of 400 µm were prepared.

2.3. Characterization

Chemical composition of powders was determined using X-ray Fluorescence spectrometry (XRF) (PANalytical, MagicX (PW-2424) with a RX tube (anode Rh SUPER SHARP) and a generator of 2.4 KW. The FRX analysis of the majority elements was performed on the samples prepared in the form of a pearl using a Philips PerL'X3 pearlizer and a Pt–Au crucible.

The three compositions were characterized before and after the SLM processing by XRD. The samples were grinded to < 63 µm and XRD patterns were recorder on a diffractometer Bruker D8 Advance (Germany) with a monochromator using Cu Kα₁ radiation. Data were collected in the Bragg-Brentano vertical geometry (θ/2θ) between 20 and 80° (2θ) in 0.05° counting for 153 s per step. The EVA-version 6.0 Diffract Plus software (Bruker AXS GmbH, Karlsruhe, Germany) was used to analyze the patterns obtained.

Microstructural analysis of the scaffolds was performed using a scanning electron microscopy system (SEM, Hitachi TM-1000, Tokyo, Japan) with a backscattered electron detector (BSE). In addition, a Field Emission Electron Microscopy (FE-SEM, Hitachi-S4700, Tokyo, Japan) equipped with Energy Dispersive X-Ray Spectroscopy (EDS) was also used.

Compressive strength was measured using a universal testing machine (EM2/200/FR, MicroTest, Spain) using 5 cylindrical samples of each composition of 5 × 5 mm (± 0.1 mm) with crosshead speed of 0.4 mm/min. The compressive load and displacement were recorder at 0.1 s intervals.

Analysis of the hydroxyapatite layer formed on the surface was carried out by RAMAN spectroscopy. The spectrum was obtained using a confocal Raman microscope (inVia Raman Microscope, Renishaw,

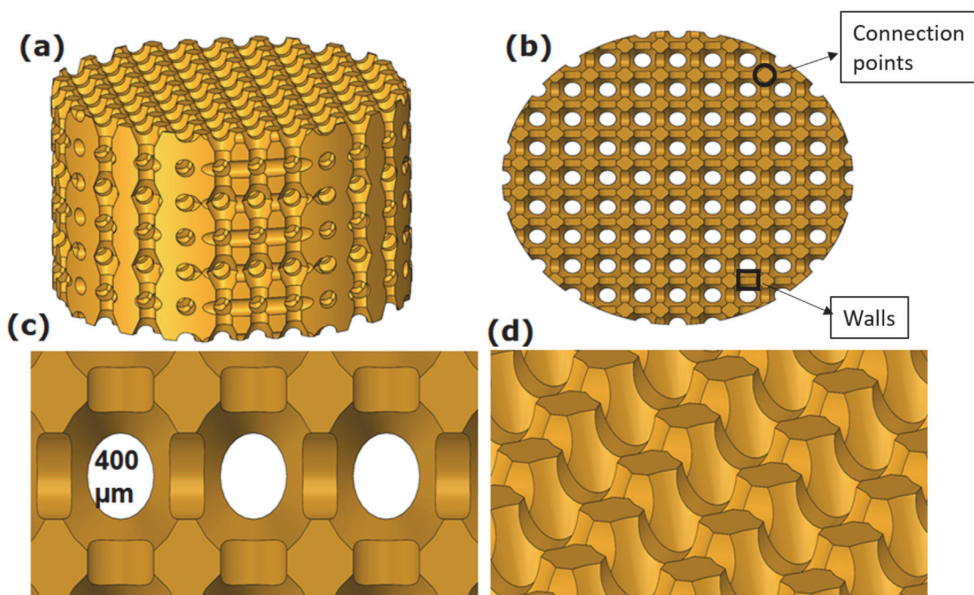


Fig. 1. CAD model of silicon – 62W glass scaffolds a) isometric view; b), c) top view and d) surface morphology. (For interpretation of the references to colour in this figure legend, the reader is referred to the Web version of this article.)

Table 1
Variable printing parameters used for each composition.

Laser current (mA)	62W50Si	62W40Si	62W30Si
	675	675	450
Energy Density (J/mm ³)	140.6	140.6	93.8

UK) equipped with a red laser working at 785 nm and a 10% of power, and a microscope's objective 50x. The measuring conditions were 10 s of exposure time and were collected over the range of 300–1100 nm.

Bioactivity was evaluated *in vitro* using the international standard ISO/FDIS 23317 [28] by preparing a simulated body fluid solution (SBF), fixed in a pH value of 7.4. Cylindrical scaffolds of $5 \times 5 \text{ mm}^3$ were immersed in 30 ml of SBF solution at 37 °C for 7 days using clean conical flasks.

3. Results and Discussion

3.1. Characterization

The composition of the 62W glass is shown in Table 2, jointly with the designed theoretical composition. A good agreement is observed between the designed and the obtained composition. It must be considered that in obtaining glasses it is very difficult to obtain exactly the desired composition when working in small quantities (hundreds of grams).

Fig. 2 shows the XRD pattern of the three feedstock powders. 62W vitreous state was confirmed showing a broad band without any

Table 2
Experimental and designed compositions of 62W Glass.

	CaO	SiO ₂	P ₂ O ₅	MgO
wt. % (designed)	47 ± 1 (46)	39 ± 1 (40)	10.1 ± 0.5 (10.6)	3.0 ± 0.5 (2.8)

crystallization peak between 20 and 40° (2θ). The crystalline state of pure silicon was authenticated by observing five characteristic peaks in the 2θ range between 25–80° (JCPDS Silicon 00-027-1402). Fig. 3 illustrate the XRD spectrum of the 62W50Si, 62W40Si and 62W30Si composites after the SLM process.

It can be seen the appearance of a new crystalline phase corresponding to pseudowollastonite (psW or α-wollastonite, Ca₃(Si₃O₉); JCPDS Card No. 074–0874). It is the high-temperature wollastonite polymorph. This glass composition (62W glass) tends to form this pseudowollastonite phase by a devitrification process. Rodrigo-Vázquez et al. [12] detected the crystallization of this phase in the range 700 °C (8 h of treatment) and 900 °C (1 h of treatment) for this glass composition. However, the exposure time used during the SLM processing was 125 μs. The detection of this crystalline phase indicates that, probably, the vitreous particles have reached temperatures higher than 900 °C.

Morphology of the manufactured scaffolds is shown in Fig. 4. It is possible to perceive the established interaction between silicon particles after the SLM printing. The globular surface as depicted in Fig. 4 shows that the YAG:Nd³⁺ laser energy used was enough to melt the particles, allowing its coalescence and forming the continuous silicon matrix of the final structure. The layer-by-layer pattern is observed in all cases because of the 3D printing processing. On the other side, most of the glassy particles remain in the bulk of this matrix as dispersed phase (Fig. 5). Also some of them are present on the surface with rounded shapes (Fig. 4c, showed by arrows), indicating that viscosity of these particles were relatively low because the high temperature that they reach.

Fig. 5 shows the bulk microstructure of a 62W50Si polished scaffold. Silicon appears to form a continuous phase with some residual porosity (A mapping corresponding to Si), while vitreous phase (B mapping corresponding to Ca) presents cracks probably due to thermal stresses suffered during the processing. It can also be observed a good interaction between silicon and glass phases, making difficult to distinguish the interfaces without the aid of EDS mapping. Due to the presence of Si in both phases the presence of Ca peaks helped us to identify each phase. Therefore, there is a good integration between both materials by

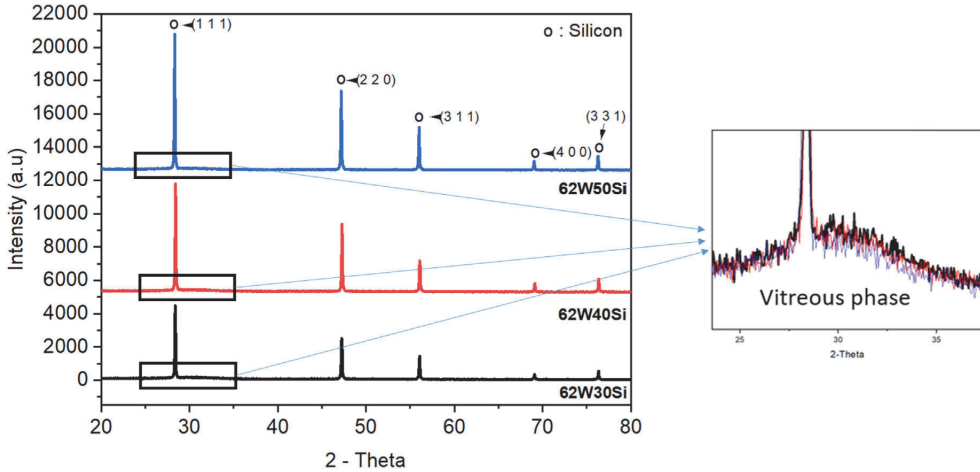


Fig. 2. X – Ray Diffraction patterns of feed stock powders before SLM process with crystalline peaks of silicon (o). (For interpretation of the references to colour in this figure legend, the reader is referred to the Web version of this article.)

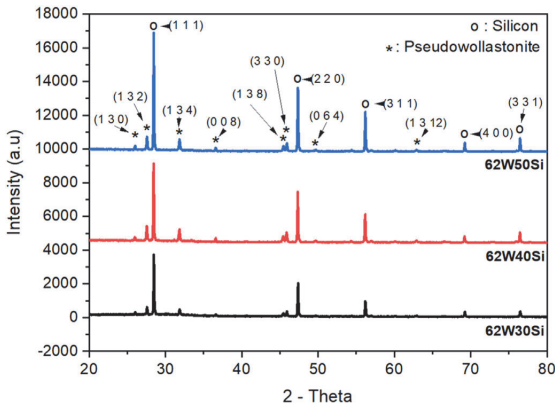


Fig. 3. X – Ray Diffraction patterns of scaffold powders after SLM process with silicon (o) and pseudowollastonite (*). (For interpretation of the references to colour in this figure legend, the reader is referred to the Web version of this article.)

the action of radiation. Even though silicon melting point is 1414 °C and 62W glass present a liquid flow range between 1300–1350 °C. Nevertheless, silicon shows a better interaction with this wavelength laser. The ability of silicon to absorb the energy provided by incident

laser radiation causes the complete fusion of the silicon particles allowing its coalescence. Therefore, the silicon phase is directly responsible for the shaping of the three-dimensional structure, having a fundamental role in the processing of this family of materials. Moreover, the fused silicon particles in contact to glass give energy enough to decrease the viscosity of the vitreous network and, consequently, some of the vitreous particles are joined by a coalescence process forming glass blocks. In addition the temperature increase also allows an increase in the mobility of atoms in the glass structure. It triggers the appearance of a pseudowollastonite phase due to a partial devitrification process. However, the composition with higher amount of glass (62W30Si) shows the lower amount of pseudowollastonite, qualitatively speaking (Fig. 3). This situation is related to the lower amount of energy used for its processing (see Table 2). The amount of energy suitable for a satisfactory interaction depends on the silicon/62W glass ratio. The higher amount of glass makes processes such as “balling” and “showering”, more relevant due to the high temperature difference between the melting powder (silicon) and the adjacent powder (glass) [29]. This phenomenon is common when the thermal expansion coefficients (CTE) of two phases are quite different (CTE Silicon: $2.6 \cdot 10^{-6} \text{ K}^{-1}$ [36]; CTE Bioactive glasses: $14\text{--}15 \cdot 10^{-6} \text{ K}^{-1}$ [37] at room temperature). As a result, obtaining satisfactory scaffolds implies using a low energy density. This establishes an energetic limitation for the devitrification process (governed by thermodynamic control) and finally, less presence of pseudowollastonite. On one hand, 62W50Si and 62W40Si powders have a greater amount of silicon phase in their composition. A decrease in the contact ratio between the melting

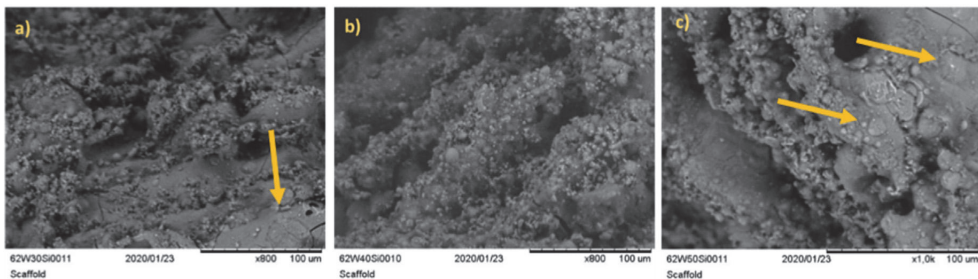


Fig. 4. SEM micrographs of 62W30Si (a), 62W40Si (b) and 62W50Si (c) particle interaction.

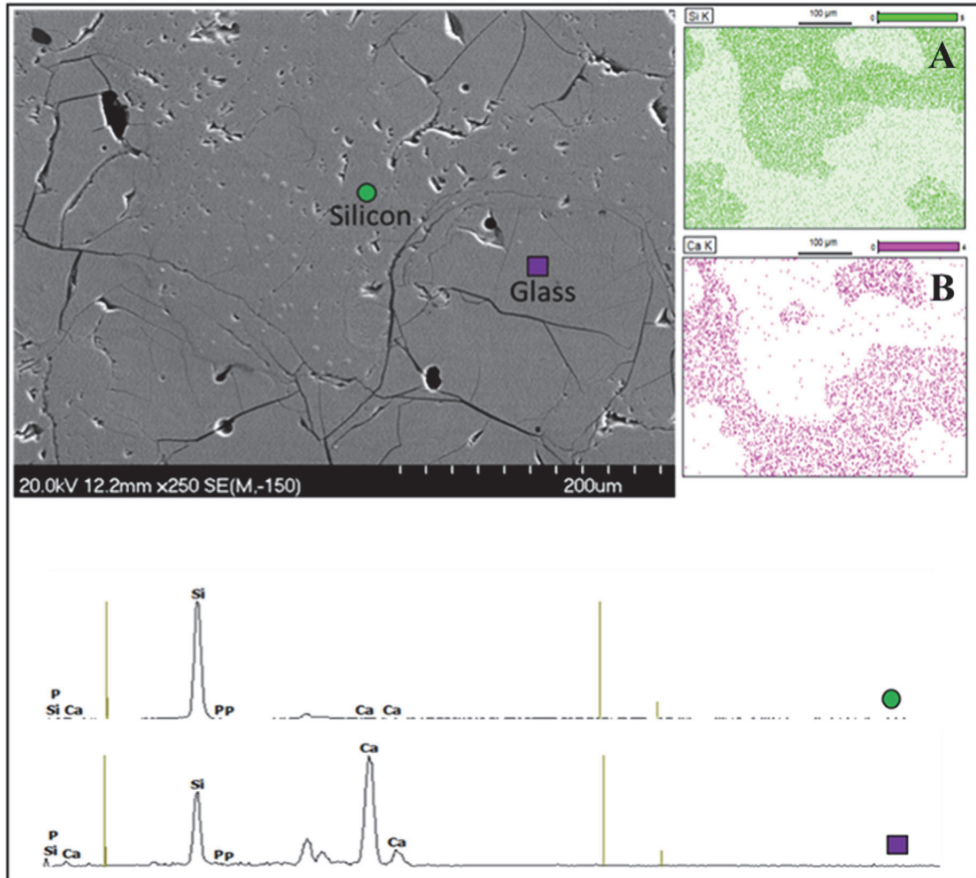


Fig. 5. FE-SEM micrograph of 62W50Si polished surface and EDS + mapping analysis.

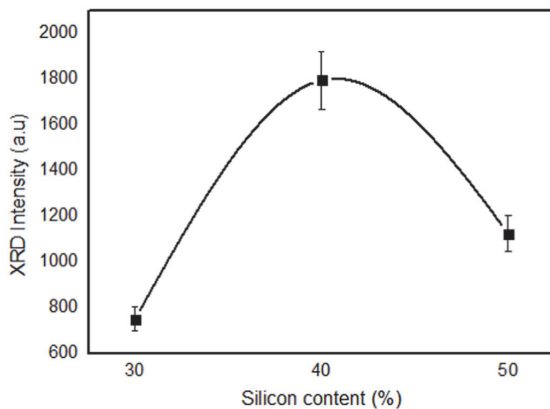


Fig. 6. Pseudowollastonite X – Ray Diffraction main peak (1 3 2) intensity vs. silicon content (wt. %). (Line is drawn as guide).

powder and the adjacent powder decreases adverse effects related to the offset between CTE values and allows the use of a higher energy density level of 140.6 J/mm^3 (see Table 2). On the other hand, Fig. 6 shows that 62W50Si scaffolds has lower pseudowollastonite phase

crystallized than 62W40Si. This result can be explained considering two different theories: the amount of glass is lower in the 62W50Si formulation (it is the phase susceptible to suffer a devitrification process), and the energetic density applied is the same even when composition changes. Sensing this, the composition with lower amount of silicon (62W40Si) will reach higher temperatures due to a more effective energetic absorption process carried out by the silicon phase. Therefore, the intermediate composition (62W40Si) presents a Si/ρ_E relation that favors the highest rate of pseudowollastonite crystallization.

Fig. 7 shows SEM micrographs of the scaffolds surfaces. It can be seen the general porous morphology, showing a regular shape and obtaining a final 3D structure according to the designed model (see Fig. 1). Macroporous size (around $400 \mu\text{m}$) and interconnection joints dimensions (between 600 and $800 \mu\text{m}$) are in good agreement with the model designed. A high degree of surface roughness can also be observed for the three compositions. It is well known that a high surface roughness is an important variable for new bone formation processes, both to promote the precipitation of hydroxyapatite and to facilitate the attaching of osteoblast-like cells [38,39]. The surface roughness can control through the particle size of the feedstock powder. Smaller the particle size, the less surface roughness.

However, it can be also observed the microstructural differences depending on the starting composition. Fig. 7 (a) corresponds to the sample with the lowest amount of silicon (62W30Si). The surface has many pores and cracks outside the preliminary design. This residual

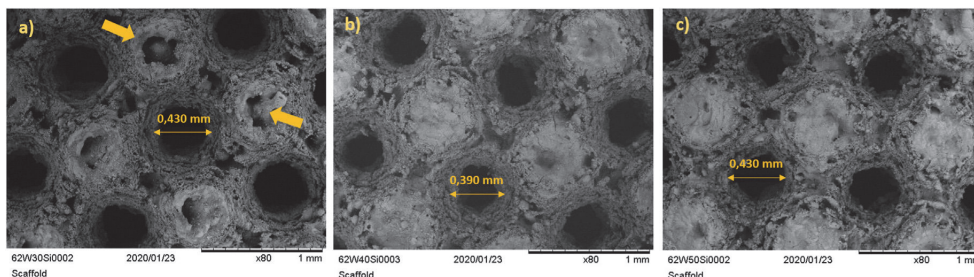


Fig. 7. SEM micrograph of 62W30Si (a), 62W40Si (b) and 62W50Si (c).

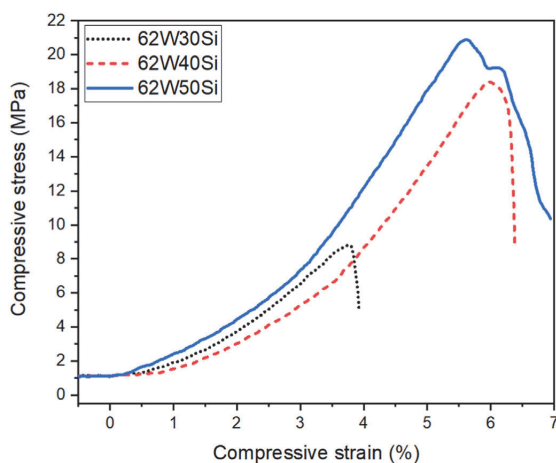


Fig. 8. Compressive stress-strain response of the as-produced scaffolds.

porosity can help in the infiltration of physiological fluids and facilitates biodegradation. In addition, the connection points are not completely dense and present big porous in the center (Fig. 7 (a) pointed by arrows). Samples 62W40Si (Figs. 7 (b)) and 62W50Si (Fig. 7 (c)) show a silicon matrix more continuous with less presence of pores.

Mechanical behavior of the three compositions was tested measuring the compressive strength. Fig. 8 shows the representative compressive stress - strain curve for the tested scaffolds. They present a non-completely brittle behavior that frequently is shown this kind of 3D structures. This non-completely brittle behavior is due to the sequential collapse of the bridges from the most resistant to the weakest.

The values obtained for each composition were 8 ± 1 MPa, 16 ± 2 MPa and 21 ± 4 MPa for 62W30Si, 62W40Si and 62W50Si respectively. An improvement related with the increase of silicon phase amount in the composition is observed. This increase is related to an improvement in the mechanical behavior of the composite with the highest amount of silicon in its composition (Fig. 8, continuous blue line). It means the structure is able to withstand higher compressive loads.

Fig. 9 shows a magnification of the walls for the three scaffolds: 62W30Si scaffold (Fig. 9 (a)) expected to be the weakest, showing major flaws in the wall structure (it can also observe in Fig. 7 (a)). Furthermore, 62W40Si (Fig. 9 (b)) and 62W50Si (Fig. 9 (c)) have a similar look, although the sample with more silicon presents even a better degree of interaction of the particles. The mechanical behavior is consistent with the microstructural differences and the amount and size of observed defects.

3.2. Bioactivity

The most widely used indicator to study the bioactive response of a material and its suitability to bond the surrounding bone tissue is the ability to form an apatite layer when the sample is submerged in a SBF solution for a certain time. In this simulated environment at 36.5 °C and pH of 7.4, an ions exchange is established resulting in the apatite layer formation [1,40]. Fig. 10 (a, b and c) shows the surfaces of the studied scaffolds after 7 days of soaking. The surfaces present a globular microstructure, similar to the hydroxyapatite typical organization. However, comparing the micrographs taken from the surface before the immersion on SBF (Fig. 8), it can be seen a similar microstructure, with a very rough and globular surface. Therefore, different analysis techniques were used to confirm the presence of this new layer in the surfaces of the scaffolds. Fig. 10 (d, e and f) shown FE-SEM micrographs and EDS analysis of the granulated phase that appeared after 7 days of immersion in SBF. The two main elements detected by EDS (without including Si) was Ca and P, confirming the precipitation of a calcium phosphate phase in all the three compositions. A faint signal related to magnesium was also observed which indicated a migration and substitution of Mg^{2+} in this structure.

Fig. 11 shows Raman spectrum of the three samples after 7 days immersed in SBF and a pattern of pure HA. The results reveal the presence of this phase, signifying the characteristics bands for this phase in the spectrum (cm^{-1}): 961(vs) (ν_1 of the P-O bond); 620 (vw), 610 (w), 594 (m), 582 (w) (ν_4 of the O-P-O) and 447 (m), 433 (w) (ν_2 of the P-O-P bond) [41]. The most intense band of the HA is observed in all the three samples. It appears like a broad band instead of a sharp peak due to its lower crystallinity and, similarly, in the case of the other two sets of characteristics peaks of HA. In addition, the high crystallinity silicon matrix, which is acting as a substrate, can also affect to the spectra. Depending on the zone where the laser is projected and the thickness of the HA layer, the silicon signal can be huge. This situation causes that the HA signal to be out of scale and appears with a low intensity and broader (Fig. 11 red line from 62W40Si sample). However, the presence of this signals confirms the precipitation of the HA phase and the bioactivity of this material in a very short period.

This system presents a combined bioactive response, where the glassy phase is mainly responsible for the high bioactivity of the composite scaffolds.

In addition, the biodegradation studies are ongoing in a tris/HCl buffer 0.05 M with pH fixed at 7.4 and 36.5 °C for these materials. Some initial results show a release capacity of the cations with a function of network modifiers (Ca^{2+} and Mg^{2+}) around 50 wt% during the first 7 days. As for the cations with a network former function, both P^{5+} and Si^{4+} release as much lower rate, not exceeding 5 wt% of the total during the same period. The results are consistent with the role played by each of the cations involved.

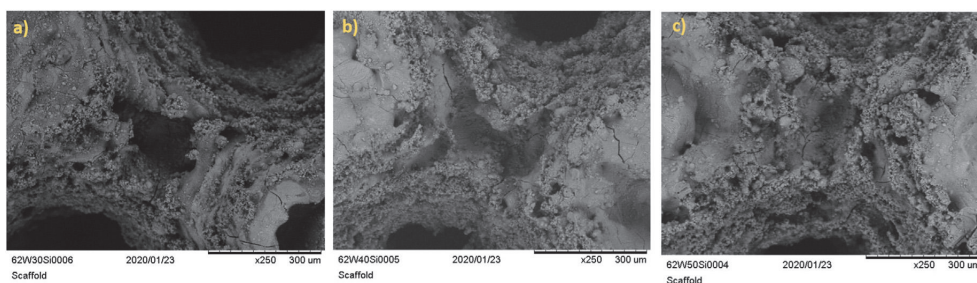


Fig. 9. SEM micrograph of 62W30Si (a), 62W40Si (b) and 62W50Si (c) connection walls microstructure.

4. Conclusions

The compositions studied present the capability to produce a new biocomposite scaffolds processed by Selective Laser Melting (SLM) for its application in bone tissue regeneration. Two phases in different proportions, crystalline silicon and a new designed bioactive glass (62W glass) was used as the feed stock material.

- Silicon phase was responsible to establish a direct interaction with used YAG: Nd³⁺ laser radiation by absorption. This interaction caused the melting of silicon particles, allowing their coalescence and forming a continuous matrix.
- X Ray Diffraction analysis shows the three compositions studied displayed partial devitrification of the vitreous particles, which leads to the appearance of a pseudowollastonite phase after the Selective Laser Melting. The crystallization rate of each composition showed dependence on the level of energy density used during the process. The devitrification process was favored by the increase of temperature of the surrounding silicon particles.

- Measurements of compressive strength shown an improvement with the increasing of silicon phase in the composition. Mechanical response of the materials was determined by silicon phase, improving by ~60% between the composition with least amount of silicon (62W30Si) and the one with highest amount (62W50Si).
- All scaffolds present bioactivity after 7 days immersed in Simulated Body Fluid solution (SBF). Bioactive response was due to the presence of a 62W glass phase (bioactive glass). Scanning Electron Microscope (SEM) and Raman Spectroscopy confirmed the formation of hydroxyapatite on the surface.

Declaration of competing interest

The authors declare that they have no known competing financial interests or personal relationships that could have appeared to influence the work reported in this paper.

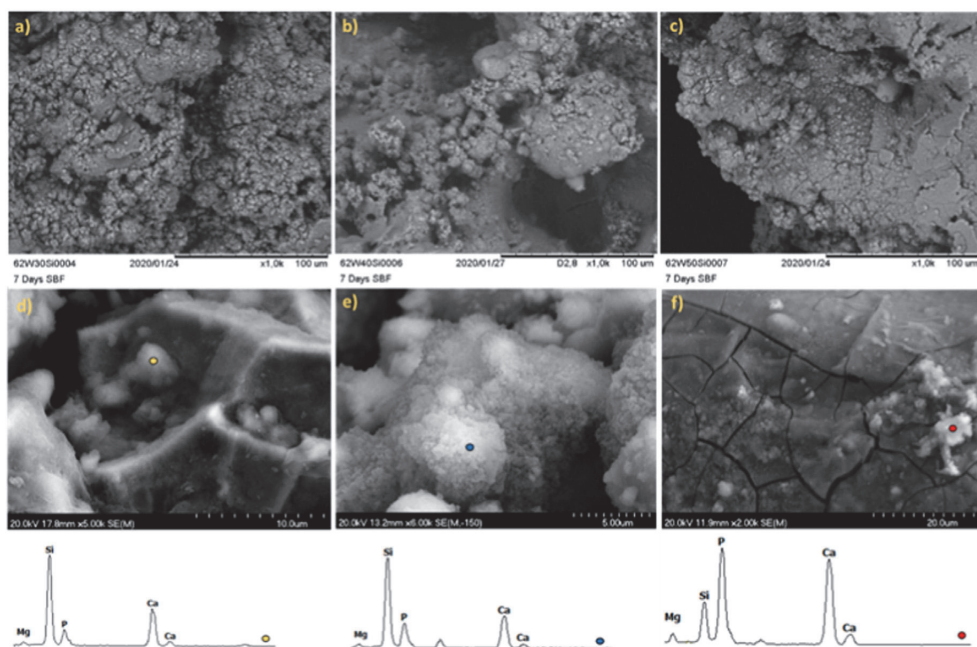


Fig. 10. SEM micrograph of 62W30Si (a), 62W40Si (b) and 62W50Si (c) surfaces after 7 days immersed in SBF. FE-SEM micrographs of 62W30Si (d), 62W40Si (e) and 62W50Si (f) surfaces after 7 days immersed in SBF with EDS analysis.

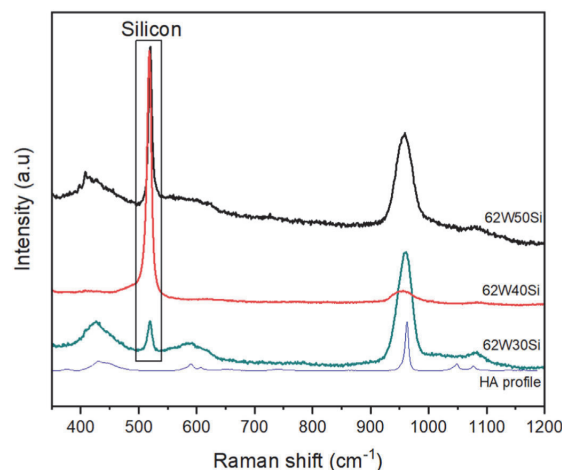


Fig. 11. Raman spectrum of the scaffolds after 7 days immersed in SBF compared to theoretical hydroxyapatite (HA) spectrum.

Acknowledgements

The authors would like to acknowledge DoraPlus program no 3–14/2030/3 “Scholarship for short term visit” offered by the TalTech University of Tallinn (TTÜ, Estonia), the financial support in the frame of projects CSIC-201760E022, CSIC-201860E127 and the personal grant with contract number 2018 186-11 to participate on the January 2020 ACerS Winter Workshop financed by JECS Trust Board. This work was also supported by the Estonian Research Council grant PRG643 (I. Hussainova).

References

- [1] L.L. Hench, H.A. Paschall, Direct chemical bond of bioactive glass-ceramic materials to bone and muscle, *J. Biomed. Mater. Res. Symp.* 4 (1973) 25–42.
- [2] D.F. Williams, On the mechanisms of biocompatibility, *Biomaterials* 29 (2008) 2941–2953, <https://doi.org/10.1016/j.biomaterials.2008.04.023>.
- [3] A. Barbas, A.S. Bonnet, P. Lipinski, R. Pesci, G. Dubois, Development and mechanical characterization of porous titanium bone substitutes, *J. Mech. Behav. Biomed. Mater.* 9 (2012) 34–44, <https://doi.org/10.1016/j.jmbm.2012.01.008>.
- [4] G.M. De Peppo, A. Palmquist, P. Borchardt, M. Lennerås, J. Hyllner, A. Snis, J. Lausmaa, P. Thomsen, C. Karlsson, Free-form-fabricated commercially pure Ti and Ti6Al4V porous scaffolds support the growth of human embryonic stem cell-derived mesodermal progenitors, *ScientificWorldJournal* (2012) 2012, <https://doi.org/10.1100/2012/646417>.
- [5] V. Karageorgiou, D. Kaplan, Porosity of 3D biomaterial scaffolds and osteogenesis, *Biomaterials* 26 (2005) 5474–5491, <https://doi.org/10.1016/j.biomaterials.2005.02.002>.
- [6] J. Henkel, M.A. Woodruff, D.R. Epari, R. Steck, V. Glatt, I.C. Dickinson, P.F.M. Choong, M.A. Schuetz, Di.W. Huttmacher, Bone regeneration based on tissue engineering conceptions-A 21st century perspective, *Bone Res.* 1 (2013) 216–248, <https://doi.org/10.4248/BR201303002>.
- [7] C. Myeroff, M. Archdeacon, Autogenous bone graft: donor sites and techniques, *J. Bone Jt. Surg. - Ser. A.* 93 (2011) 2227–2236, <https://doi.org/10.2106/JBJS.101513>.
- [8] J. Chalmers, Transplantation immunity in bone homografting, *J. Bone Joint Surg. Br.* 41 B (1959) 160–179, <https://doi.org/10.1302/0301-620x.41b1.160>.
- [9] W.F. Enneking, Immunologic aspects of bone transplantation, *South. Med. J.* 55 (1962) 894–900, <https://doi.org/10.1097/00007611-196209000-00007>.
- [10] M. Hinsenkamp, L. Muyille, T. Eastlund, D. Fehily, L. Noël, D.M. Strong, Adverse reactions and events related to musculoskeletal allografts: reviewed by the world health organisation project NOTIFY, *Int. Orthop.* 36 (2012) 633–641, <https://doi.org/10.1007/s00264-011-1391-7>.
- [11] P. Valerio, M.M. Pereira, A.M. Goes, M.F. Leite, The effect of ionic products from bioactive glass dissolution on osteoblast proliferation and collagen production, *Biomaterials* 25 (2004) 2941–2948, <https://doi.org/10.1016/j.biomaterials.2003.09.086>.
- [12] C.S. Rodrigo-vázquez, M.A. Rodríguez, A.H. De Aza, Devitrification study of a novel bioactive glass designed on the CaSiO₃–Ca₃(PO₄)₂–MgCa(SiO₃)₂ system, *J. Non-Cryst. Solids* (2019), <https://doi.org/10.1016/j.jnoncrysol.2019.119705>.
- [13] C. Deng, H. Zhu, J. Li, C. Feng, Q. Yao, L. Wang, J. Chang, C. Wu, Bioactive scaffolds for regeneration of cartilage and subchondral bone interface, *Theranostics* 8 (2018) 1940–1955, <https://doi.org/10.7150/thno.23674>.
- [14] E.M. Carlisle, Silicon: a possible factor in bone calcification, *Science* 167 (80-) (1970) 279–280, <https://doi.org/10.1126/science.167.3916.279>.
- [15] P.N. De Aza, A.H. De Aza, P. Pena, S. De Aza, Bioactive glasses and glass-ceramics, *Bol. La Soc. Esp. Ceram. y Vidr.* 46 (2007) 45–55 www.scientific.net/msf.293.37.
- [16] J.H. Kang, K.J. Jang, K. Sakthiabirami, G.J. Oh, J.G. Jang, C. Park, H.P. Lim, K.D. Yun, S.W. Park, Mechanical properties and optical evaluation of scaffolds produced from 45S5 bioactive glass suspensions via stereolithography, *Ceram. Int.* 46 (2020) 2481–2488, <https://doi.org/10.1016/j.ceramint.2019.09.242>.
- [17] R. Gauvin, Y.C. Chen, J.W. Lee, P. Soman, P. Zorlutuna, J.W. Nichol, H. Bae, S. Chen, A. Khademhosseini, Microfabrication of complex porous tissue engineering scaffolds using 3D projection stereolithography, *Biomaterials* 33 (2012) 3824–3834, <https://doi.org/10.1016/j.biomaterials.2012.01.048>.
- [18] S. Sahmani, A. Khandan, S. Esmaeili, S. Saber-Samandari, M. Ghadiri Nejad, M.M. Aghdam, Calcium phosphate-PLA scaffolds fabricated by fused deposition modeling technique for bone tissue applications: fabrication, characterization and simulation, *Ceram. Int.* 46 (2020) 2447–2456, <https://doi.org/10.1016/j.ceramint.2019.09.238>.
- [19] S. Esmaeili, H. Akbari Aghdam, M. Motiffard, S. Saber-Samandari, A.H. Montazeran, M. Bigonah, E. Sheikhhahaei, A. Khandan, A porous polymeric-hydroxyapatite scaffold used for femur fractures treatment: fabrication, analysis, and simulation, *Eur. J. Orthop. Surg. Traumatol.* 30 (2020) 123–131, <https://doi.org/10.1007/s00590-019-02530-3>.
- [20] A.M. Abdullah, T.N.A. Tuan Rahim, D. Mohamad, H.M. Akil, Z.A. Rajion, Mechanical and physical properties of highly ZrO₂/β-TCP filled polyamide 12 prepared via fused deposition modelling (FDM) 3D printer for potential craniofacial reconstruction application, *Mater. Lett.* 189 (2017) 307–309, <https://doi.org/10.1016/j.matlet.2016.11.052>.
- [21] S. Sahoo, Microstructure simulation of Ti-6Al-4V biomaterial produced by electron beam additive manufacturing process, *Int. J. Nano Biomater.* 5 (2014) 228–235, <https://doi.org/10.1504/IJNB.2014.069811>.
- [22] K.C.R. Kolan, M.C. Leu, G.E. Hilmas, R.F. Brown, M. Velez, Fabrication of 13-93 bioactive glass scaffolds for bone tissue engineering using indirect selective laser sintering, *Biofabrication* 3 (2011) 025004, <https://doi.org/10.1088/1758-5082/3/2/025004>.
- [23] J.M. Williams, A. Adewunmi, R.M. Schek, C.L. Flanagan, P.H. Krebsbach, S.E. Feinberg, S.J. Hollister, S. Das, Bone tissue engineering using polycaprolactone scaffolds fabricated via selective laser sintering, *Biomaterials* 26 (2005) 4817–4827, <https://doi.org/10.1016/j.biomaterials.2004.11.057>.
- [24] D. Pham, R. Gault, A comparison of rapid prototyping technologies, *Int. J. Mach. Tools Manuf.* 38 (1998) 1257–1287, [https://doi.org/10.1016/S0890-6955\(97\)00137-5](https://doi.org/10.1016/S0890-6955(97)00137-5).
- [25] J. Liu, C. Gao, P. Feng, S. Peng, C. Shuai, Selective laser sintering of β-TCP/nano-585 composite scaffolds with improved mechanical properties, *Mater. Des.* 84 (2015) 395–401, <https://doi.org/10.1016/j.matdes.2015.06.161>.
- [26] C.N. Kelly, J. Francovich, S. Julmi, D. Safranski, R.E. Goldberg, H.J. Maier, K. Gall, Fatigue behavior of As-built selective laser melted titanium scaffolds with shell-based gyroid microarchitecture for bone tissue engineering, *Acta Biomater.* 94 (2019) 610–626, <https://doi.org/10.1016/j.actbio.2019.05.046>.
- [27] L. Shpakova, G.I. Gheorghie, C. Nitu, O. Dontu, E. Moraru, D. Besnea, D. Dragomir, Thermal analysis of some prosthetic dental biomaterials processed by selective laser melting, in: G.I. Gheorghie (Ed.), *Proc. Int. Conf. Mechatronics Cyber-Mix-Mechatronics – 2019*, Springer International Publishing, Cham, 2020, pp. 124–132.
- [28] S. Dhiman, S.S. Sidhu, P.S. Bains, M. Bahraminasab, Mechanobiological assessment of Ti-6Al-4V fabricated via selective laser melting technique: a review, *Rapid Prototyp. J.* 25 (2019) 1266–1284, <https://doi.org/10.1108/RPJ-03-2019-0057>.
- [29] L. Hao, S. Dadbakhsh, O. Seaman, M. Felstead, Selective laser melting of a stainless steel and hydroxyapatite composite for load-bearing implant development, *J. Mater. Process. Technol.* 209 (2009) 5793–5801, <https://doi.org/10.1016/j.jmatprotec.2009.06.012>.
- [30] L.C. Zhang, H. Attar, Selective laser melting of titanium alloys and titanium matrix composites for biomedical applications: a review, *Adv. Eng. Mater.* 18 (2016) 463–475, <https://doi.org/10.1002/adem.201500419>.
- [31] S. Liu, Y.C. Shin, Additive manufacturing of Ti6Al4V alloy: a review, *Mater. Des.* 164 (2019) 107552, <https://doi.org/10.1016/j.matdes.2018.107552>.
- [32] J. Zhang, B. Song, Q. Wei, D. Bourell, Y. Shi, A review of selective laser melting of aluminum alloys: processing, microstructure, property and developing trends, *J. Mater. Sci. Technol.* 35 (2019) 270–284, <https://doi.org/10.1016/j.jmst.2018.09.004>.
- [33] S. Afkhami, M. Dabiri, S.H. Alavi, T. Björk, A. Salminen, Fatigue characteristics of steels manufactured by selective laser melting, *Int. J. Fatigue.* 122 (2019) 72–83, <https://doi.org/10.1016/j.ijfatigue.2018.12.029>.
- [34] N. Kamboj, M. Aghayan, C.S. Rodrigo-Vázquez, M.A. Rodríguez, I. Hussainova, Novel silicon-wollastonite based scaffolds for bone tissue engineering produced by selective laser melting, *Ceram. Int.* (2019), <https://doi.org/10.1016/j.ceramint.2019.08.208>.
- [35] N. Kamboj, M.A. Rodríguez, R. Rahmani, K.G. Prashanth, I. Hussainova, Bioceramic scaffolds by additive manufacturing for controlled delivery of the antibiotic vancomycin, *Proc. Est. Acad. Sci.* 68 (2019) 185–190, <https://doi.org/10.3176/proc.2019.2.10>.
- [36] Y. Okada, Y. Tokumaru, Precise determination of lattice parameter and thermal expansion coefficient of silicon between 300 and 1500 K, *J. Appl. Phys.* 56 (1984) 314–320, <https://doi.org/10.1063/1.333965>.
- [37] D. Bellucci, V. Cannillo, A. Sola, Coefficient of thermal expansion of bioactive

- glasses: available literature data and analytical equation estimates, *Ceram. Int.* 37 (2011) 2963–2972, <https://doi.org/10.1016/j.ceramint.2011.05.048>.
- [38] Y. Shin, M. Akao, Tissue reactions to various percutaneous materials with different surface properties and structures, *Artif. Organs* 21 (2008) 995–1001, <https://doi.org/10.1111/j.1525-1594.1997.tb00514.x>.
- [39] D.D. Deligianni, N.D. Katsala, P.G. Koutsoukos, Y.F. Missirlis, Effect of surface roughness of hydroxyapatite on human bone marrow cell adhesion, proliferation, differentiation and detachment strength, *Biomaterials* 22 (2000) 87–96, [https://doi.org/10.1016/S0142-9612\(00\)00174-5](https://doi.org/10.1016/S0142-9612(00)00174-5).
- [40] L.L. Hench, R.J. Splinter, W.C. Allen, T.K. Greenlee, Bonding mechanisms at the interface of ceramic prosthetic materials, *J. Biomed. Mater. Res.* 5 (1971) 117–141, <https://doi.org/10.1002/jbm.820050611>.
- [41] S. Koutsopoulos, *Synthesis and Characterization of Hydroxyapatite Crystals: A Review Study on the Analytical Methods* vol. 62, Wiley Period. Inc., 2002, pp. 600–612, <https://doi.org/10.1002/jbm.10280>.

Curriculum vitae

Personal data

Name: Nikhil Kumar Kamboj
Date of birth: 11.05.1990
Place of birth: Moga, Punjab, India
Citizenship: India

Contact data

E-mail: nikhil.kamboj@ttu.ee

Education

2014–2016 Tallinn University of Technology, MSc in Engineering
2011–2013 IBAB (Institute of Bioinformatics and applied Biotechnology), MSc in Biotechnology and bioinformatics
2008–2011 Lovely Professional University, BSc in Biotechnology
1993–2008 High school, Sacred Heart School Moga, Punjab, India

Language competence

Punjabi Mother tongue
Hindi Native speaker
English Fluent
German Intermediate

Professional employment

2013 Strand Life Sciences, Bangalore, India
2016–2018 Tallinn University of Technology, Department of Mechanical and Industrial Engineering, Early Stage Researcher

Defended thesis

Master's Degree The template-assisted wet-combustion synthesis of mesoporous core-shell structured materials. 2016, Supervisors: Prof. Irina Hussainova, Marina Aghayan

Involvement in research projects

IUT19-29 Multi-scale structured ceramic-based composites for extreme applications
PRG643 Bio-replicating Engineering Structures for Tribo-applications
PUT1063 Nanonet of ceramic fibers with targeted functionalities

Research visits

(1.01.2016–26.05.2016) Erasmus+ Higher Education Student Mobility student at the Institute of Ceramics and Glass, Madrid, Spain

(16.07.2018–14.08.2018) Institute of Ceramics and Glass, Madrid, Spain

Awards and honours

2018, Funding by EPMA to attend AM Motion Summer School from 4th-7th September, Gijon Asturias, Spain

2019, Speaker travel stipend by ECerS to attend Workshop for Young Researchers in Ceramics and Glasses for Medical Applications, Madrid, Spain, 10-11 October

2019, Speaker travel stipend by ACerS for oral presentation at 43rd international conference and exposition of advanced ceramics and composites (ICACC 2019), Jan 27-Feb 1, Florida, USA

2020, Member of the reviewer committee of 2020 Young Ceramists Additive Manufacturing Forum (yCAM) conference, Toulouse, France

2020, Awarded by ECerS with the financial support of the JECS Trust with a grant to attend Winter Workshop to Daytona beach, Jan 24-28, Florida, USA

2020, Chair of the session of symposium: Next generation Bioceramics and biocomposites at 44th International Conference and Expo on Advanced Ceramics and Composites (ICACC 2020), Jan 26-31, Florida, USA

2020, Reviewer of the Journal "Open Ceramics"

Patent

Method for synthesizing rhombohedral FeAlO₃ nanofibers and product comprising said nanofibers thereof; Owners: Tallinn University of Technology; Authors: Marina Aghayan, **Nikhil Kumar Kamboj**, Irina Hussainova; Priority number: P201600017; Priority date: 15.08.2016

Elulookirjeldus

Isikuandmed

Nimi: Nikhil Kumar Kamboj
Sünniaeg: 11.05.1990
Sünnikoht: Moga, India
Kodakondsus: India

Kontaktandmed

E-mail: nikhil.kamboj@taltech.ee

Hariduskäik

2014–2016 Tallinna Tehnikaülikool, Materjalid ja protsessid jätkusuutlikus energeetikas magistrikraad
2011–2013 Bioinformaatika ja biotehnoloogia instituut, biotehnoloogia ja bioinformaatika magistrikraad
2008–2011 Lovely Professional ülikool, biotehnoloogia bakalaureusekraad
1993–2008 Sacred Heart School, keskkool

Keelteoskus

Pandžabi keel emakeel
Hindi keel emakeel
Inglise keel kõrgtase
Saksa keel vahepealne

Teenistuskäik

2013 Strand life Sciences, Bangalore, India, Biokuraator
2016–2018 Tallinna Tehnikaülikool, Mehaanika ja tööstustehnika instituut, doktorant-nooremteadur

Kaitstud lõputööd

Mudel-abistatud märg-põlemise meetodil mesopoorsete kargmaterjalide süntees, Tallinna Tehnikaülikool, Materjali- ja keskkonnatehnoloogia instituut, 2016, juhendajad: Prof. Irina Hussainova, Marina Aghayan

Osalemine uurimisprojektides

IUT19-29 Mitmeastmeliselt struktureeritud keraamika-baasil komposiitmaterjalid kasutamiseks ekstreemtingimustes
PRG643 Biojäljendatud tehnostruktuurid triboloogilisteks rakendusteks
PUT1063 Keraamika kiudude nanovõrgustik sihitute funktsioonidega

Teadusränne

(1.01.2016–26.05.2016) Erasmus+ üliõpilaste õpirände projekti üliõpilane Keraamika ja Klaasi Instituudis, Madrid, Hispaania

(16.07.2018–14.08.2018) Keraamika ja Klaasi Instituut, Madrid, Hispaania

Tunnustused

2018, EPMA stipendium osalemiseks AM Motion suveülikoolis 4.-7. september, Gijon Asturias, Hispaania

2019, ECerS stipendium osalemiseks üritusel “Workshop for Young Researchers in Ceramics and Glasses for Medical Applications”, 10.-11. oktoober, Madrid, Hispaania

2019, ACerS stipendium suuliseks ettekandeks konverentsil “43rd international conference and exposition of advanced ceramics and composites (ICACC 2019)”, 27. jaanuar- 1. veebruar, Florida, USA

2020, Retsensentide komisjoni liige konverentsil “of 2020 Young Ceramists Additive Manufacturing Forum (yCAM)”, Toulouse, Prantsusmaa

2020, ECerS stipendium osalemiseks töötoas “Winter Workshop”, 24.-28. jaanuar, Florida, USA

2020, Sessiooni juhataja sümboosiumil “Next generation Bioceramics and biocomposites at 44th International Conference and Expo on Advanced Ceramics and Composites (ICACC 2020)”, 26-31. jaanuar, Florida, USA

2020, Teadusartiklite retsensendi ajakiri “Open Ceramics”

Tööstusomand

Patentne leiutis: Meetod romboedriline FeAlO₃ nanokiudude sünteesimiseks ja nanokiudusid sisaldav toode; Omanikud: Tallinna Tehnikaülikool; Autorid: Marina Aghayan, **Nikhil Kumar Kamboj**, Irina Hussainova; Prioriteedi number: P201600017; Prioriteedi kuupäev: 15.08.2016